NTNU – Trondheim
Norwegian University of
Science and Technology

Efficient Response Simulation Strategies for Jacket-based Offshore Wind Turbines

An integrated approach combining model reduction and nonlinear irregular wave theory

Bas Verheugt

Wind Energy
Submission date: November 2014
Supervisor: Torgeir Moan, IMT

Norwegian University of Science and Technology
Department of Marine Technology

Efficient Response Simulation Strategies for Jacket-based Offshore Wind Turbines

An integrated approach combining model reduction and nonlinear irregular wave theory

Master of Science Thesis

Author:	Bas Verheugt	
Committee:	Prof. dr. ir. R.H.M. Huijsmans	TU Delft - Chairman
	Ir. J.H. den Besten	TU Delft
	Dr. Ir. G.H. Keetels	TU Delft
	Prof. dr. ir. T. Moan	NTNU
	Assoc. Prof. dr. ir. Z. Gao	NTNU
	Dr. ir. M.C. Ong	NTNU
	Dr. ir. S.N. Voormeeren	Siemens Wind Power
	Ir. M.B. van der Meulen	Siemens Wind Power

November 2014

TUDelft Delft University of Technology

SIEMENS

NTNU – Trondheim
Norwegian University of
Science and Technology

- CONFIDENTIAL -

Summary

The offshore wind industry has been growing exponentially over the last two decades, thereby establishing itself as one of the most promising alternative energy sources. Technological developments are required to reach ambitious cost reduction targets, set to decrease the industry's dependency on governmental support. Two key trends are identified in the development of new offshore wind parks. Firstly, the turbine size increases and secondly, the parks are being built further offshore. Both trends cause the foundation to play an increasingly important role as it is subjected to larger loads. The monopile is the preferred choice of foundation in water depths up to 30 - 40 m because of its effective and proven design. However, following the industry trends the jacket foundation is the most economically attractive option for the deeper waters and larger turbines. At these deeper locations the foundation represents an increasingly large part of the CAPEX, thereby making it suitable component for possible cost reductions. One way to cut costs is by the implementation of a more accurate hydrodynamic model, resulting in less uncertainty and consequently in a more efficient foundation design.

Considering the modeling of the foundation, the geometrical complexity of the jacket makes the design more computationally expensive than for a monopile. The challenge is to keep the model to manageable proportions while incorporating sufficient accuracy, both in wave and structural modeling. The goal of this thesis is therefore to develop an integrated calculation strategy to accurately and efficiently determine the fatigue loads on a jacket-based offshore wind turbine. To this end a nonlinear irregular wave model is implemented and the Morison equation is used to translate wave kinematics to nodal forces in the jacket model. Furthermore, different model reduction techniques are considered to determine the optimal calculation strategy of the response to the hydrodynamic loading. The thesis first provides a theoretical background on the fields of wave and structural modeling. Subsequently, the implementation of the models is described and a case study is defined. This case study forms the basis to fulfill the two key objectives; quantifying the influence of the nonlinear waves and determining an optimal reduced model.

The nonlinear wave model is compared to the linear model in terms of response of the jacket. It is found that the nonlinear model induces 1% to 6% stress increase in the jacket members, depending on the location of the specific member. The stress increase is most pronounced in the splash zone. When considering the amount of kinetic energy triggered by both models, it is demonstrated that the nonlinear model can have a significant contribution to the dynamic response of the jacket. A sensitivity study shows that the eigenfrequencies and damping of the structure play an important role in the response, both in absolute as well as in relative (nonlinear vs. linear) terms.

In the quest for an optimal reduced model three types of models are considered: Guyan, Craig-Bampton (CB) and Augmented Craig-Bampton (ACB). The models are compared in terms of their spectral and spatial convergence with respect to the full model. It is found that the fixed interface vibration modes significantly improve the spectral convergence of the reduced model. To also ensure a high spatial convergence the addition of Modal Truncation Augmentation vectors (MTAs) proves to be essential. Models containing these load case specific modes yield a very small error in terms of potential energy (max. 0.08%), compared to the full model. By clustering the load cases it was found that even a single reduced model containing generic MTAs produces only a small error (max. 1%). To be able to accurately describe the combined wave-wind loading it is recommended to include both fixed interface vibration modes and MTAs.

The reduced model approach reveals its added value when considering the computational time: an averaged size reduced model (± 400 DoF) performs the dynamic simulation nearly ten times faster than the full model (± 1300 DoF). The calculation time of the nonlinear wave model (T_c = 200 s) causes an increase with respect to the linear model (T_c = 110 s) for the wave load generation. However, in the light of the complete analysis, including the dynamic simulation (T_c = 30 min) using a reduced model, the gain in accuracy outweighs the relatively small increase in computational time.

Summarizing, the nonlinear irregular wave model is successfully implemented and the difference in terms of dynamic response is quantified with respect to the linear model. A model reduction strategy is developed which provides an optimal composition of the reduction basis, in terms of accuracy and computational efficiency. These two tools together provide *an efficient, integrated calculation strategy for the dynamic fatigue load analysis of a jacket-based OWT subjected to nonlinear irregular wave loading*, thereby fulfilling the thesis objective.

Acknowledgements

About a year and a half ago Michiel van der Meulen had the opportunity to present his thesis work during one of the lectures at the TU Delft. Having learned the basics of wave theory during my first semester in Denmark, Michiel's topic quickly gained my interest. Not long after that I inquired about the possibilities to write my thesis on a similar topic with Siemens Wind Power in The Hague. After Michiel's enthusiastic reply, a thesis proposal followed and I had my work cut out for me.

The first part of the thesis I carried out in Trondheim at the NTNU. For the guidance during that time I have my Norwegian supervisors to thank. In discussions with Torgeir Moan and Zhen Gao I have gained many insights that helped me to form the theoretical background for this thesis. Muk Chen Ong has been a great help in the verification of the wave model.

Starting January 2014 I continued my work at the Siemens office in The Hague where I really enjoyed the close collaboration with my supervisors Sven and Michiel. The many sparring sessions in or outside of "the stadium" made the potentially solitary process of graduating feel like a team effort. Your combined knowledge of model reduction techniques and wave modeling has greatly contributed to the outcome of this thesis. I would also like to thank professor Huijsmans and Henk den Besten for their constructive feedback during my period at Siemens.

I have the other students at Siemens to thank for the enjoyable office hours. Corine, Lukas, Saskia, Dick, I hope we will have the opportunity to have some more coffee or beer in the near future. Not only the students, but also the other colleagues have contributed to pleasant working environment. The many heated table football games were a good way to blow off some steam. Furthermore, I would like to thank David-Pieter Molenaar for giving the opportunity to write my thesis in collaboration with Siemens. I admire your personal involvement in the way you lead the department. Fortunately my time here was to both of our satisfaction and I am proud to be joining the team after my graduation.

For the required distraction from my work I could always count on my house mates. During my time in Trondheim I have Tim and Marius to thank for on- and off-topic discussions, hazardous fishing trips and the occasional drink. Coen, Arie and Thijs, I have many, many good memories to the time in our "Palazzio d'Esso", the *foundation* for our continued friendship.

Mom and dad, I want to thank you for the unconditional support you have given me during my studies. Your trust has always provided me with the confidence to pursue my aspirations. Finally, Sjakie, I mean it when I say that I could not have done it without you. We have been through a lot together and your support has been vital, not only for the completion of my thesis. I hope now that my sea has calmed down a bit that I can provide the same stability for you.

Amsterdam, November 2014,

Bas Verheugt

Contents

List of Figures

List of Tables

Nomenclature

Latin symbols

$\boldsymbol{B}$	Signed boolean matrix	-
$\boldsymbol{C}$	Damping matrix	-
$\boldsymbol{F}$	Matrix of external force vectors	-
$\boldsymbol{f}$	External force vector	-
$\boldsymbol{g}$	Interface force vector	-
$\boldsymbol{K}$	Stiffness matrix	-
$\boldsymbol{L}$	Boolean matrix	-
$\boldsymbol{M}$	Mass matrix	-
$\boldsymbol{P}$	Projection matrix	-
$\boldsymbol{q}$	Generalized DoF vector	-
$\boldsymbol{R}$	Reduction matrix	-
$\boldsymbol{r}$	Residual force vector	-
$\boldsymbol{T}$	Transformation matrix	-
$\boldsymbol{u}$	Displacement DoF vector	-
a	Amplitude	m
A_{ij}, B_{ij}, C_0	Coefficients in Fourier series	-
B^{-}_{mn}, B^{+}_{mn}	Amplitude transfer function of sum and difference components	-
c	Wave speed / celerity	m/s
C_d	Drag coefficient	-
C_m	Inertia coefficient	-
d	Water depth	m
D	Cylinder diameter	m
D^{-}_{mn}, D^{+}_{mn}	Second-order transfer functions	-
E	Variance density	m^2/Hz
E_k	Kinetic energy	N
E_p	Potential energy	N

f	Frequency	Hz
f_p	Peak frequency	Hz
f_D	Drag force per unit length	N/m
f_I	Inertial force per unit length	N/m
g	Gravitational acceleration	m/s^2
H	Wave height	m
$\overline{H}$	Mean wave height	m
I	Moment of inertia	m^4
H_{m_0}	Significant wave height, estimated from wave spectrum	m
H_s	Significant wave height	m
k	Wave number	rad/m
L	Wave length	m
m_n	n$^{\text{th}}$-order spectral moment	-
N	Order of a series expansion	-
N, M	Number of expansions in a Fourier series	-
p	Pressure	Pa
p	Probability	-
Q^-_{mn}, Q^+_{mn}	Second-order wave kinematics amplitude	-
r	Radius	m
r_i	Inner radius	m
r_o	Outer radius	m
t	Time	s
T	Wave period	s
T_p	Peak wave period	s
T_Z	Zero-crossing wave period	s
$\boldsymbol{V}$	Velocity vector	m/s
u, v, w	Velocity components	m/s
$\dot{u}, \dot{v}, \dot{w}$	Acceleration components	m/s^2
X	Fourier coefficient	-
Y	Single summation Fourier coefficient	-
Z^-_{mn}, Z^+_{mn}	Second-order wave kinematics amplitude	-

Greek symbols

$\boldsymbol{\eta}_i$	Modal amplitude fixed interface vibration modes	-
$\boldsymbol{\Phi}_i$	Fixed interface vibration modes	-

$\boldsymbol{\Phi}_{MTA}$	MTA vectors	-
$\boldsymbol{\Psi}_{C}$	Static constraint modes	-
$\boldsymbol{\zeta}_{i}$	Modal amplitude MTA vectors	-
α	Energy scale	-
γ	Peak-enhancement factor	-
η	Sea surface elevation	m
θ	Wave propagation direction w.r.t. the x-axis	rad
λ	Wave length	m
μ	Expected value	-
ρ	Density	kg/m^3
σ	Peak-width parameter	-
σ	Stress	Pa
Φ	Velocity potential function	m^2/s
ϕ	Wave phase	rad
ω	Angular frequency	rad/s

Subscripts

b	Boundary degree(s) of freedom
dyn	Dynamic part
i	Internal degree(s) of freedom
$stat$	Static part
$_{JS}$	JONSWAP
$_{PM}$	Pierson-Moskowitz

Superscripts

(1)	First-order term
(2)	Second-order term
(s)	Belonging to substructure s
$+$	Sum contribution
$-$	Difference contribution
$\sim$	Reduced
T	Transpose

Abbreviations

ACB	Augmented Craig-Bampton
BEM	Boundary Element Method

BHawC	Bonus Energy Horizontal axis wind turbine Code
CAPEX	Capital expenditures
CB	Craig-Bampton
CB00	A reduced model containing 6 static constraint modes (Guyan)
CB10M10	A reduced model containing 10 fixed interface modes and 10 MTA vectors
CB20	A reduced model containing 20 fixed interface vibration modes
CFD	Computational Fluid Dynamics
CMS	Component Mode Synthesis
DAF	Dynamic Amplification Factor
DD	Direct Drive
DFSBC	Dynamic Free Surface Boundary Condition
DNV	Det Norske Veritas
DoF	Degree of Freedom
EWEA	European Wind Energy Association
FE	Finite Element
FEM	Finite Element Method
FRF	Frequency Response Function
GBS	Gravity-Based-Structure
(I)FFT	(Inverse) Fast Fourier Transform
JONSWAP	JOint North Sea WAve Project
KBBC	Kinematic Bottom Boundary Condition
KFSBC	Kinematic Free Surface Boundary Condition
M20	A reduced model containing 20 MTA vectors
MSL	Mean Sea Level
MTA	Modal Truncation Augmentation
NS	Navier-Stokes (equations)
OC4	Offshore Code Comparison Collaboration Continuation
OWT	Offshore Wind Turbine
PDF	Probability Density Function
PM	Pierson-Moskowitz
POD	Proper Orthogonal Decomposition
POM	Proper Orthogonal Mode
POV	Proper Orthogonal Value
RNA	Rotor-Nacelle-Assembly
SVD	Singular Value Decomposition
TP	Transition Piece

1

Introduction

The first chapter of this thesis provides an overview of the context in which it is written. Firstly, the offshore wind industry is discussed from a holistic perspective in section 1.1, focusing on the latest developments and ambitions. Secondly, the offshore wind turbine itself and its structural components are introduced in section 1.2. Thirdly, the current modeling practices are described in section 1.3. These first three sections provide the background for the motivation behind this thesis, as is explained in section 1.4. Finally, the thesis outline is presented in section 1.5.

1.1 Offshore wind industry

Energy security, or lack thereof, is one of the biggest threats facing today's society. Fossil fuels are currently providing for 80% of global electricity production [29]. However, the fact that the supply of these fuels is diminishing and above all limited, gives rise to the need for other, sustainable energy sources. In Europe, binding legislation has been adopted which aims to accomplish that 20% of the EU energy consumption is produced from renewable energy sources in 2020. Wind energy plays an important role in the shift towards a more sustainable energy mix. The European Wind Energy Association (EWEA) estimates an installed capacity of 230 GW by 2020 and 735 GW by 2050 [11]. An increasingly large portion is projected to be represented by offshore wind energy, as is indicated in figure 1.1a.

In order to accomplish this challenging task, two main trends can be identified in the offshore wind industry. Firstly, the wind turbines are becoming bigger and bigger (figure 1.1b). While the first offshore wind park (Vindeby) was build in 1991 using 0.5 MW turbines, nowadays wind parks are equipped with turbines that have a rated capacity around 5 MW. Within the next decade, 10+ MW turbines are expected to be installed offshore. A second industry trend is that newly consented wind parks are located increasingly further offshore [10]. These sites generally have better wind conditions and therefore a potentially higher yield, but with the

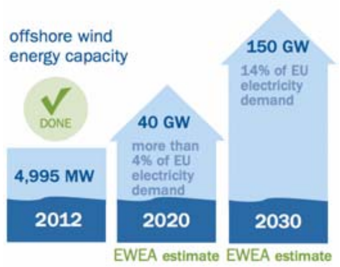

(a) Projected capacity of offshore wind energy in Europe.

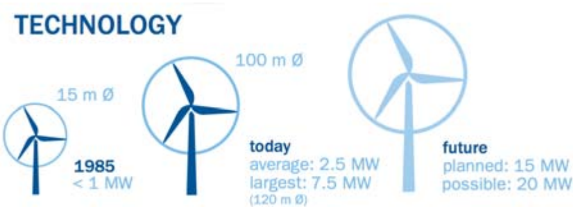

(b) Illustration of the trend towards larger turbines

distance to shore also the water depth and the severity of the weather conditions increase.

Many of the current offshore parks use a monopile foundation because of its relatively simple and cheap design. As the water depth and the forces on the structure increase, so does the diameter and wall thickness of the foundation structure in order to cope with the increased loading. Strengthening the monopile foundation is a feasible option up to the point where other foundation types become more economically attractive. In the UK for example, home to 56% of Europe's offshore installed capacity, a major shift from the use of monopiles to more complex foundations is predicted (figure 1.1).

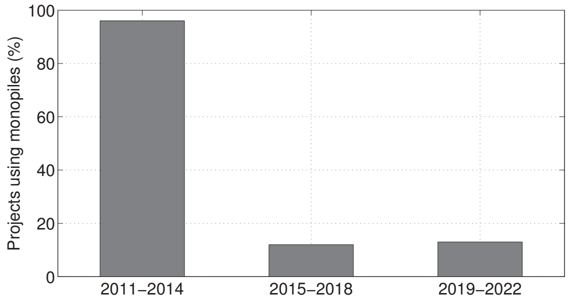

Figure 1.1: Forecast of the use of monopile foundations in the UK [30].

Currently, (offshore) wind energy receives subsidies from the government in order to stimulate its development. However, in the long term the goal for wind energy is to become a self-sustaining energy source, i.e. independent of governmental aid. As the offshore wind industry is relatively young, there is still a lot of room for technological innovations. These are not only desirable from a manufacturers point of view but imperative for the envisioned cost reductions. Regulations and subsidy schemes differ from country to country but cost reductions are a common goal. For example in the Netherlands, the current subsidy scheme is agreed upon between the government and the industry, on the premise that price per MWh is reduced by 40% in the period 2014-2024 [35].

1.2 Offshore wind turbine

In this section the main components of an offshore wind turbine (OWT) are introduced and an overview is given of the different foundation types. An OWT consists of five main structural components (from top to bottom), which can be seen in figure 1.2.

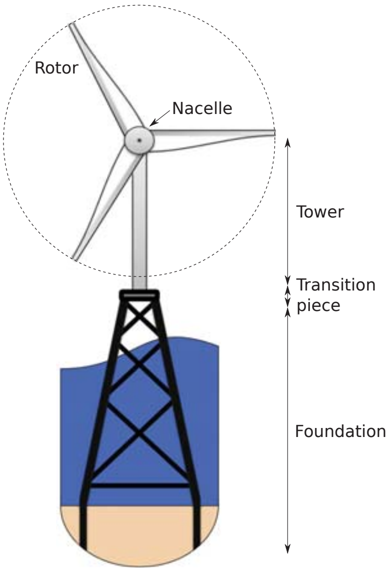

Figure 1.2: Structural components of an OWT [42].

- The **rotor** consists of the blades and the hub that connects them. The shape of the blades generates lift, thereby spinning the rotor. The main function of the rotor is to efficiently transfer aerodynamic energy into rotational energy.
- The **nacelle** is connected to the rotor through the drive shaft. The generator, either geared or direct drive (DD), converts the rotational energy into electrical energy.

- The **tower** is a cylindrical steel tube that tapers from a wide bottom diameter to a smaller top diameter. It is designed to withstand all loads induced by the rotor-nacelle-assembly (RNA). The tower provides access to the RNA for maintenance operations.
- The **transition piece** links the tower to the foundation. The secondary steel components such as a boat landing or a ladder are welded to the transition piece.
- The **foundation** supports the tower and the RNA and its main functionality is transfer of the structural loads to the soil. The type of foundation depends on the site conditions.

All components together are referred to as an *offshore wind turbine*, while everything excluding the RNA is called *support structure*. As stated before, there are several options for the foundation. Four of the most common foundation types are discussed below and illustrated in figure 1.3. The remaining 2% of the foundation types is represented by a mix of tripile and floating solutions.

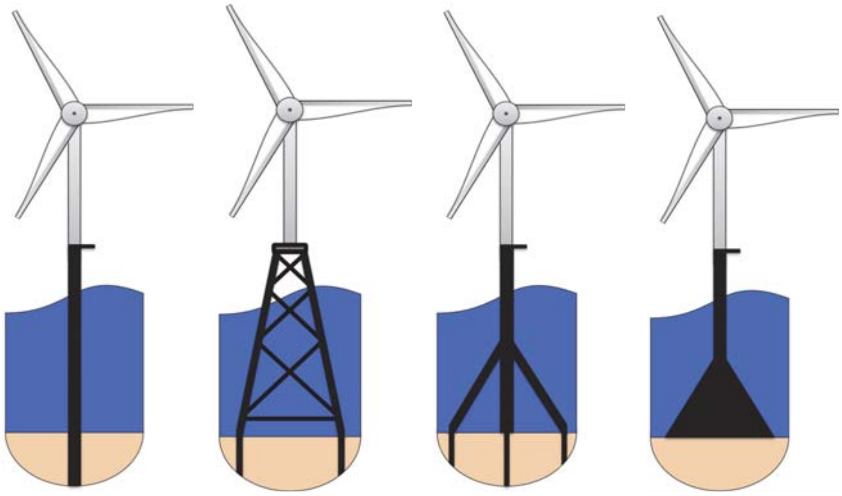

(a) Monopile (76%) **(b)** Jacket (5%) **(c)** Tripod (5%) **(d)** GBS (12%)

Figure 1.3: Different foundation types and their relative occurrence in the EU up to 2013 [42].

- The **monopile** is currently the most popular foundation type and is particularly attractive in relatively shallow waters (up to 30-40 meters). It is a tubular steel construction that is hammered into the seabed. It is relatively cheap due to its simple geometry.
- A **jacket** is a three-, or more commonly four-legged lattice tower, that is based on technology from the oil & gas industry. The legs of the jacket are connected to the piles at the mudline that are hammered into the soil. The connection between the legs is established through the bracing. All jacket members are tubular steel components that are welded together. A jacket foundation is more expensive (€/kg) than a monopile due to the labor intensity. A jacket is applicable for water depths ranging from 20 to 80 meters.
- A **tripod** is a three-legged structure, suitable for similar water depths as the jacket. The central vertical pile is connected to tubular steel legs and the legs are in turn connected to piles that are driven into the seabed.
- A **gravity-based-structure** (GBS) is not piled to the seabed but uses its own weight to for its stability. The structure is hollow and is empty when transported out to the site. Once installed on the seabed, the structure is filled with sand or rocks to increase its mass. A GBS is mainly used in shallow waters.

As was depicted in figure 1.1, monopiles have been the preferred foundation type so far but as wind parks are located further offshore, the jacket becomes a more economically feasible option. In order to identify possible sources for the desired cost reductions mentioned in section 1.1, a general breakdown of the capital expenditures (CAPEX) of an OWT are presented in figure 1.4.

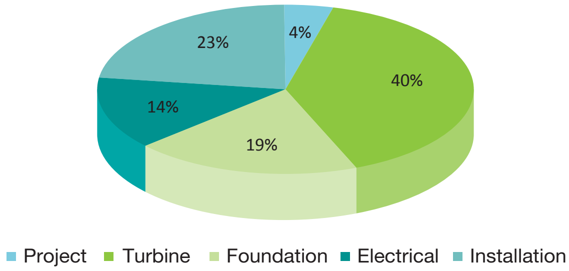

Figure 1.4: Breakdown of the CAPEX of an OWT [30].

It can be seen that the turbine, i.e. tower and RNA, represents the largest share of the CAPEX. However, also the foundation is a major cost driver and therefore potentially an important component in establishing cost reductions. It is noted that the breakdown is site dependent and that the foundation becomes even more important when moving to deeper sites and using larger turbines.

1.3 State-of-the-art modeling practices

This section shortly describes the modeling practices that are employed in the offshore wind industry nowadays. The first part focuses on wave modeling and the translation from velocity and acceleration into force. The second part describes the common practice in the field of structural modeling and introduces the related model reduction techniques.

1.3.1 Wave modeling

In the design of an OWT a distinction is made between two types of loading: fatigue loading and ultimate loading. The first type is related to the damage the structure accumulates during its lifetime due to the cyclic excitation by the environmental loads. The latter is caused by a single, extreme event that generates the maximum loading a structure needs to withstand. In terms of wave loading, the maximum loading is generated by an extreme wave. In order to accurately model the properties of this steep wave, a nonlinear deterministic model is often employed [13].

For the simulation of the fatigue loading a time series of an irregular wave train is required, rather than a single wave. This irregular wave record is generated using a summation of many frequency components, each with a random amplitude and phase. This method is usually based on linear (Airy) wave theory [2], thereby neglecting any higher order effects in the elevation of the sea surface. This approach was adopted from the oil & gas industry where the assumption to neglect higher order effects is valid due to the small ratio of wave height over water depth (H/d). As offshore wind parks are generally located on more shallow sites, the higher order effects can become more pronounced. In a case study for an offshore wind park on monopile foundations in the German Bight it was found that the equivalent fatigue load increases 4% to 6% when using a second-order wave model, compared to a linear model [41].

Using one of the above-described wave models, the surface elevation and the kinematics (velocity and acceleration) of the sea can be described. However, due to the linearization of the boundary conditions of the wave problem, the expressions are only valid up to the Mean Sea Level (MSL). In order to be able to describe the kinematics underneath the wave crest and above MSL, the kinematics need to be stretched to the free surface. Different methods have been developed to overcome this problem. Possible stretching methods are the widely adopted, empirical Wheeler stretching method [46] or the second-order kinematics model based on a Taylor-expansion around MSL [38].

Once the wave kinematics are fully described, they can be translated into hydrodynamic loads through the use of the Morison equation [27]. This semi-empirical equation is the sum of two force components: an inertia term proportional to the flow acceleration and a drag term proportional to the (signed) square of the flow velocity. The structural properties are captured in the inertia coefficient (C_m) and the drag coefficient (C_d).

1.3.2 Structural modeling

Using the wave force obtained from the Morison equation as a starting point, this section focuses on the modeling of the structure's response to this applied force. Finite element (FE) models are common engineering practice to analyze a structure's response (displacement, velocity and acceleration) and corresponding stresses and strains. An FE model approximates the partial differential equations governing the structural elements. The model consists of a set of appropriate finite elements interconnected at certain points, so called *nodes*. Depending on the type of finite element, one is able to describe the displacements and/or rotations of the element in the plane of interest. The number of independent parameters that describe the state of the element are called *degrees of freedom* (DoF). For example, a 3D beam element that is able to displace and rotate (2) in all three directions (x3) at both ends of the element (x2) has 12 DoF.

When considering a jacket foundation it is easy to imagine that an accurate FE model consists of many beam elements, with an even larger number of corresponding DoF. In order to calculate the fatigue loads on an OWT, the FE models of the jacket (± 1000 DoF), tower (± 100 DoF) and RNA (± 300 DoF) are implemented in a dynamic simulation software (e.g. BHawC) where the external wind and wave load are applied to the structure in a time-domain simulation. In this simulation the wind turbine controller is also included in the simulations. The calculation time is proportional to the amount of DoF in the structure and it is obvious that the jacket has a large contribution to this. In the design phase of an offshore wind park +10.000 simulations have to be run to simulate all possible loading conditions of the OWT. A relatively small gain in terms of calculation time could therefore have a large impact on the duration of the design phase. In order to reduce the amount of DoF and thereby the calculation time, several model reduction methods have been developed. The ones that are discussed in the thesis are shortly introduced here:

- The **Guyan** method [16], also known as static condensation, makes a distinction between *internal* DoF and *boundary* DoF. The boundary DoF are located at the node(s) where the structure connects to an adjacent structure. The Guyan method aims to capture the displacement of all the internal DoF using static constraint modes, i.e. the static response of the internal DoF to a unit displacement of the boundary DoF. This method does not account for any dynamics in the reduction nor does it allow for external force to be applied on the internal DoF.

- The **Craig-Bampton** (CB) method [5], similar to the Guyan method, subdivides the DoF into internal and boundary DoF, but it does not neglect the dynamics of the structure. Instead, the CB method is based on the premise that the dynamics of the internal DoF can be described by including the fixed interface vibration modes of the structure. This addition overcomes the main drawback of the Guyan method.
- The **Augmented Craig-Bampton** (ACB) method provides an additional set of vectors to the reduced system of equations, based on the CB method. These additional vectors are load-dependent and allow the structure to deform in the dominant shapes induced by the external force. These force vectors can be obtained by performing a Proper Orthogonal Decomposition (POD) on the time series of the external force.

The Guyan method used to be industry standard until recent years. However, this method has been proven to produce significant errors in terms of the structure's forced response due to its inability to model the internal dynamics of the system [44]. The CB and ACB method provide only a slightly larger reduced model but yield a large increase in accuracy compared to the Guyan method.

1.4 Thesis motivation and objective

The previous sections outline the context of this thesis, both in terms of the developments in wave and structural modeling as well as its connection to the industry trends. Section 1.1 demonstrates the great potential and ambition of the offshore wind industry and the driving developments. The trends of moving towards deeper water depths and using larger turbines results in the fact that jacket foundations are gaining ground on the monopile.

In terms of wave modeling, nowadays often a linear irregular wave model is used with a certain safety factor in order to correct for the neglected higher order effects. A more accurate, second-order wave model will eliminate part of this uncertainty and might lay the basis to reconsider the current safety factor. As stated before, the equivalent fatigue loads for a monopile have shown to increase around 5% when using a second-order wave model. A jacket foundation is generally located in deeper waters, which would indicate a smaller wave steepness and thus a smaller second-order contribution. On the other hand, in deeper waters the wave loading becomes more dominant. In any case, a more accurate model could potentially lead to a less conservative and more cost effective design, working towards the much needed cost reductions in the offshore wind industry.

The several model reduction techniques offer the opportunity to significantly reduce the simulation time of the dynamic analysis of the OWT. Both the CB and the ACB method have shown very promising results in this respect. However, insights are still missing with regards to an optimal reduced model definition, in terms of accuracy and efficiency. This is especially true when considering a combination of load cases with different wave heights and directions. Because of the jacket's complex geometry, special attention has to be paid to what extent the reduced model is able to represent the dynamics of the structure. This is specifically important for the nonlinear wave model, as this model is expected to trigger more dynamics than the linear model.

Summarizing, the challenge in this thesis lies in combining the worlds of wave modeling and structural modeling, in a way that provides both academic value as well as useful engineering applications. Hence, the objective of this thesis can be formulated as follows:

> *Develop an efficient, integrated calculation strategy for the dynamic fatigue load analysis of a jacket-based OWT subjected to nonlinear irregular wave loading.*

This objective can be subdivided into the two following main tasks:

1. Implement a second-order irregular wave model for a jacket foundation and examine the difference with respect to a linear model.
2. Investigate model reduction techniques and develop an efficient application for the load analysis of an OWT.

1.5 Thesis outline

In order to fulfill the above-stated objective in a structured way, the content of this thesis is subdivided into a number of chapters. To start off, a theoretical background in both wave and structural modeling is required. Chapter 2 treats linear and nonlinear wave theory, several stretching methods and the translation from wave kinematics into wave loading. Next, an introduction is given to the field of domain decomposition in chapter 3. First the philosophy of the procedure is discussed after which the several model reduction techniques are introduced.

With the theoretical background discussed, chapter 4 treats both the implementation of the wave and structural model, as well as the setup of the case study.

This case study is conducted using measurement data from an offshore site in the German Bight. The results of this study are discussed in chapter 5 and chapter 6, respectively. Chapter 5 focuses on the difference in member stresses caused by the linear and the nonlinear wave model. In chapter 6 a number of reduced models is compared based on their accuracy and efficiency in calculating the dynamic response of the jacket foundation. Finally, chapter 7 concludes on the obtained insights and provides recommendations for future work.

2

Wave modeling

2.1 Introduction

In order to accurately model waves and their corresponding kinematics, a profound understanding of the theoretical background is required. This chapter provides a introduction into the different types of waves in section 2.2. Section 2.3 describes the basic wave motion and introduces the parameters involved. An overview of the derivation of the wave problem is presented in section 2.4 and a solution to the problem is presented in section 2.5. Several profile extension methods to describe the wave kinematics (velocity and acceleration) above the mean sea level (MSL) are discussed in section 2.6. The basic wave equations are consequently expanded to both irregular waves and nonlinear waves in section 2.7 and 2.8, respectively. In the final section of this chapter, the Morison equation is introduced, which is used to translate wave kinematics into hydrodynamic forces.

2.2 Sea spectrum

The ocean consists of many different types of waves. The different wave types can be distinguished based on their wave period. An overview of the spectrum of ocean waves and their corresponding periods is given in figure 2.1. In order to determine what range of waves should be taken into account for the loads on offshore structures it is important to consider the structural eigenfrequencies. For bottom fixed support structures used for wind turbines such as a monopile or jacket, the first eigenfrequency lies around 0.3 Hz [3]. This implies that the wind-generated waves are of significant importance since they cover the frequency range between 0.05 and 1 Hz.

As can be seen from figure 2.1, the wind-generated waves can be subdivided into several categories. A distinction can be made based on the governing force that controls the waves. The waves that have a higher frequency than 4 Hz and wave lengths shorter than 10 cm, are referred to *capillary waves*. For these capillary waves, surface tension is the governing force. As the frequency decreases and the wave length increases, the gravitational force takes over and the waves are referred to as *surface gravity waves*.

Waves that are generated by local winds are *short-crested* (directional) and *irregular* (multiple frequencies) and are called a *wind sea*. As the waves propagate and get a chance to develop away from the generation area, they become more *long-crested* (uni-directional) and *regular* (single frequency) and eventually form a *swell*. In addition to the waves, also tidal currents need to be considered as they can add a net current to the horizontal wave velocity. Tides are generated by the interaction of the oceans with the moon and the sun. Finally, storm-surges need to be taken into account as they generate a large-scale surface elevation due to low atmospheric pressure and high wind speeds in the storm. This effect causes a rise of the MSL, which in turn influences the hydrodynamic forces on the support structure.

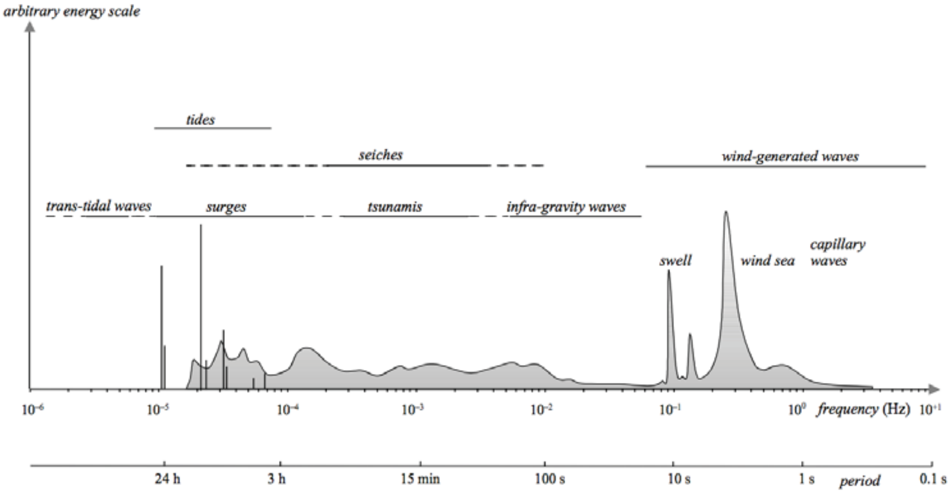

Figure 2.1: Periods of the vertical motions of the ocean surface [18].

2.3 Basic wave motion

Before being able to describe an open sea, one first needs to understand the properties of a single wave. Figure 2.2 shows a regular, unidirectional wave and its corresponding properties. The axis system is defined at MSL, which is the average height of the sea surface. The wave is propagating in positive x-direction. The z-axis is defined positive upwards which entails that the depth d is described by a negative z-coordinate. The wave height is indicated by H and is defined as the vertical distance between the crest and the through. For a linear regular wave, the amplitude is defined as $a = H/2$. The wave length L is the horizontal distance between two crests. The time between two consecutive up- or down-crossings of MSL is defined as the wave period $T = 1/f$, where f is the wave frequency. Finally, the phase of the wave is given by ϕ. Using these definitions, the surface elevation η can be represented by a harmonic wave according to equation 2.1.

$$\eta(t) = a\cos(2\pi f t + \phi) \tag{2.1}$$

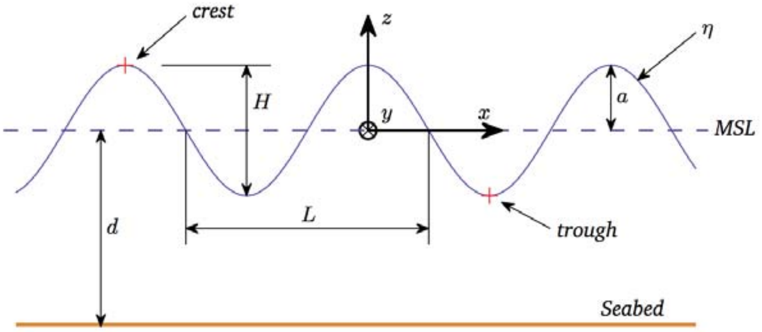

Figure 2.2: Wave parameter definitions [41].

2.4 Wave problem

The wave problem consists of the governing equations that describe the physical behavior of a wave. A detailed derivation of the equations is provided in appendix A. This section introduces the main assumptions in the derivation and presents the linearized equations for the 2D wave problem. The continuity equation and the conservation of momentum form the starting point for the derivation of the wave problem. From this the Navier-Stokes (NS) equations can be found, when assuming an incompressible fluid. These equations can describe wide variety of flow phenomena. Computation Fluid Dynamics (CFD) is one of the fields using these equations to numerically approximate flow problems. Unfortunately, analytical solutions to these equations only exist for simple problems. Therefore two assumptions are made in order to simplify the governing equations. The first assumption is that the flow can be regarded as inviscid. This is a valid assumption since the viscous effects only play a significant role in the wave boundary layer and are negligible when considering the global wave motion.

The second assumption states that the flow is irrotational. This might be counter-intuitive when considering the motion of a wave. However, irrotationality in a frictionless fluid can be easily interpreted when considering in infinitesimal small fluid element, e.g. a sphere. Since the fluid is frictionless, the surface forces act through the center of the sphere and therefore can not exert any torque on the element. Hence, no change in angular velocity occurs and a fluid element that is initially at rest can not be forced to rotate. The assumption of irrotationality allows for the fluid velocities to be described by a velocity potential Φ. Inserting the velocity potential into the continuity equation yields the Laplace equation:

$$\nabla^2\Phi = 0 \tag{2.2}$$

This is the governing equation for potential wave theory. In order to obtain a solution for the velocity potential, several boundary conditions are required. The equations corresponding to the boundary conditions are related to the linearized wave problem. In the linearization of the wave problem lies the assumption that the wave steepness H/d is very small. For the nonlinear boundary conditions the reader is referred to section A.3 in appendix A.

- The **kinematic bottom boundary condition** (KBBC) states that the sea bottom is impermeable and thus the vertical fluid velocity has to be zero there.

$$\frac{\partial\Phi}{\partial z} = 0 \quad \text{for } z = -d \tag{2.3}$$

- According to the small wave steepness assumption, **kinematic free surface boundary condition** (KFSBC) states that for infinitesimal small waves, the vertical motion of the fluid is equal to the vertical velocity at MSL.

$$\frac{\partial\Phi}{\partial z} = \frac{\partial\eta}{\partial t} \quad \text{for } z = 0 \tag{2.4}$$

- The **dynamic free surface condition** (DFSC) enforces the atmospheric pressure to be equal to the pressure in the fluid at the free surface.

$$\frac{\partial\Phi}{\partial t} + g\eta = 0 \quad \text{for } z = 0 \tag{2.5}$$

Equations 2.2 to 2.5 together formulate the 2D linearized wave problem.

2.5 Solution to the Laplace equation

Now that the wave problem is clearly defined, a solution to the Laplace equation can be found. This procedure is described in many textbooks on fluid dynamics, such as for example in [39]. The assumption on which the derivation is based is that the velocity potential can be described by a product of functions, each of which just depends on a single variable. This method is also referred to *separation of variables*. The outcome of this procedure is an expression for the velocity potential of a propagating wave:

$$\Phi = \frac{ag}{\omega} \frac{\cosh k(z+d)}{\cosh kd} \sin(kx - \omega t + \phi) \tag{2.6}$$

Where k is the wave number and ω is the radial frequency. By entering the expression for the velocity potential into the dynamic free surface boundary condition (2.5), the expression for the surface elevation is found:

$$\eta = a \cos(kx - \omega t + \phi) \tag{2.7}$$

To obtain the *dispersion relation*, the velocity potential is substituted into the kinematic free surface boundary condition:

$$\omega^2 = k\, g \tanh kd \tag{2.8}$$

The dispersion relation defines the compatibility between temporal and spatial periodicity, i.e. a wave with a certain period $T = 2\pi/\omega$ has a certain corresponding wave length $\lambda = 2\pi/k$. Together with the velocity potential and the surface elevation, the dispersion relation forms the core of linear wave theory. Based on the dispersion relation, the wave celerity or phase velocity ($c = \lambda/T = \omega/k$) becomes:

$$c = \sqrt{\frac{g}{k} \tanh kd} \tag{2.9}$$

Dispersion thus entails that waves of different wavelengths travel at different phase speeds. It is observed that in the deep water limit, the phase velocity is merely dependent on the wave number:

$$c = \sqrt{\frac{g}{k}} \quad \text{as } \tanh kd \to 1 \tag{2.10}$$

In the shallow water limit however, all dependency on the wave number disappears as the water depth becomes the dominating variable:

$$c = \sqrt{gd} \quad \text{as } \tanh kd \to kd \tag{2.11}$$

By combining the expression for the velocity potential (2.6) and the dispersion relation (2.8), the horizontal (u) and vertical (w) wave particle velocity components are found:

$$u = \frac{agk}{\omega}\frac{\cosh k(z+d)}{\cosh kd}\cos(kx-\omega t+\phi) \tag{2.12}$$

$$w = \frac{agk}{\omega}\frac{\sinh k(z+d)}{\cosh kd}\sin(kx-\omega t+\phi) \tag{2.13}$$

The accelerations are obtained by taking the time-derivative of the velocities:

$$\dot{u} = agk\frac{\cosh k(z+d)}{\cosh kd}\sin(kx-\omega t+\phi) \tag{2.14}$$

$$\dot{w} = -agk\frac{\sinh k(z+d)}{\cosh kd}\cos(kx-\omega t+\phi) \tag{2.15}$$

It can be observed that the horizontal and the vertical velocity are $\pi/2$ (rad) out of phase; the maximum values of the horizontal velocity appear under the crest and trough positions ($kx-\omega t+\phi = 0, \pi, ...$), whereas the maximum values of the vertical velocity are found where the surface elevation is zero ($kx-\omega t+\phi = \pi/2, 3\pi/2, ...$). This behavior is illustrated in figure 2.3.

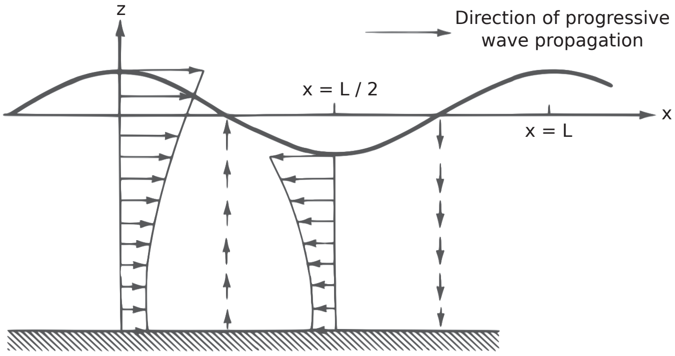

Figure 2.3: Water particle velocities in a progressive wave [7].

It is noted that the acceleration vector is always perpendicular to the velocity vector. This is important when calculating the loads on a slender structure. The trajectories that the particles travel due to the wave motion is dependent on the ratio between the water depth and the wave height. In deep water ($d/L > 1/2$), the water particles follow a circular path, in which the velocities decay exponentially with depth. In the shallow waters ($d/L < 1/20$), the horizontal motion becomes more pronounced as the vertical decay of the velocities mainly applies to the vertical velocity w. In the intermediate region ($1/20 < d/L < 1/2$), the shape of the trajectory corresponds to an elliptical shape. An illustration of the trajectories for different relative depth is provided in figure 2.4.

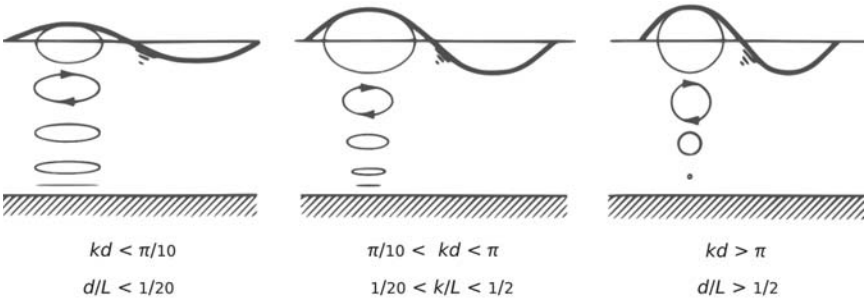

Figure 2.4: Water particle trajectories in progressive waves for different relative water depths [7].

2.6 Profile extension methods

Linear wave theory as introduced in the previous sections is only able to describe the kinematics up to MSL. This is the case since the wave amplitude is assumed to be small and therefore the variation above MSL to be negligible. However, large discrepancies have been found between measurements and linear theory around MSL. Due to the exponential vertical variation in the kinematics, it is actually of great importance to get an accurate estimate of the kinematics and the corresponding loads around MSL. For this reason a need arises for the development of a more accurate model in order to provide more detail. A number of methods have been formulated, varying in complexity and accuracy. Some of the most common models are discussed below:

Constant extrapolation

Constant extrapolation is a linear method that simply uses a vertical extrapolation of the linear Airy theory. The value for the kinematics at MSL ($z = 0$) is extrapolated up to the free surface in a constant way. The equation describing this procedure is the following:

$$u(x,z,t) = \begin{cases} u(x,z,t) & z \leq 0 \\ u(x,0,t) & 0 \leq z \leq \eta \end{cases} \tag{2.16}$$

Wheeler stretching

Wheeler stretching is also based on Airy theory but some nonlinear effects are included by stretching the vertical coordinate z up to the instantaneous surface elevation η. The horizontal velocity is now expressed in terms of the this stretched coordinate z':

$$u(x, z, t) = u(x, z', t) \quad 0 \leq z \leq \eta \tag{2.17}$$

With

$$z' = \frac{z - \eta}{1 + \dfrac{\eta}{d}} \tag{2.18}$$

The method was developed by Wheeler in 1969 [46] and is widely used in the offshore industry.

Second-order kinematics model

The second-order kinematics model is based on the irregular wave model described in section 2.8.2 and to avoid confusion is hereafter referred to as the "Taylor expansion model". It is based on the principle that the second-order effects present in an irregular wave can be expressed in terms of sum and difference components. The kinematics model uses a Taylor expansion of the linear velocity profile. In this way, the second-order horizontal velocity may be written as the sum of the linear term $u^{(1)}$ and the second order contributions:

$$u(z) = \begin{cases} u^{(1)}(z) + u^{(2,\text{sum})}(z) + u^{(2,\text{diff})}(z) & z \leq 0 \\ u_0 + \left.\dfrac{\partial u^{(1)}}{\partial z}\right|_{z=0} \cdot z + u^{(2,\text{sum})}(0) + u^{(2,\text{diff})}(0) & z > 0 \end{cases} \tag{2.19}$$

The second line of equation 2.19 demonstrates how the second-order kinematics model describes the horizontal velocity above MSL. u_0 is defined as linear velocity at MSL $u^{(1)}(0)$. The second term represents the stretching which stretches the kinematics up to the free surface. The equation is consistent up the the second-order as long as the last two terms are included [38].

Grue's method

Another way to determine the wave kinematics is Grue's method [15]. The method evaluates a time series (measured or simulated) and obtains the crest height $z = \eta_m$ and the corresponding through to through period T_{TT}. A local angular frequency is based on this period as $\omega = 2\pi/T_{TT}$. In order to obtain the local wave number k and the wave slope ϵ, a system of equations is solved numerically, based on third-order Stokes theory:

$$\frac{\omega^2}{gk} = 1 + \epsilon^2 \quad , \quad k\eta_m = \epsilon + \frac{1}{2}\epsilon^2 + \frac{1}{2}\epsilon^3 \tag{2.20}$$

In equation 2.20, the first part represents the nonlinear dispersion relation and the second part expresses the non-dimensional surface elevation. The horizontal velocity under a crest is then given by:

$$u(z) = \epsilon\sqrt{\frac{g}{k}}e^{kz} \tag{2.21}$$

Grue's method is limited to kinematics under a crest and is only valid in deep water.

Comparison
In figure 2.5 the velocity profiles under a crest are shown for the different models.

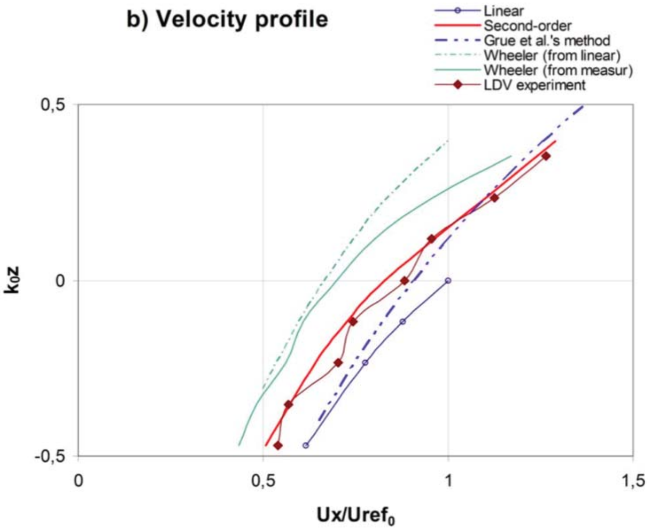

Figure 2.5: Velocity profile comparison for difference extension methods [37].

Stansberg [37] investigated the kinematics under extreme waves. It was concluded that all three nonlinear models predict the maximum velocity reasonably well at the free surface of steep crest, $z = \eta_{max}$. Grue's method works well for $z > 0$ but generally overpredicts for $z < 0$. Wheeler stretching estimates quite well at the free surface using measurements as input, but underpredicts at lower levels. When using a linear input, the same error is also present at the free surface. The second-order kinematics model is concluded to compare best to the experiment.

2.7 Irregular waves

So far only waves with a single frequency have been considered. These are regular waves, also known as monochromatic waves, refers to an effect in light waves which only have one color for a single frequency signal. In this section the concept of irregular waves is introduced. This is necessary since the sea surface can not be described by a regular wave. Rather, a summation of regular waves is used to obtain an expression for the sea surface, consisting of a large variety of waves moving in several directions with different frequencies, amplitudes and phases. The main assumption is that all the individual waves are linear and hence can be superimposed. For now directionality is not considered and the surface elevation for an irregular wave is described by the random-phase/amplitude model:

$$\eta(t) = \sum_{i=1}^{N} \underline{a}_i \cos(2\pi f_i t + \underline{\phi}_i) \tag{2.22}$$

In equation 2.22 N is the number of frequencies and the underscores under the amplitude $\underline{a}_i$ and the phase $\underline{\phi}_i$ indicate that these are random variables. Each of these random variables can be characterized by its corresponding probability density function. The amplitude is Rayleigh distributed at each frequency:

$$p(a_i) = \frac{\pi}{2}\frac{a_i}{\mu_i^2} \exp\left(-\frac{\pi a_i^2}{4\mu_i^2}\right) \quad \text{for} \quad a_i \geq 0 \tag{2.23}$$

The only parameter that varies over the different frequencies is μ_i. This parameter provides the expected value $E\{\}$ or mean value from the Rayleigh distribution. The phase at each frequency is uniformly distributed between 0 and 2π:

$$p(\phi_i) = \frac{1}{2\pi} \quad \text{for} \quad 0 < \phi_i \leq 2\pi \tag{2.24}$$

The above described principle is depicted in figure 2.6. As illustrated, the amplitude spectrum $E\{\underline{a}_i\}$ is constructed by assembling the expected values of the respective Rayleigh distributions. For a given amplitude spectrum, one can generate a realization of the surface elevation $\eta(t)$ by drawing from this amplitude spectrum, i.e. obtaining values for the amplitude and phase from their respective probability density functions. These individual contributions are then summed to obtain the surface elevation. A remark for the use of this model is that it generates a stationary process. Since the sea is in fact not stationary, the wave record needs to be divided into time frames for which the conditions may be assumed to be constant. Furthermore, the random-phase/amplitude model assumes no interaction between the several frequency components. This is a valid assumption for small amplitude waves in deep water but care should be taken for steeper waves or more shallow regions. Finally, the amplitude spectrum is built up from discrete frequencies while

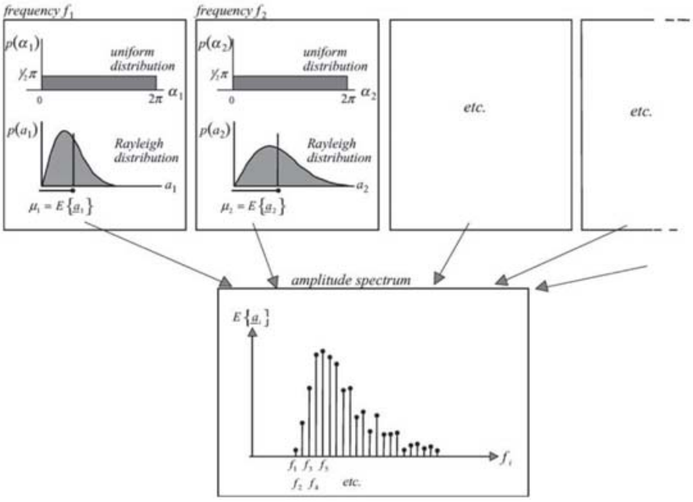

Figure 2.6: Amplitude spectrum build up from individual frequencies with their respective expected value [18].

the sea contains a continuum of frequencies.

The amplitude spectrum provides the basis for the variance spectrum. The latter spectrum is preferred for two reasons. Firstly, the variance $\frac{1}{2}\underline{a}_i^2$ is a more relevant statistical property than the amplitude. Secondly, the energy of the waves is proportional to the variance. Now, to overcome the earlier described problem that not all frequencies can be represented by the discretized spectrum, the variance $E\left\{\frac{1}{2}\underline{a}_i^2\right\}$ is distributed over the frequency interval Δf_i. This yields the variance density spectrum $E^*(f_i)$:

$$E^*(f_i) = \frac{1}{\Delta f_i} E\left\{\tfrac{1}{2}\underline{a}_i^2\right\} \quad \text{for all } f_i \tag{2.25}$$

By introducing the frequency band Δf_i, the spectrum is now able to describe all frequencies. Finally, the discontinuity between two adjacent frequency bands is removed as the width of the frequency goes to zero:

$$E(f) = \lim_{\Delta f \to 0} \frac{1}{\Delta f_i} E\left\{\tfrac{1}{2}\underline{a}_1^2\right\} \tag{2.26}$$

Equation 2.26 is referred to as the variance density spectrum and provides a complete description of the surface elevation. The above described procedure is illustrated graphically in figure 2.7. The equations corresponding to the spectra are displayed in the caption. Note that there is a clear distinction between the expected value $E\{\}$ and the variance density $E^*()$ and $E()$.

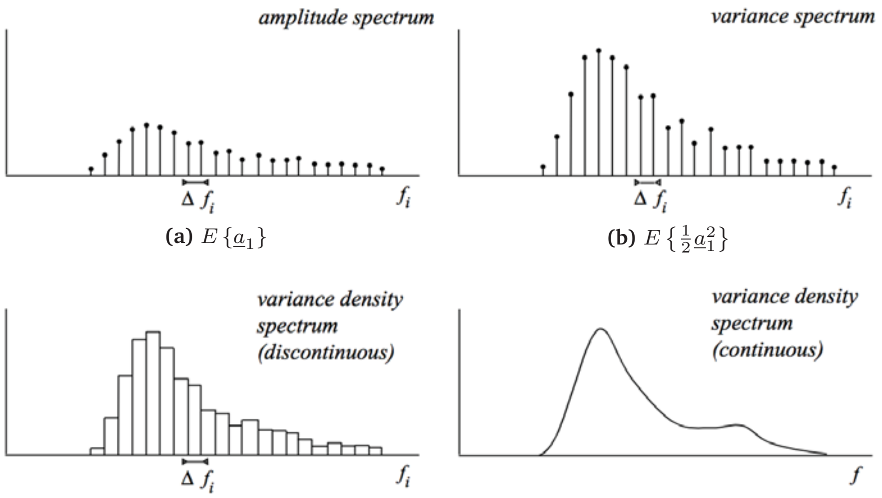

(a) $E\{\underline{a}_1\}$ **(b)** $E\left\{\frac{1}{2}\underline{a}_1^2\right\}$

(c) $\frac{1}{\Delta f_i}E\left\{\frac{1}{2}\underline{a}_1^2\right\}$ **(d)** $E(f) = \lim_{\Delta f \to 0}\frac{1}{\Delta f_i}E\left\{\frac{1}{2}\underline{a}_1^2\right\}$

Figure 2.7: Transformation of discrete amplitude spectrum to continious variance density spectrum [18]

As explained above, the variance density spectrum is preferred to the amplitude spectrum because the wave energy is proportional to the variance. The variance density spectrum can be used to describe the *statistical* properties of the waves whereas energy spectrum is used to describe the *physical* aspects of the wave. To convert to the energy spectrum, the variance density spectrum is mulitplied with ρg:

$$E_{energy}(f) = \rho g E_{variance}(f) \tag{2.27}$$

The width of the spectrum determines the degree of irregularity in the waves. In the extreme case where spectrum consist of a single frequency, the surface elevation is described by a regular wave. However, when the spectrum covers a wide range of frequencies, the surface elevations displays a high level of irregularity.

2.7.1 Directionality

The description given in the previous section of the one-dimensional wave spectrum is a function of time at a single location. In order to make the model three-dimensional, the directional parameter θ needs to be added. A 3D description can be used to describe the surface elevation at different locations, for example at the four legs of a jacket structure. The surface elevation can be rewritten to:

$$\eta(x, y, t) = a\cos(\omega t - kx\cos\theta - ky\sin\theta + \phi) \tag{2.28}$$

Where the wave number k is defined as $k = 2\pi/L$ and the angle θ is the direction of the wave propagation. The random amplitude/phase model can now be extended to the following:

$$\underline{\eta}(x, y, t) = \sum_{i=1}^{N}\sum_{j=1}^{M} \underline{a}_{i,j} \cos\left(\omega t - k_i x\cos\theta_j - k_i y\sin\theta_j + \underline{\phi}_{i,j}\right) \tag{2.29}$$

Because of the addition of two dimensions (x and y), one would also expect two extra summations. However, since the wave number k is directly related to frequency ω through the dispersion relation (2.8), the 3D-model is reduced to a 2D-model. Now the discrete 2D-model is converted to a continuous variance density spectrum, in a similar way as described before. In terms of frequency f, the spectrum is given as:

$$E(f, \theta) = \lim_{\Delta f \to 0} \lim_{\Delta\theta \to 0} \frac{1}{\Delta f \Delta\theta} E\left\{\tfrac{1}{2}\underline{a}^2\right\} \tag{2.30}$$

The spectrum indicates the distribution of the variance $\underline{\eta}(x, y, t)$ over the directions and frequencies.

2.7.2 Wave height and period

For a harmonic wave, the wave height and period are constant and are given by H and T, respectively. For irregular waves however, the superposition of many harmonic waves results in a varying wave height and period. In order to be able to say something about these parameters, the concepts of *mean wave height* and *mean zero crossing wave period* are introduced. These represent the average of all wave height and the time between each downward zero-crossing, respectively:

$$\overline{H} = \frac{1}{N}\sum_{i=1}^{N} H_i \tag{2.31}$$

$$\overline{T}_z = \frac{1}{N}\sum_{i=1}^{N} T_{z_i} \tag{2.32}$$

Another way of quantifying the average wave height is by means of the *significant wave height* H_s. This parameter is defined in the time domain as the average of the highest one-third of the wave heights:

$$H_s = \frac{1}{N/3} \sum_{j=1}^{N/3} H_j \tag{2.33}$$

Where j describes the rank number of the wave height (i.e. $j = 1$ for the highest wave, $j = 2$ for the second highest, etc.) The significant wave height was historically intended to mathematically express the wave height that could be observed by a trained observer. Another very useful advantage is that the significant wave height can be estimated from the wave spectrum. The significant wave height H_{m_0} is defined in the frequency domain in terms of the zeroth moment m_0 of the wave spectrum:

$$H_{m_0} \approx 4\sqrt{m_0} \tag{2.34}$$

Any spectral moment of the wave spectrum $S(f)$ can be obtained from the following relation:

$$m_n = \int_0^\infty f^n S(f)\, df \tag{2.35}$$

2.7.3 Generalized spectral shapes

The fact that an irregular wave can be described by an energy spectrum is a very powerful tool in order to make a compact description of the sea. One of the first spectra that was proposed to describe a sea state was the in 1964 developed Pierson-Moskowitz (PM) spectrum. This concept assumes a uniform, steady wind blowing for a long time (ten-thousand wave periods) over a large area (five-thousand wave lengths). As the sea is subjected to the wind, waves are generated and the wave celerity increases up to the point when it reaches the wind speed. The waves are then considered to be *fully developed*. During the development, the peak frequency, the frequency that carries the most energy, decreases. The PM spectrum is given by equation 2.36:

$$S_{PM}(f) = \alpha_{PM}\, g^2 (2\pi)^{-4} f^{-5} \exp\left[-\frac{5}{4}\left(\frac{f}{f_p}\right)^{-4}\right] \tag{2.36}$$

Where α_{PM} and f_p are the energy scale and the peak frequency, respectively. In the 1970s, the JOint North Sea WAve Project (JONSWAP) conducted a series of extensive measurements. It was concluded that the wave spectrum is never fully developed as the development continues through nonlinear wave-wave interactions [17]. To account for this effect, a peak-enhancement function was added to the PM spectrum. The result is known as the JONSWAP spectrum:

$$S_{JS}(f) = \alpha_{JS}\, g^2 (2\pi)^{-4} f^{-5} \exp\left[-\frac{5}{4}\left(\frac{f}{f_p}\right)^{-4}\right] \gamma^{\exp\left[-\frac{(f-f_p)^2}{2\sigma^2 f_p^2}\right]} \tag{2.37}$$

Where γ is the peak-enhancement factor and σ is the peak-width parameter. When γ is set to unity, the JONSWAP spectrum simplifies to the PM spectrum. The PM spectrum is used for fully developed seas, the JONSWAP spectrum for seas with a limited fetch. Both spectra however describe wind sea conditions. In case a swell is also present, a two peak spectrum may be used, e.g. the spectra proposed by [28] or [40].

2.8 Nonlinear wave models

This section discusses both nonlinear regular and irregular wave models. Since this thesis focuses on fatigue loads and correspondingly the use of an irregular wave model, the regular models are only touched upon briefly. For more information on the nonlinear regular wave models the reader is directed to the corresponding references for a more detailed discussion or to the overview provided in the DNV standard [8].

2.8.1 Nonlinear regular waves

In deep water, where waves generally have low wave steepness H/L, the nonlinear effects in the waves are insignificant and a linear wave model suffices. However, when moving towards more shallow waters, where offshore wind farms are generally located, the nonlinear effects become more pronounced and a linear model is no longer able to accurately describe the motion of the sea. To overcome this problem various nonlinear regular models have been developed to describe these effects [8]. A popular method to describe higher order effects in a wave is *Stokes theory* [13]. This theory is based on the idea that the nonlinear effects can be described by adding higher order pertubations to the linear wave. Other nonlinear regular wave models are for example *Cnoidal wave theory* [47] and *Solitary wave theory* [33]. The drawback of each of these models is that they have limited applicability, depending on the wave height and water depth. An overview of the range of applicability of the different theories is provided in figure 2.8.

Due to the limited range of applicability of the different wave theories, another method has been developed, providing a more general formulation that is able to describe most weakly nonlinear waves. This *Stream function wave theory* owes its name to fact that the theory does not express the kinematics in terms of a velocity potential, but rather uses a *stream function*. This wave theory is used to provide

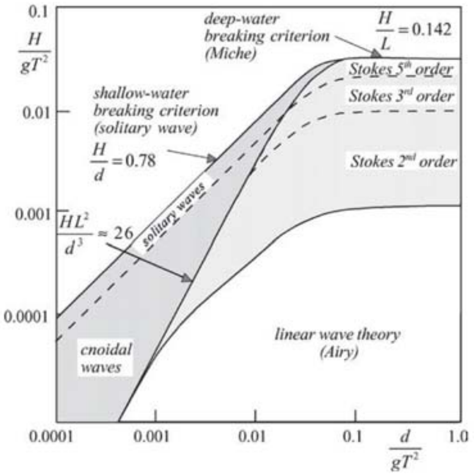

Figure 2.8: Applicability of different nonlinear regular wave models [18].

a numerical alternative to the above described analytical methods and provides a broader range of validity. Furthermore, the stream function is able to describe the wave kinematics up to the free surface whereas Stokes waves are limited to MSL and are thus required to use a profile extension method.

2.8.2 Nonlinear irregular waves

In order to accurately describe the sea surface elevation and corresponding kinematics, both its irregular as well as its nonlinear properties need to be taken into account. The methods described in the previous section are only applicable to regular waves and hence do not include irregularity. Similarly, the method for treating irregular waves (see section 2.7), does not include nonlinearities.

A number of approaches has been developed to accurately describe a nonlinear, irregular sea. One approach that is widely used in different fields of engineering is CFD. This method is not based on potential flow theory but instead generates an approximate solution to the Navier-Stokes equations through a 3D discretization of the flow field. In the field of ocean engineering, this method is particularly useful for simulating breaking waves and/or irregular waves traveling over a complex bathymetry. The downside of the CFD method is that it is very computationally expensive and hence not very practical for running a large amount of design load cases. Another approach to obtain an approximate solution to the governing wave equations is based on the *Boussinesq formulations*. Rather than solving the 3D wave problem numerically, the Boussinesq formulations provide an analytical description of the vertical variation of flow field, thereby reducing the 3D problem to a 2D problem [24].

Despite the advantageous features of these nonlinear irregular methods, their relative complex implementation and computational expense limits their use as engineering tools. Therefore, a simpler nonlinear random wave model is recommended practice for engineering purposes according to the DNV standards [8]. This is the second-order pertubation model by Longuet-Higgins [22], which is an extension of linear wave theory, hence based on potential flow theory. The model was originally formulated for unidirectional waves in infinite water depth. [36] reformulated the expressions to describe short-crested seas. Unidirectional expressions for finite water depth were formulated by [26].

The governing equation is the Laplace equation and the velocity potential Φ is determined by the boundary value problem described in section 2.4. When unidirectional waves are considered, no y-dependency is taken into account. As mentioned before, the model is based on linear Airy wave theory with a second-order pertubation. The velocity potential is formulated accordingly:

$$\Phi(x,z,t) = \Phi^{(1)}(x,z,t) + \Phi^{(2)}(x,z,t) \tag{2.38}$$

Where $\Phi^{(1)}$ is the linear velocity potential and $\Phi^{(2)}$ is the second-order pertubation, consisting of the sum and difference terms. The corresponding surface elevation η is given by:

$$\eta(x,t) = \eta^{(1)}(x,t) + \eta^{(2)}(x,t) \tag{2.39}$$

The linear part of the irregular surface elevation $\eta^{(1)}$ has been discussed in section 2.7. Its unidirectional formulation is repeated here:

$$\eta^{(1)}(x,t) = \sum_{i=1}^{N} a_i \cos(\psi_i) \tag{2.40}$$

Where the argument of the cosine has been abbreviated by $\psi_i = k_i x - \omega_i t + \phi_i$. The second-order contribution to the surface elevation is given by equation 2.41:

$$\eta^{(2)}(x,t) = \sum_{n=1}^{N} \sum_{m=1}^{N} a_n a_m \left\{ B^{-}_{mn} \cos(\psi_n - \psi_m) + B^{+}_{mn} \cos(\psi_n + \psi_m) \right\} \tag{2.41}$$

In equation 2.41 the B^{+} and B^{-} terms represent the transfer functions of the sum- and difference-contributions of the second order. The expressions for these parameters are presented in chapter 4 which discusses the implementation of the second-order pertubation model. The sum- and difference-contributions of the second order are pertubations to the first-order wave and hence travel *phase-locked* with the linear wave. The pertubations cause the shape of the linear wave adjust and show sharper crests and flatter troughs.

2.9 Morison equation

The Morison equation is a semi-empirical formula that is used to calculated hydrodynamic forces on circular cylindrical structural members of offshore structures. It calculates the in-line force, i.e. along the wave direction and normal to the cylinder axis. The equation consists of an inertia term F_I, in phase with the acceleration, and a drag term F_D, in phase with the velocity. The Morison equation in terms of force per strip length dz is given by:

$$dF = \underbrace{\rho C_M \frac{\pi D^2}{4} \dot{u} dz}_{dF_I} + \underbrace{\frac{1}{2} \rho C_D D u |u| dz}_{dF_D} \tag{2.42}$$

The force is calculated at the center point of each strip. The Morison equation assumes the cross-flow principle, i.e. no force contributions are taken into account due to tangential velocity and acceleration, only horizontal contributions [12]. The drag force is the in-line viscous force, acting along the direction of wave propagation. In order to investigate the formulation of the inertia force, the excitation force on a generic strip according to potential flow with long-wave approximation is considered. Long-wave approximation can be used when the structure volume small relative to the wave length, i.e. $\lambda/D > 5$. This is illustrated graphically in figure 2.9.

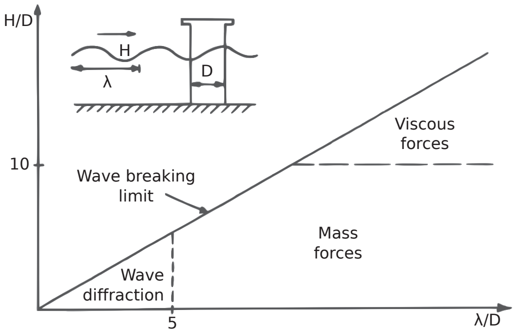

Figure 2.9: Relative importance of diffraction, inertia and viscous forces on marine structures [12].

Now considering the excitation force on a generic strip:

$$dF = \rho A\dot{u}dz + A_{11}\dot{u}dz \tag{2.43}$$

Where A_{11} is the added mass in an infinite fluid and is given by $A_{11} = \rho(\pi D^2/4)$. The added mass can be related to the force that is required to accelerate the fluid surrounding the body. Using the expression for A_{11}, equation 2.43 simplifies to:

$$dF = \rho\frac{\pi D^2}{4}\dot{u}dz + \rho\frac{\pi D^2}{4}\dot{u}dz = 2\rho\frac{\pi D^2}{4}\dot{u}dz \tag{2.44}$$

Comparing equation 2.44 to the inertia part of the Morison equation, it can be seen that they are equal for $C_m = 2$. The mass coefficient C_m is given by:

$$C_m = C_a + 1 \tag{2.45}$$

Where C_a is the added mass coefficient. The maximum value for C_a for a circular cylinder is equal to 1. It can thus be seen that the Morison equation describes the correct excitation force on the body according to potential theory for the asymptotic condition of large λ/D. Hence, it is concluded that the Morison equation is a long-wave approximation and therefore neglects diffraction effects. When a fluid-structure problem is characterized by $\lambda/D < 5$, a correction should be applied to account for diffraction effects. The value for the drag and inertia coefficient do not only depend on the structural properties of the member, but also on the properties of the flow. Important parameters are the Reynolds number and the Keulegan-Carpenter number. For more detail on the influence of these parameters the reader is referred to [8].

Using the deep water expressions for the horizontal velocity and acceleration, the inertia and the drag force have a vertical variation of e^{kz} and e^{2kz}, respectively. Hence, both forces are more pronounced near the free surface, where the drag force has an even higher concentration than the inertia force. This demonstrates the importance of an accurate extrapolation method of the wave kinematics in this region. Especially when considering drag dominated structures such as a jacket, a potential error in the horizontal velocity comes augmented in the drag force due to the fact that it is quadratically proportional.

3

Structural modeling

3.1 Introduction

Where chapter 2 provided theoretical background on the wave modeling practices, this chapter goes into detail in the field of structural modeling. As described in the thesis objective, the goal is to develop an accurate and efficient method to calculate the structural response of the jacket structure. Due to the relatively large number of degrees of freedom (DoF) in the jacket foundation, an increase in computational efficiency is envisioned to come from the use of reduced structural models. For that reason this chapter focuses on the field of domain decomposition and the corresponding model reduction techniques.

To start off, an introduction is given in section 3.2 to provide some context for the use of model reduction techniques. Section 3.3 treats the basics of the use of a finite element (FE) model and explains how different substructures can be coupled in the physical domain. Next, section 3.4 introduces the concept of model reduction and the different methods are described in section 3.5. A way to enhance the performance of a reduced model is to use Modal Truncation Augmentation (MTA). This principle is explained in section 3.6 and applied to the Craig-Bampton method in section 3.7.

3.2 Domain decomposition

The motivation behind domain decomposition is to generate a method that is able to analyze a complex problem, by considering the problems of its components, and the interface between these components separately. This approach is an implementation of the old "divide and conquer" principle. Schwarz [34] pioneered this idea in 1890 by defining an iterative procedure based on domain decomposition. He applied his method to find the solution of the combined domain of a circular and a rectangular component, of which the analytical solution to the separate domains was known. Unfortunately, the domains of most engineering problems are too complex to find an analytical solution for the continuous coupled components. This issue gave rise to the development of discretization techniques such as the boundary element method (BEM) and the finite element method (FEM). These numerical methods provide an approximate solution to partial differential equations, governing the complex problem. Observing figure 3.1, both the discretization methods (left) and Schwarz' method (right) are considered "level 1" domain decomposition techniques.

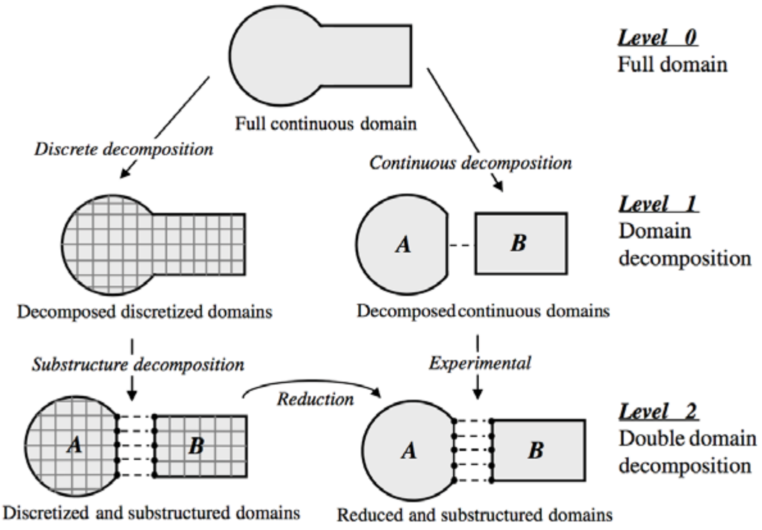

Figure 3.1: An overview of domain decomposition methods [6].

Figure 3.1 also illustrates the substructure decomposition technique, the step from the decomposed discretized domains (level 1) to the discretized and substructured domains (level 2). This approach of analyzing the subdomains/components and reassembling them to form the complete structure has several advantages:

- Dynamic behavior of large and/or complex systems can be analyzed, which would otherwise be very time consuming or even impossible.
- Local dynamic behavior is more easily recognized than in a full model analysis.
- Optimization is done on a component level.
- Modeled components (discretized or analytical) can be combined with experimentally determined components.

- Possibility of parallel computing of the different components.
- Fast reanalysis when only certain components require modification.

In order to ensure an even more efficient analysis, the individual component models are often subjected to model reduction, again see figure 3.1. In this procedure the DoF of the component models are reduced to a certain number of generalized DoF. The latter generally describe the displacement shapes of the component, based on its static and dynamic properties. This procedure of reducing component models was first applied by Hurty [19] and Gladwell [14] in the early 1960s. More advanced and generalized methods were consequently developed by Craig and Bampton [5], MacNeal [23] and Rubin [32].

According to the general framework for domain decomposition, as described in [6], dynamic systems can be represented in three domains. The first domain is the *physical domain*, in which the structure is represented by a mass, damping and stiffness matrix. In the *modal domain*, the structure's dynamic behavior is captured in a superposition of response modes. The physical domain is transformed to the modal domain through an eigenvalue analysis. Both the physical and the modal domain belong to the time to domain. The third possible domain is the *frequency domain*, which is obtained by performing a Fourier transform on the dynamic system in the physical domain. The frequency domain is useful for determining dynamic behavior from experiments, where the input is related to the output through frequency response functions (FRF). For this thesis only coupling in the time domain is of interest and is therefore explained in section 3.3.

3.3 Coupling in the time domain

As stated before, in the time domain the mechanical and geometrical properties of the system are represented by a mass, damping and stiffness matrix. The "level 1" discretization is often accomplished using an FE model which results in discrete matrices. The equations of motion of a linear(ized) component are given by:

$$\boldsymbol{M}^{(s)}\ddot{\boldsymbol{u}}^{(s)}(t) + \boldsymbol{C}^{(s)}\dot{\boldsymbol{u}}^{(s)}(t) + \boldsymbol{K}^{(s)}\boldsymbol{u}^{(s)}(t) = \boldsymbol{f}^{(s)}(t) + \boldsymbol{g}^{(s)}(t) \tag{3.1}$$

Where the mass, damping and stiffness matrices of the substructure/component s, are represented by $\boldsymbol{M}^{(s)}$, $\boldsymbol{C}^{(s)}$ and $\boldsymbol{K}^{(s)}$ respectively. The component DoF are collocated in the vector $\boldsymbol{u}^{(s)}(t)$ (displacement), and the vectors $\dot{\boldsymbol{u}}^{(s)}(t)$ (velocity) and $\ddot{\boldsymbol{u}}^{(s)}(t)$ (acceleration) are its first two time derivatives. On the right hand side of equation 3.1, $\boldsymbol{f}^{(s)}(t)$ represents the external force vector and $\boldsymbol{g}^{(s)}(t)$ is the interface force vector, associated with the compatibility conditions.

When considering n uncoupled components, the equations of motion can be written in block-diagonal format:

$$\boldsymbol{M}\ddot{\boldsymbol{u}} + \boldsymbol{C}\dot{\boldsymbol{u}} + \boldsymbol{K}\boldsymbol{u} = \boldsymbol{f} + \boldsymbol{g} \tag{3.2}$$

With

$$\begin{aligned}
\boldsymbol{M} &\triangleq \text{diag}(\boldsymbol{M}^{(1)}, \dots, \boldsymbol{M}^{(n)}) = \begin{bmatrix} \boldsymbol{M}^{(1)} & & \\ & \ddots & \\ & & \boldsymbol{M}^{(n)} \end{bmatrix} \\
\boldsymbol{C} &\triangleq \text{diag}(\boldsymbol{C}^{(1)}, \dots, \boldsymbol{C}^{(n)}) \\
\boldsymbol{K} &\triangleq \text{diag}(\boldsymbol{K}^{(1)}, \dots, \boldsymbol{K}^{(n)}) \\
\boldsymbol{u} &\triangleq \begin{bmatrix} \boldsymbol{u}^{(1)} \\ \vdots \\ \boldsymbol{u}^{(n)} \end{bmatrix}, \qquad \boldsymbol{f} \triangleq \begin{bmatrix} \boldsymbol{f}^{(1)} \\ \vdots \\ \boldsymbol{f}^{(n)} \end{bmatrix}, \qquad \boldsymbol{g} \triangleq \begin{bmatrix} \boldsymbol{g}^{(1)} \\ \vdots \\ \boldsymbol{g}^{(n)} \end{bmatrix}
\end{aligned}$$

When considering the assembly of component models, the following two conditions should hold:

1. *Interface compatibility*: the displacements along the interface of component 1 are equal to the interface displacements of neighboring component 2:
2. *Equilibrium condition*: the interface forces of the two components must be in equilibrium.

The interface compatibility can be expressed in matrix notation as follows:

$$\boldsymbol{B}\boldsymbol{u} = \boldsymbol{0} \tag{3.3}$$

The $\boldsymbol{B}$ matrix operates on the interface DoF. If the interface DoF of the two components match (conforming), then the $\boldsymbol{B}$ matrix is a signed Boolean matrix. When the interface DoF do not match (non-conforming), nodal collocation can be used in order to ensure interface compatibility. In this case, the $\boldsymbol{B}$ matrix is no longer Boolean. Whether the $\boldsymbol{B}$ is Boolean or not, it can always be used to express the compatibility condition. In the case that $\boldsymbol{B}$ is a signed Boolean matrix, it implies that the displacement of the interface DoF of the two components must be the same, i.e. $\boldsymbol{u}^{(1)} = \boldsymbol{u}^{(2)}$.

The equilibrium condition can be expressed in matrix notation as follows:

$$\boldsymbol{L}^T\boldsymbol{g} = \boldsymbol{0} \tag{3.4}$$

The $\boldsymbol{L}$ matrix localizes the interface DoF of the substructures with respect to the global DoF. According to the equilibrium condition, the interface (boundary) forces of the two components musts balance each other out, i.e. $\boldsymbol{g}_b^{(1)} + \boldsymbol{g}_b^{(2)} = \boldsymbol{0}$.

Using the above defined boundary conditions, the complete system of equations is given by:

$$\begin{cases} \boldsymbol{M}\ddot{\boldsymbol{u}} + \boldsymbol{C}\dot{\boldsymbol{u}} + \boldsymbol{K}\boldsymbol{u} = \boldsymbol{f} + \boldsymbol{g} \\ \boldsymbol{B}\boldsymbol{u} = \boldsymbol{0} \\ \boldsymbol{L}^T\boldsymbol{g} = \boldsymbol{0} \end{cases} \tag{3.5}$$

Equation 3.5 describes the coupling between any number of components, where the unknowns are the displacements $\boldsymbol{u}$ and the interface forces $\boldsymbol{g}$. With the system of equations defined, the next step is to consider the assembly of the components. Assembling components using *primal assembly* is discussed below.

Primal assembly

The primal assembly technique is based on the definition of a unique set of interface DoF q, while eliminating the interface forces as unknowns. For conforming meshes, this is achieved by selecting the unique DoF from the double set of interface DoF from both components. This definition can be described by:

$$\boldsymbol{u} = \boldsymbol{L}\boldsymbol{q} \tag{3.6}$$

Where $\boldsymbol{L}$ is the previously defined Boolean matrix. Because of the fact that the vector $\boldsymbol{q}$ contains a unique set of DoF, the compatibility condition (equation 3.3) is automatically satisfied for any set of $\boldsymbol{q}$:

$$\boldsymbol{B}\boldsymbol{u} = \boldsymbol{B}\boldsymbol{L}\boldsymbol{q} = \boldsymbol{0} \quad \forall\, \boldsymbol{q} \tag{3.7}$$

This means that the two Boolean matrices are actually each other's null spaces:

$$\begin{cases} \boldsymbol{L} & = & \text{null}(\boldsymbol{B}) \\ \boldsymbol{B}^T & = & \text{null}(\boldsymbol{L}^T) \end{cases} \tag{3.8}$$

This is a convenient property for computational purposes, as only one of the two matrices needs to be explicitly defined. The compatibility condition drops out of the system of equations as it is satisfied by the choice of $\boldsymbol{q}$, and equation 3.5 reduces to:

$$\begin{cases} \boldsymbol{M}\boldsymbol{L}\ddot{\boldsymbol{q}} + \boldsymbol{C}\boldsymbol{L}\dot{\boldsymbol{q}} + \boldsymbol{K}\boldsymbol{L}\boldsymbol{q} = \boldsymbol{f} + \boldsymbol{g} \\ \boldsymbol{L}^T\boldsymbol{g} = \boldsymbol{0} \end{cases} \tag{3.9}$$

By premultiplication of equation 3.9 with $\boldsymbol{L}^T$, the equilibrium condition is satisfied and symmetric matrices are obtained:

$$\bar{\boldsymbol{M}}\ddot{\boldsymbol{q}} + \bar{\boldsymbol{C}}\dot{\boldsymbol{q}} + \bar{\boldsymbol{K}}\boldsymbol{q} = \bar{\boldsymbol{f}} \tag{3.10}$$

With

$$\begin{cases} \bar{\boldsymbol{M}} & \triangleq & \boldsymbol{L}^T\boldsymbol{M}\boldsymbol{L} \\ \bar{\boldsymbol{C}} & \triangleq & \boldsymbol{L}^T\boldsymbol{C}\boldsymbol{L} \\ \bar{\boldsymbol{K}} & \triangleq & \boldsymbol{L}^T\boldsymbol{K}\boldsymbol{L} \\ \bar{\boldsymbol{f}} & \triangleq & \boldsymbol{L}^T\boldsymbol{f} \end{cases}$$

3.4 Component model reduction

Referring to figure 3.1, it is recalled that the "level 1" decomposition often entails the generation of a FE model, while the "level 2" decomposition is the structure's division into component models. This section treats the final step in the domain decomposition procedure, namely the reduction of the component models.

The basis of a component model is generally formed by an FE model, which is used to calculate stresses, strains and displacements. Depending on the geometry, the FE model often contains a high level of detail, required to capture local phenomena. The dynamic behavior of the component occurs on a more global scale, hence this level of mesh refinement is not necessary, or even desired, for a dynamic analysis. In the design procedure of a wind turbine over 10.000 dynamic simulations need to be run for all the different design load cases. One quickly understands the need for a computationally efficient dynamic model.

A solution to decrease computational time could be to use a coarser mesh. However, coarsening the existing mesh can be time consuming and also introduces artificial stiffness as the reduction of DoF limits the component's ability to deform. This problem triggered the development of an alternative way to describe the component's response, namely by a reduced set of generalized DoF that represents the amplitudes of a selected set of displacement shapes. Originally, only eigenmodes of the component were used and the method became known as *component mode synthesis* (CMS). Nowadays, CMS has a broader definition where the method comprises some kind of modal analysis on the substructure, of which the obtained modal vectors are used to reduce the equations of motion from the physical to the modal domain [6]. The collection of modal vectors is referred to as the *reduction basis* and often contains a description of the component's static response and/or dynamic component mode shapes. In vector notation, the model reduction can be represented by:

$$\boldsymbol{u} = \boldsymbol{R}\boldsymbol{q} \tag{3.11}$$

Where the vector $\boldsymbol{u}$ $[n \times 1]$ contains all the original DoF of the system, the matrix $\boldsymbol{R}$ $[n \times r]$ is the reduction basis, containing the selected modes, and the vector $\boldsymbol{q}$ $[r \times 1]$ contains the generalized DoF which represent the amplitude of the corresponding modes. The dimensions n and r represent the number of original and generalized DoF, where generally $r \ll n$. The level to which the reduced system of equations is able to accurately represent the response, is dependent on how well the selected modes in $\boldsymbol{R}$ match the exact solution. The reduced system of equations is derived here. The linear(ized) equation of motion of a discretized substructure s was already presented in equation 3.1, but is repeated here for convenience. The time dependency is dropped for a clearer notation:

$$\boldsymbol{M}^{(s)}\ddot{\boldsymbol{u}} + \boldsymbol{C}^{(s)}\dot{\boldsymbol{u}}^{(s)} + \boldsymbol{K}^{(s)}\boldsymbol{u}^{(s)} = \boldsymbol{f}^{(s)} + \boldsymbol{g}^{(s)} \tag{3.12}$$

Inserting equation 3.11 into 3.12 yields the following expression:

$$\boldsymbol{M}^{(s)}\boldsymbol{R}^{(s)}\ddot{\boldsymbol{q}}^{(s)} + \boldsymbol{C}^{(s)}\boldsymbol{R}^{(s)}\dot{\boldsymbol{q}}^{(s)} + \boldsymbol{K}^{(s)}\boldsymbol{R}^{(s)}\boldsymbol{q}^{(s)} = \boldsymbol{f}^{(s)} + \boldsymbol{g}^{(s)} + \boldsymbol{r}^{(s)} \tag{3.13}$$

Where the vector $\boldsymbol{r}^{(s)}$ describes the residual force that comes into play due to modal truncation, i.e. not all eigenmodes are considered in $\boldsymbol{R}$. It is noted that when the full set of eigenmodes is used ($r = n$), the exact solutions is found and the reduction merely becomes a transformation to modal coordinates. However, this clearly defeats the purpose of reduction as the number of coordinates remains the same. To allow for the error that the residual force introduces, it is imposed that $\boldsymbol{r}^{(s)}$ must be zero in the reduction space:

$$\boldsymbol{R}^{(s)T}\boldsymbol{r}^{(s)} = \boldsymbol{0} \tag{3.14}$$

By premultiplying equation 3.14 with $\boldsymbol{R}^{(s)T}$, the reduced system of equations is obtained:

$$\tilde{\boldsymbol{M}}^{(s)}\ddot{\boldsymbol{q}}^{(s)} + \tilde{\boldsymbol{C}}^{(s)}\dot{\boldsymbol{q}}^{(s)} + \tilde{\boldsymbol{K}}^{(s)}\boldsymbol{q}^{(s)} = \tilde{\boldsymbol{f}}^{(s)} + \tilde{\boldsymbol{g}}^{(s)} \tag{3.15}$$

Where the reduced matrices and vectors are given by:

$$\begin{cases} \tilde{\boldsymbol{M}}^{(s)} & = & \boldsymbol{R}^{(s)T}\boldsymbol{M}^{(s)}\boldsymbol{R}^{(s)} \\ \tilde{\boldsymbol{C}}^{(s)} & = & \boldsymbol{R}^{(s)T}\boldsymbol{C}^{(s)}\boldsymbol{R}^{(s)} \\ \tilde{\boldsymbol{K}}^{(s)} & = & \boldsymbol{R}^{(s)T}\boldsymbol{K}^{(s)}\boldsymbol{R}^{(s)} \\ \tilde{\boldsymbol{f}}^{(s)} & = & \boldsymbol{R}^{(s)T}\boldsymbol{f}^{(s)} \\ \tilde{\boldsymbol{g}}^{(s)} & = & \boldsymbol{R}^{(s)T}\boldsymbol{g}^{(s)} \end{cases}$$

3.5 Model reduction methods

As discussed in section 3.4, the goal of model reduction is to obtain a reduced set of equations, based on the reduction basis $\boldsymbol{R}$, that accurately approximates the full model. The shapes contained in this matrix depend on the reduction method that is used. This section discusses two of the most popular reduction methods; the Guyan method and the Craig-Bampton method. The equations for the different methods are derived without damping and the superscript $^{(s)}$ is omitted for simplicity. This yields the equations of motion in the following format:

$$\boldsymbol{M}\ddot{\boldsymbol{u}} + \boldsymbol{K}\boldsymbol{u} = \boldsymbol{f} + \boldsymbol{g} \tag{3.16}$$

The different model reduction techniques are illustrated by an example of a 2D cantilever beam. A representation of the continuous model is presented in figure 3.2a. In order to able to solve the beam problem numerically, a FE model of the beam is made, which is depicted in figure 3.2b. In this 2D cantilever beam model each of the nodes has three DoF: two translational (axial and transverse) and one rotational DoF. Since the first node is clamped, the current structure consists of nine internal DoF and three boundary DoF. In the FE model it can be observed that a distinction is made between internal DoF $\boldsymbol{u}_i$ and boundary DoF $\boldsymbol{u}_b$. Both the Guyan method and the Craig-Bampton method are based on this division.

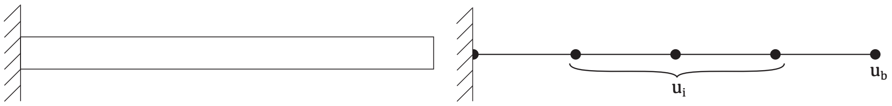

(a) Continuous model. **(b)** FE model.

Figure 3.2: Continuous and FE model of a cantilever beam.

3.5.1 Guyan method

The Guyan method was proposed by R.J. Guyan in 1965 [16] and is nowadays still widely used in the field of structural dynamics. The principle of the method is that it includes only static constraint modes in the reduction basis. The static constraint modes describe the static response of the internal DoF due to a unit displacement of one of the interface DoF, while the other interface DoF are restrained. Furthermore, no external force is applied to the internal DoF. Following the example of the cantilever beam, the three static constraint modes are illustrated in figure 3.3a to 3.3c.

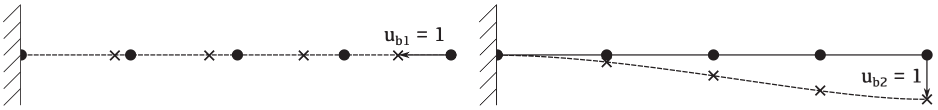

(a) Static constraint mode shape 1. **(b)** Static constraint mode shape 2.

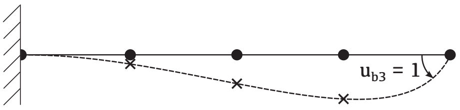

(c) Static constraint mode shape 3.

Figure 3.3: Static constraint modes of a cantilever beam.

In order to compute these modes, the equations of motion are split accordingly to the division of the DoF:

$$\begin{bmatrix} \boldsymbol{M}_{bb} & \boldsymbol{M}_{bi} \\ \boldsymbol{M}_{ib} & \boldsymbol{M}_{ii} \end{bmatrix} \begin{bmatrix} \ddot{\boldsymbol{u}}_b \\ \ddot{\boldsymbol{u}}_i \end{bmatrix} + \begin{bmatrix} \boldsymbol{K}_{bb} & \boldsymbol{K}_{bi} \\ \boldsymbol{K}_{ib} & \boldsymbol{K}_{ii} \end{bmatrix} \begin{bmatrix} \boldsymbol{u}_b \\ \boldsymbol{u}_i \end{bmatrix} = \begin{bmatrix} \boldsymbol{f}_b \\ \boldsymbol{f}_i \end{bmatrix} + \begin{bmatrix} \boldsymbol{g}_b \\ \boldsymbol{0} \end{bmatrix} \tag{3.17}$$

As stated before, it is assumed that no external force acts on the internal DoF, hence $\boldsymbol{f}_i = 0$. The second line of equation 3.17 therefore reduces to:

$$\boldsymbol{M}_{ii}\ddot{\boldsymbol{u}}_i + \boldsymbol{K}_{ii}\boldsymbol{u}_i = -\boldsymbol{M}_{ib}\ddot{\boldsymbol{u}}_b - \boldsymbol{K}_{ib}\boldsymbol{u}_b \tag{3.18}$$

Next, the response of the internal DoF is split into a static and a dynamic contribution:

$$\boldsymbol{u}_i = \boldsymbol{u}_{i,stat} + \boldsymbol{u}_{i,dyn} \tag{3.19}$$

Since the modes under consideration are static, only $\boldsymbol{u}_{i,stat}$ is considered and the inertia forces are neglected by setting $\ddot{\boldsymbol{u}}_i$ and $\ddot{\boldsymbol{u}}_b$ to zero. The static response is then given by:

$$\boldsymbol{u}_{i,stat} = -\boldsymbol{K}_{ii}^{-1}\boldsymbol{K}_{ib}\boldsymbol{u}_b = \boldsymbol{\Psi}_{C,i}\boldsymbol{u}_b \tag{3.20}$$

Here the matrix $\boldsymbol{\Psi}_{C,i}$ is introduced which is referred to as the *static condensation matrix*. The columns of the matrix contain the static mode shapes, induced by a unit displacement in the corresponding boundary DoF. The total static response of the system can now be written as:

$$\begin{bmatrix} \boldsymbol{u}_b \\ \boldsymbol{u}_i \end{bmatrix} = \begin{bmatrix} \boldsymbol{I} \\ -\boldsymbol{K}_{ii}^{-1}\boldsymbol{K}_{ib} \end{bmatrix} \boldsymbol{u}_b = \boldsymbol{\Psi}_C\boldsymbol{u}_b \tag{3.21}$$

The matrix $\boldsymbol{\Psi}_C$, containing the static mode shapes, in fact represents the reduction basis of the Guyan method, i.e. $\boldsymbol{R}_G = \boldsymbol{\Psi}_C$. Inserting the reduction basis into equation 3.17 yields the following reduced equations of motion:

$$\tilde{\boldsymbol{M}}\ddot{\boldsymbol{u}}_b + \tilde{\boldsymbol{K}}\boldsymbol{u}_b = \tilde{\boldsymbol{f}}_b \tag{3.22}$$

Where

$$\begin{cases} \tilde{\boldsymbol{M}} & = \boldsymbol{R}_G^T \boldsymbol{M} \boldsymbol{R}_G \\ \tilde{\boldsymbol{K}} & = \boldsymbol{R}_G^T \boldsymbol{K} \boldsymbol{R}_G \\ \tilde{\boldsymbol{f}} & = \boldsymbol{R}_G^T \boldsymbol{f} \end{cases}$$

It is noted that the system is reduced from the original amount of DoF $\boldsymbol{u}$ to only the interface DoF $\boldsymbol{u}_b$. The Guyan method is able compute exactly the internal response due to a static force on the boundary. However, the fact the inertia forces are condensed at the boundary implies that they can only contribute in a quasi-static way, thereby strongly approximating any dynamic behavior. The Guyan method only gives an accurate response when frequency one wants to compute for the entire system is much lower than the first eigenfrequency of the system when clamped at the interface [43].

This is one of the major limitations of the Guyan method. In order to yield a more accurate representation of the structure's dynamic response, additional dynamic information is required in the reduction basis. The Craig-Bampton method, described in section 3.5.2 provides a solution to this problem.

3.5.2 Craig-Bampton method

The Craig-Bampton method [5] is an extension of the Guyan method. By including fixed interface vibration modes in the reduction basis, the Craig-Bampton method adds important dynamic information and thereby overcomes the major drawback of the Guyan method. The Craig-Bampton method owes its popularity to the accurate reduction basis and straightforward implementation. Figure 3.4 graphically illustrates the first two fixed interface vibration modes of the cantilever beam. It can be observed that, unlike the case for the static constraint modes, the boundary node is now fixed.

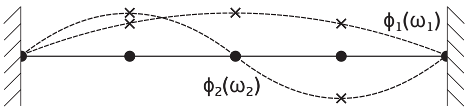

Figure 3.4: First two fixed interface vibration modes of a cantilever beam.

The fixed interface vibration modes describe the natural vibration shapes of the structure for the case when the boundary is clamped. These modes ϕ_i have a corresponding frequency ω_i, as is shown in figure 3.4. Similar to the static constraint modes, no external force is applied to the internal DoF. Using equation 3.17 as the starting point, it is again assumed that $\boldsymbol{f}_i = 0$ and the interface is fixed by enforcing $\boldsymbol{u}_b = 0$. The second line of the equations of motion then reads:

$$\boldsymbol{M}_{ii}\ddot{\boldsymbol{u}}_i + \boldsymbol{K}_{ii}\boldsymbol{u}_i = \boldsymbol{0} \tag{3.23}$$

In order to find the internal response $\boldsymbol{u}_i$, the nontrivial solution of the eigenvalue problem is required:

$$\left(\boldsymbol{K}_{ii} - \omega_{i,n}^2 \boldsymbol{M}_{ii}\right) \phi_{i,n} = \boldsymbol{0} \tag{3.24}$$

In equation 3.24 $\phi_{i,n}$ represents the n^{th} fixed interface vibration mode and $\omega_{i,n}$ is the corresponding eigenfrequency. As for the Guyan method, the internal DoF are split into a static and a dynamic part. Now, instead of neglecting the dynamic part, $\boldsymbol{u}_{i,dyn}$ is retained and can be approximated by the superposition of a truncated number of vibration modes:

$$\boldsymbol{u}_{i,dyn} \approx \sum_{n=1}^{m} \phi_{i,n}\eta_{i,n} = \boldsymbol{\Phi}_i \boldsymbol{\eta}_i \tag{3.25}$$

The matrix $\boldsymbol{\Phi}_i$ is the collection of all n included fixed vibration modes $\phi_{i,n}$ and the vector $\boldsymbol{\eta}_i$ contains the corresponding modal amplitudes. Combining equation 3.20 and 3.25, the response of the internal DoF can be written as:

$$\boldsymbol{u}_i \approx \boldsymbol{\Psi}_{C,i}\boldsymbol{u}_b + \boldsymbol{\Phi}_i \boldsymbol{\eta}_i \tag{3.26}$$

Rewriting equation 3.26 into matrix notation yields the CB reduction basis $\boldsymbol{R}_{CB}$:

$$\begin{bmatrix} \boldsymbol{u}_b \\ \boldsymbol{u}_i \end{bmatrix} \approx \begin{bmatrix} \boldsymbol{I} & \boldsymbol{0} \\ \boldsymbol{\Psi}_{C,i} & \boldsymbol{\Phi}_i \end{bmatrix} \begin{bmatrix} \boldsymbol{u}_b \\ \boldsymbol{\eta}_i \end{bmatrix} = \boldsymbol{R}_{CB}\boldsymbol{q} \tag{3.27}$$

Finally, the reduced system of equations is obtained:

$$\tilde{\boldsymbol{M}}\ddot{\boldsymbol{q}} + \tilde{\boldsymbol{K}}\boldsymbol{q} = \tilde{\boldsymbol{f}} \tag{3.28}$$

The reduced mass and stiffness matrix and the external force vector are again obtained by premultiplying with the transpose of the reduction basis $\boldsymbol{R}_{CB}^T$:

$$\begin{cases} \tilde{\boldsymbol{M}} & = & \boldsymbol{R}_{CB}^T \boldsymbol{M} \boldsymbol{R}_{CB} \\ \tilde{\boldsymbol{K}} & = & \boldsymbol{R}_{CB}^T \boldsymbol{K} \boldsymbol{R}_{CB} \\ \tilde{\boldsymbol{f}} & = & \boldsymbol{R}_{CB}^T \boldsymbol{f} \end{cases}$$

Where $\tilde{\boldsymbol{M}}$, $\tilde{\boldsymbol{K}}$ and $\tilde{\boldsymbol{f}}$ have the following form:

$$\begin{aligned}
\tilde{\boldsymbol{K}} &= \begin{bmatrix} \tilde{\boldsymbol{K}}_{bb} & \boldsymbol{0} \\ \boldsymbol{0} & \boldsymbol{\Omega}_i^2 \end{bmatrix} \\
\tilde{\boldsymbol{K}}_{bb} &= \boldsymbol{K}_{bb} - \boldsymbol{K}_{bi}\boldsymbol{K}_{ii}^{-1}\boldsymbol{K}_{ib} \\
\tilde{\boldsymbol{M}} &= \begin{bmatrix} \tilde{\boldsymbol{M}}_{bb} & \tilde{\boldsymbol{M}}_{b\zeta} \\ \tilde{\boldsymbol{M}}_{\zeta b} & \boldsymbol{I} \end{bmatrix} \\
\tilde{\boldsymbol{M}}_{bb} &= \boldsymbol{M}_{bb} - \boldsymbol{M}_{bi}\boldsymbol{K}_{ii}^{-1}\boldsymbol{K}_{ib} - \boldsymbol{K}_{bi}\boldsymbol{K}_{ii}^{-1}\boldsymbol{M}_{ib} + \boldsymbol{K}_{bi}\boldsymbol{K}_{ii}^{-1}\boldsymbol{M}_{ii}\boldsymbol{K}_{ii}^{-1}\boldsymbol{K}_{ib} \\
\tilde{\boldsymbol{M}}_{\zeta b} &= \boldsymbol{\Phi}_i^T\left(\boldsymbol{M}_{ib} - \boldsymbol{M}_{ii}\boldsymbol{K}_{ii}^{-1}\boldsymbol{K}_{ib}\right) = \tilde{\boldsymbol{M}}_{b\zeta}^T \\
\tilde{\boldsymbol{f}} &= \begin{bmatrix} \boldsymbol{f}_b + \boldsymbol{\Psi}_{C,i}^T\boldsymbol{f}_i \\ \boldsymbol{\Phi}_i^T\boldsymbol{f}_i \end{bmatrix}
\end{aligned}$$

The term $\boldsymbol{\Omega}_i^2$ is a diagonal matrix, containing the eigenfrequencies of the fixed interface vibration modes.

3.6 Modal Truncation Augmentation

As described in section 3.5, in the Craig-Bampton method the assumption is made that no external loading acts on the internal DoF $\boldsymbol{u}_i$. When the model is subjected to external loading on the internal DoF, this might lead to an inaccurate calculation of the response. The accuracy of the response of the internal DoF depends on the how well the reduction basis is able to describe the response to the external loading. Generally speaking, the approximation is accurate when the modes that are not included in the reduction basis, are not excited by the external loading. The two key parameters of interest here are *spectral* and *spatial convergence*. The difference between the two and their importance in model reduction is discussed in section 3.6.1. A way to increase spatial convergence is by adding Modal Truncation Augmentation vectors (MTAs) to the reduction basis. The derivation of the MTAs is introduced in section 3.6.2.

3.6.1 Spectral and spatial convergence

Spectral and spatial convergence are both important in the generation of an accurate reduced model. The two parameters can be described as follows:

- **Spectral convergence**: The accuracy of the response prediction depends on how well the frequency content of the reduction basis and the external force match. When the structure is excited by a spectrum of external loading, e.g. a wave spectrum, a rule of thumb states that all substructure's modes up to 1.5

times the highest loading frequency should be retained in the reduction basis [43]. However, only a high level of spectral convergence does not guarantee an accurate forced response.

- **Spatial convergence**: A second factor in the forced response accuracy is the spatial convergence. This parameter indicates how well the shape of the included modes is able to represent the spatial distribution of the external loading. A way to improve spatial convergence is to include more modes, but the extra modes are expensive to compute and lead to a larger and less efficient reduction basis. Furthermore, the convergence rate still depends on the correlation between the extra modes and the spatial load vectors.

The difference between the two types of convergence is best illustrated with an example. Figure 3.5a shows the cantilever beam subjected to a vertical force f_v, exciting the structure at a frequency ω that lies between the frequencies ω_1 and ω_2, corresponding to the first two fixed interface vibration modes.

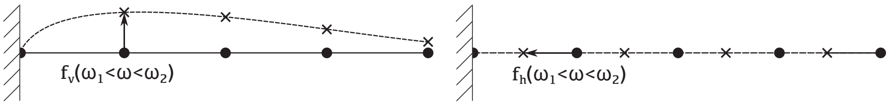

(a) Vertical force on internal DoF. **(b)** Horizontal force on internal DoF.

Figure 3.5: Maximum force and moment error for the different interpolation methods.

One can imagine that the response shape of the structure can be approximated by a combination of the second static constraint mode (figure 3.3b) and the first two fixed interface vibration modes (figure 3.4). The fact that the shapes in the reduction basis can represent the deformation shape, means that the reduced model has good spatial convergence for this specific loading. Furthermore, since the loading frequency of $\boldsymbol{f}_v$ lies between the frequencies corresponding to the included modes (ω_1 and ω_2), the reduced model also ensures good spectral convergence. In short, spatial convergence is related to the *shape* of the response, spectral convergence to its *frequency*.

This becomes more clear when the same point force is applied horizontally in terms of $\boldsymbol{f}_h$ in figure 3.5b. The spectral convergence is equally well represented as for the vertically loaded beam, however the deformation shape of the structure, in which only the left most element deforms axially, can not be represented by the fixed interface vibration shapes at all. The static constraint mode in figure 3.3b is able to describe the deformation of the first element to a certain degree but since that shape also deforms the other three elements, this reduced model will have a low accuracy due to lack of spatial convergence. This example clearly illustrates the difference between the two types of convergence and the importance to capture both in the reduced structural model.

One way to overcome the lack of spatial convergence is to add more fixed interface vibration modes. The problem with this approach is that it can be time consuming to find out which of these modes accurately describe the deformation induced by the external force. In the current example, the eigenmode capturing the axial deformation of the first element of the beam is often one of the modes corresponding to the higher eigenfrequecies. Since the reduction basis is normally filled with mode shapes corresponding to frequencies ranging from low to high, many shapes would have to be added in order to include the axial deformation shape. If one would add all fixed interface vibration modes, which are mass- and stiffness-orthogonal with respect to each other, the model converges to the exact solution. However, this defeats the purpose of the model reduction as in fact no reduction is realized.

Instead of adding extra structural modes to increase spatial convergence, another method was developed to find a set of dedicated, load dependent vectors. This method is known as Modal Truncation Augmentation (MTA) and has demonstrated significant accuracy improvement in the forced dynamic response [9], [31]. The modes that are computed based on the MTA method are called *psuedo modes* and are able to capture the spatial part of the forced response that the other types of modes in the reduction basis can be unable to describe accurately.

3.6.2 Derivation MTAs

For the derivation of the MTA vectors, a simple system is considered which is constrained such that no rigid body modes exist. The equations of motion are given by:

$$\boldsymbol{M}\ddot{\boldsymbol{u}} + \boldsymbol{K}\boldsymbol{u} = \boldsymbol{f} \tag{3.29}$$

Again, the response $\boldsymbol{u}$ is split in a static and a dynamic part:

$$\boldsymbol{u} = \boldsymbol{u}_{stat} + \boldsymbol{u}_{dyn} \tag{3.30}$$

As in the derivation of the static constraint modes, the static response is found by setting the accelerations to zero:

$$\boldsymbol{u}_{stat} = \boldsymbol{K}^{-1}\boldsymbol{f} \tag{3.31}$$

Inserting equation 3.30 and 3.31 into 3.29, the dynamic part of the response is given by:

$$\boldsymbol{M}\ddot{\boldsymbol{u}}_{dyn} + \boldsymbol{K}\boldsymbol{u}_{dyn} = -\boldsymbol{M}\boldsymbol{K}^{-1}\ddot{\boldsymbol{f}} \tag{3.32}$$

The same procedure can now be repeated for equation 3.32, where the response $\boldsymbol{u}_{dyn}$ is again subdivided into a quasi-static and a dynamic part, relative to the quasi-static part:

$$\boldsymbol{u}_{dyn} = \boldsymbol{y}_{stat} + \boldsymbol{y}_{dyn} \tag{3.33}$$

Consequently, the accelerations $\ddot{\boldsymbol{u}}_{dyn}$ are set to zero to find the quasi-static response $\boldsymbol{y}_{stat}$:

$$\boldsymbol{y}_{stat} = \boldsymbol{K}^{-1}\left(-\boldsymbol{M}\boldsymbol{K}^{-1}\right)\ddot{\boldsymbol{f}} \tag{3.34}$$

When equation 3.33 and 3.34 are substituted into 3.32, the dynamic part $\boldsymbol{y}_{dyn}$ is given by:

$$\boldsymbol{M}\ddot{\boldsymbol{y}}_{dyn} + \boldsymbol{K}\boldsymbol{y}_{dyn} = \left(-\boldsymbol{M}\boldsymbol{K}^{-1}\right)^2 \frac{d^4\boldsymbol{f}}{dt^4} \tag{3.35}$$

This procedure of representing the dynamic response by a quasi-static and dynamic response relative to that, can be repeated many times. This yields the following equation:

$$\begin{aligned} \boldsymbol{u} &= \boldsymbol{u}_{stat} + \boldsymbol{u}_{dyn} \\ &= \boldsymbol{u}_{stat} + \boldsymbol{y}_{stat} + \boldsymbol{y}_{dyn} \\ &= \boldsymbol{u}_{stat} + \boldsymbol{y}_{stat} + \boldsymbol{z}_{stat} + \ldots + \boldsymbol{w}_{dyn} \end{aligned} \tag{3.36}$$

Substituting the quasi-static solution into equation 3.36, the total response can be written as follows:

$$\boldsymbol{u} = \sum_{j=0}^{m} \boldsymbol{K}^{-1}\left(-\boldsymbol{M}\boldsymbol{K}^{-1}\right)^j \frac{d^{2j}\boldsymbol{f}}{dt^{2j}} + \boldsymbol{w}_{dyn} \tag{3.37}$$

Equation 3.37 represents the response of the system as a superposition of quasi-static solutions up to the order m. The dynamic solution is approximated by the truncated number of k retained vibration modes $\boldsymbol{\Phi}_k$. In order to be able to use equation 3.37, the external force $\boldsymbol{f}(t)$ has to be decomposed into a spatial and a spectral (time-dependent) part:

$$\boldsymbol{f}(t) = \sum_{p=1}^{g} \boldsymbol{f}_p \alpha_p(t) = \boldsymbol{F}\boldsymbol{\alpha}(t) \tag{3.38}$$

Where $\boldsymbol{f}_p$ is the p^{th} spatial vector and α_p represents the corresponding time-dependent amplitude. A limited number g of such spatial vectors are collected in $\boldsymbol{F}$ and are assumed to be able to represent the external loading. How these vectors can be obtained using the Proper Orthogonal Decomposition (POD) technique is explained in appendix E. The time-dependent variable $\boldsymbol{\alpha}(t)$ is discarded since only the spatial vectors are required to enhance the spatial convergence of the reduction basis. Substituting the force distribution vector (equation 3.38) into the first term on the right hand side of equation 3.37, the modal truncation augmentation vectors can be written as:

$$\tilde{\boldsymbol{\Phi}}_{M,j} = \boldsymbol{K}^{-1}\left(-\boldsymbol{M}\boldsymbol{K}^{-1}\right)^{j}\boldsymbol{F} \tag{3.39}$$

The columns in the $\tilde{\boldsymbol{\Phi}}_{M,j}$ matrix represent the MTA vectors (in short MTAs) of the order j; the number of vectors depends on the spatial force vectors p used in $\boldsymbol{F}$. Physically, the first order MTAs ($j = 0$) represent the structure's static response to the external loading in $\boldsymbol{F}$. For the second order vectors ($j = 1$), the static displacements due to these forces are first converted to inertia forces (times $\boldsymbol{M}$) and then converted to quasi-static displacements (times $\boldsymbol{K}^{-1}$) as a result of these inertia forces. In short, the MTAs provide a load-dependent quasi-static correction to the solution.

Both the MTA vectors $\tilde{\boldsymbol{\Phi}}_{M,j}$ and the vibration modes $\boldsymbol{\Phi}_r$ are included in the reduction basis. It is possible that there might be some "information overlap", i.e. the modes partly span the same space. This would result in a non-sparse matrix and could even lead to linearly dependent reduction matrix, introducing numerical stability issues. This problem can be avoided by subtracting the contribution of the vibration modes from the MTAs:

$$\begin{aligned}\tilde{\boldsymbol{\Phi}}_{M,j} &= \left(\boldsymbol{K}^{-1} - \boldsymbol{\Phi}_k\boldsymbol{\Omega}_k^{-2}\boldsymbol{\Phi}_k^T\right)\left(\boldsymbol{M}\boldsymbol{K}^{-1}\right)^{j}\boldsymbol{F}\\ &= \left(\boldsymbol{I} - \boldsymbol{\Phi}_k\boldsymbol{\Phi}_k^T\boldsymbol{M}\right)\left(\boldsymbol{K}^{-1}\boldsymbol{M}\right)^{j}\boldsymbol{K}^{-1}\boldsymbol{F}\\ &= \boldsymbol{P}\left(\boldsymbol{K}^{-1}\boldsymbol{M}\right)^{j}\boldsymbol{K}^{-1}\boldsymbol{F}\end{aligned} \tag{3.40}$$

Where the projection matrix $\boldsymbol{P} = \boldsymbol{I} - \boldsymbol{\Phi}_r\boldsymbol{\Phi}_r^T\boldsymbol{M}$, is used to orthogonalize the MTAs with respect to the vibration modes. The different orders of the MTAs can now be collected as follows:

$$\tilde{\boldsymbol{\Phi}}_{M} = \left[\tilde{\boldsymbol{\Phi}}_{M,1}\ldots\tilde{\boldsymbol{\Phi}}_{M,j}\ldots\tilde{\boldsymbol{\Phi}}_{M,k}\right] \tag{3.41}$$

In this equation k represents the highest order of the MTAs. Due to the previously described orthogonalisation, the MTAs are orthogonal with respect to the vibration modes, but not necessarily mutually orthogonal. To again avoid non-sparsity and numerical issues, the MTAs can be orthonormalized by solving the reduced eigenvalue problem in the space of the MTAs, also known as the *interaction problem*:

$$\left(\tilde{\boldsymbol{\Phi}}_M^T \boldsymbol{K} \tilde{\boldsymbol{\Phi}}_M\right) \boldsymbol{y} = \boldsymbol{\sigma}^2 \left(\tilde{\boldsymbol{\Phi}}_M^T \boldsymbol{M} \tilde{\boldsymbol{\Phi}}_M\right) \boldsymbol{y} \tag{3.42}$$

Where $\boldsymbol{\sigma}^2$ is a diagonal matrix that contains the pseudo-frequencies belonging to the MTAs. The eigenvectors are contained in $\boldsymbol{y}$ and the matrix $\tilde{\boldsymbol{\Phi}}_M$ contains all the non-orthonomalized MTAs. The orthonomalized MTAs are then found using:

$$\boldsymbol{\Phi}_M = \tilde{\boldsymbol{\Phi}}_M \boldsymbol{y} \tag{3.43}$$

Finally, the MTAs can be mass normalized using the following relations:

$$\begin{aligned} \boldsymbol{\Phi}_M^T \boldsymbol{M} \boldsymbol{\Phi}_M &= \boldsymbol{I} \\ \boldsymbol{\Phi}_M^T \boldsymbol{K} \boldsymbol{\Phi}_M &= \boldsymbol{\sigma}^2 \end{aligned} \tag{3.44}$$

The reason why MTAs are often referred to as psuedo-modes is because they do possess the orthogonality properties of the vibration modes but are not fundamental properties of the system, i.e. they are not solutions to the system's eigenvalue problem. Furthermore, it is noted that the pseudo-frequencies contained in $\boldsymbol{\sigma}^2$ are always higher than those of the vibration modes $\boldsymbol{\Omega}_k^2$. This is logical because the MTAs take into account the relevant contributions of the discarded vibration modes.

3.7 Augmenting the Craig-Bampton method

In this section the general MTA procedure as explained in section 3.6, is applied to augment the Craig-Bampton method. The starting point of the derivation is again the second line of the equations of motion (3.17). Separating the internal and boundary DoF gives:

$$\boldsymbol{M}_{ii}\ddot{\boldsymbol{u}}_i + \boldsymbol{K}_{ii}\boldsymbol{u}_i = -\boldsymbol{M}_{ib}\ddot{\boldsymbol{u}}_b - \boldsymbol{K}_{ib}\boldsymbol{u}_b + \boldsymbol{f}_i \tag{3.45}$$

As for the general MTA procedure, the response of the internal DoF is split into a static and a dynamic part:

$$\boldsymbol{u}_i = \boldsymbol{u}_{i,stat} + \boldsymbol{u}_{i,dyn} \tag{3.46}$$

The static response is found by substituting equation 3.46 into 3.45 and neglecting the intertia forces:

$$\boldsymbol{u}_{i,stat} = \boldsymbol{K}_{ii}^{-1}\boldsymbol{f}_i - \boldsymbol{K}_{ii}^{-1}\boldsymbol{K}_{ib}\boldsymbol{u}_b = \boldsymbol{K}_{ii}^{-1}\boldsymbol{f}_i + \boldsymbol{\Psi}_{C,i}\boldsymbol{u}_b \tag{3.47}$$

The first term on the right hand side is neglected in the classic derivation of the Craig-Bampton method, i.e. no external load on the internal DoF. In this augmented version of the Craig-Bampton method, the excitation force is specifically taken into account by the MTA vectors in order to improve the spatial convergence of the reduced model. The second term represents the static constraint modes, as derived in section 3.5.1. Inserting equation 3.46 and 3.47 into equation 3.45 yields the following expression for the dynamic response $\boldsymbol{u}_{i,dyn}$:

$$\boldsymbol{M}_{ii}\ddot{\boldsymbol{u}}_{i,dyn} + \boldsymbol{K}_{ii}\boldsymbol{u}_{i,dyn} = -\left(\boldsymbol{M}_{ii}\boldsymbol{\Psi}_{C,i} + \boldsymbol{M}_{ib}\right)\ddot{\boldsymbol{u}}_b - \boldsymbol{M}_{ii}\boldsymbol{K}_{ii}^{-1}\ddot{\boldsymbol{f}}_i \tag{3.48}$$

The columns of the term between brackets on the right hand side of equation 3.48 represent the load vectors, associated to the interface accelerations. The equation is rewritten as follows:

$$\boldsymbol{M}_{ii}\ddot{\boldsymbol{u}}_{i,dyn} + \boldsymbol{K}\boldsymbol{u}_{i,dyn} = \boldsymbol{Y}\ddot{\boldsymbol{u}}_b - \boldsymbol{M}_i i\boldsymbol{K}_{ii}^{-1}\ddot{\boldsymbol{f}}_i \tag{3.49}$$

Where $\boldsymbol{Y} = \left(-\boldsymbol{M}_{ii}\boldsymbol{\Psi}_{C,i} - \boldsymbol{M}_{ib}\right)$ is introduced for a more compact notation. The next step is to split $\boldsymbol{u}_{i,dyn}$ into a quasi-static part $\boldsymbol{y}_{i,stat}$ and a dynamic part $\boldsymbol{y}_{i,dyn}$ relative to that. The expression for the quasi-static part is again obtained by setting $\ddot{\boldsymbol{u}}_{i,dyn} = 0$:

$$\boldsymbol{y}_{i,stat} = \boldsymbol{K}_{ii}^{-1}\boldsymbol{Y}\ddot{\boldsymbol{u}}_b - \boldsymbol{K}_{ii}^{-1}\boldsymbol{M}_i i\boldsymbol{K}_{ii}^{-1}\ddot{\boldsymbol{f}}_i \tag{3.50}$$

The expression for $\boldsymbol{y}_{i,stat}$ is inserted into the definition of $\boldsymbol{u}_{i,dyn}$, which is consequently substituted into equation 3.49. Isolating the terms for the dynamic solution $\boldsymbol{y}_{i,dyn}$ on the left hand side gives:

$$\boldsymbol{M}_{ii}\ddot{\boldsymbol{y}}_{i,dyn} + \boldsymbol{K}\boldsymbol{y}_{i,dyn} = \boldsymbol{K}_{ii}^{-1}\boldsymbol{M}_{ii}\boldsymbol{K}_{ii}^{-1}\boldsymbol{Y}\frac{d^4\boldsymbol{u}_b}{dt^4} + \left(\boldsymbol{M}_{ii}\boldsymbol{K}_{ii}^{-1}\right)^2\frac{d^4\boldsymbol{f}_i}{dt^4} \tag{3.51}$$

Repetition of this process yields a similar sequence as was found in equation 3.36, however the response here is for the internal DoF $\boldsymbol{u}_i$. Substituting the obtained expression yields:

$$\begin{aligned}\boldsymbol{u}_i =& \boldsymbol{\Psi}_{C,i}\boldsymbol{u}_b - \boldsymbol{K}_{ii}^{-1}\boldsymbol{Y}\ddot{\boldsymbol{u}}_b - \boldsymbol{K}_{ii}^{-1}\boldsymbol{M}_{ii}\boldsymbol{K}_{ii}^{-1}\boldsymbol{Y}\frac{d^4\boldsymbol{u}_b}{dt^4} + \dots \\ &+ \boldsymbol{K}_{ii}^{-1}\boldsymbol{f}_i - \boldsymbol{K}_{ii}^{-1}\boldsymbol{M}_{ii}\boldsymbol{K}_{ii}^{-1}\ddot{\boldsymbol{f}}_i + \left(\boldsymbol{K}_{ii}^{-1}\boldsymbol{M}_{ii}\right)^2\boldsymbol{K}_{ii}^{-1}\frac{d^4\boldsymbol{f}_i}{dt^4} + \dots \\ &+ \boldsymbol{w}_{i,dyn}\end{aligned} \tag{3.52}$$

The first term on the right hand side of equation 3.52 represents the static constraint modes, which are normally already present in the Craig-Bampton reduction basis. An approximation of the last term, the dynamic solution, is present in the Craig-Bampton reduction basis through a superposition of fixed interface vibration modes $\boldsymbol{\Phi}_i$. The remaining terms can be separated into two groups; one group containing the terms with the external force on the internal DoF and an other group containing the interface excitation terms.

Similar to the procedure explained in section 3.6, it is assumed that the external loading $\boldsymbol{f}_i$ can be described by a superposition of k spatial vectors, contained in the matrix $\boldsymbol{F}_{(k)}$. The time-dependent term of the external loading is again disregarded. In order to assure that the MTAs are orthogonal with respect to the fixed-interface vibration modes, a similar projection step is carried out. Here the projection matrix is defined as $\boldsymbol{P} = \boldsymbol{I} - \boldsymbol{\Phi}_i \boldsymbol{\Phi}_i^T \boldsymbol{M}_{ii}$. The MTA vectors can now be calculated according to:

$$\tilde{\boldsymbol{\Phi}}_{MTA,j} = \boldsymbol{P}\left(\boldsymbol{K}_{ii}^{-1}\boldsymbol{M}_{ii}\right)^{j}\boldsymbol{K}_{ii}^{-1}\left[\boldsymbol{Y}\ \boldsymbol{F}_{(k)}\right] \quad j = 0, \dots, m \tag{3.53}$$

The number of MTAs per order now equals the number of interface DoF plus the number of load vectors. The vectors are orthonormalized with respect to $\boldsymbol{M}_{ii}$ and $\boldsymbol{K}_{ii}$ by solving a similar interaction problem to equation 3.42. The same properties as described in equation 3.44 are finally obtained using mass normalisation. The difference is that the properties here are valid for the mass and stiffness matrix of the internal DoF, $\boldsymbol{M}_{ii}$ and $\boldsymbol{K}_{ii}$. The solution of the internal DoF $\boldsymbol{u}_i$ can now be represented including the MTA vectors:

$$\boldsymbol{u}_i \approx \boldsymbol{\Psi}_{C,i}\boldsymbol{u}_b + \boldsymbol{\Phi}_i\boldsymbol{\eta}_i + \boldsymbol{\Phi}_{MTA}\boldsymbol{\zeta}_i \tag{3.54}$$

Where the vector $\boldsymbol{\zeta}_i$ contains the modal amplitudes of the MTAs. The augmented Craig-Bampton reduction basis is now given by:

$$\begin{bmatrix} \boldsymbol{u}_b \\ \boldsymbol{u}_i \end{bmatrix} \approx \begin{bmatrix} \boldsymbol{I} & \boldsymbol{0} & \boldsymbol{0} \\ \boldsymbol{\Psi}_{C,i} & \boldsymbol{\Phi} & \boldsymbol{\Phi}_{MTA} \end{bmatrix} \begin{bmatrix} \boldsymbol{u}_b \\ \boldsymbol{\eta}_i \\ \boldsymbol{\zeta}_i \end{bmatrix} = \boldsymbol{R}_{ACB}\boldsymbol{q}_{ACB} \tag{3.55}$$

Similar to the original Craig-Bampton method, all interface DoF are retained. The reduced mass and stiffness matrix are obtained by projecting their equivalent full matrices onto the reduction basis:

$$\begin{aligned} \tilde{\boldsymbol{M}} &= \boldsymbol{R}_{ACB}^T \boldsymbol{M} \boldsymbol{R}_{ACB} \\ \tilde{\boldsymbol{K}} &= \boldsymbol{R}_{ACB}^T \boldsymbol{K} \boldsymbol{R}_{ACB} \end{aligned} \tag{3.56}$$

Using these expressions, the reduced equations of motion can be written as:

$$\begin{bmatrix} \tilde{\boldsymbol{M}}_{bb} & \tilde{\boldsymbol{M}}_{b\zeta} & \tilde{\boldsymbol{M}}_{b\phi} \\ \tilde{\boldsymbol{M}}_{\zeta b} & \boldsymbol{I} & \boldsymbol{0} \\ \tilde{\boldsymbol{M}}_{\phi b} & \boldsymbol{0} & \boldsymbol{I} \end{bmatrix} \begin{bmatrix} \ddot{\boldsymbol{u}}_b \\ \ddot{\boldsymbol{\eta}}_i \\ \ddot{\boldsymbol{\zeta}}_i \end{bmatrix} \begin{bmatrix} \tilde{\boldsymbol{K}}_{bb} & \boldsymbol{0} & \boldsymbol{0} \\ \boldsymbol{0} & \boldsymbol{\Omega}_i^2 & \boldsymbol{0} \\ \boldsymbol{0} & \boldsymbol{0} & \boldsymbol{\sigma}^2 \end{bmatrix} \begin{bmatrix} \boldsymbol{u}_b \\ \boldsymbol{\eta}_i \\ \boldsymbol{\zeta}_i \end{bmatrix} = \begin{bmatrix} \tilde{\boldsymbol{f}}_i \\ \tilde{\boldsymbol{f}}_M \\ \tilde{\boldsymbol{f}}_b \end{bmatrix} + \begin{bmatrix} \boldsymbol{0} \\ \boldsymbol{0} \\ \boldsymbol{g}_b \end{bmatrix} \tag{3.57}$$

In addition to terms already defined in equation 3.5.2, the terms in the reduced matrices are defined as:

$$\tilde{\boldsymbol{M}}_{\zeta b} = \tilde{\boldsymbol{M}}_{b\zeta}^T = \boldsymbol{\Phi}_i^T\left(\boldsymbol{M}_{ib} - \boldsymbol{M}_{ii}\boldsymbol{K}_{ii}^{-1}\boldsymbol{K}_{ib}\right) \tag{3.58}$$

4

Modeling and case study

4.1 Introduction

Based on the theoretical background provided in chapters 2 and 3, the implementation of both the wave and the structural model is described in this chapter. Furthermore, the setup for the case study is discussed on which the results presented in the following two chapters are based. The current chapter starts with section 4.2, describing the implementation and verification of the wave model. Section 4.3 explains how the full structural model is build up and which type of reduced models are used in the case study. Section 4.4 elaborates on the details of the case study in which a full load case table is used to calculate the fatigue loading in the jacket foundation, using wave-only loading.

Figure 4.1 provides a flowchart of the implementation of the combined wave and structural model. During the preprocessing all member properties are collected and the wave spectrum is generated based on the sea state inputs. Next, the wave kinematics are calculated using the Inverse Fast Fourier Transform (IFFT) method. If a member is located in the splash zone the kinematics are adjusted using the moving coordinate. Subsequently, the wave kinematics are converted to nodal forces by means of the Morison equation and the shape functions of the members. Again, a distinction is made between fully submerged members and members in the splash zone. This is done to increase computational efficiency. The blocks containing the wave kinematics and wave force procedures are colored to indicate that these steps are repeated for each of jacket members. Finally, the dynamic simulation is performed, either using a full or a reduced foundation model. In case the reduced model requires MTAs, the complete force field is subjected to the POD method to extract the dominant mode shapes. The response is obtained using the Newmark time integration method. All theses steps are discussed throughout this chapter.

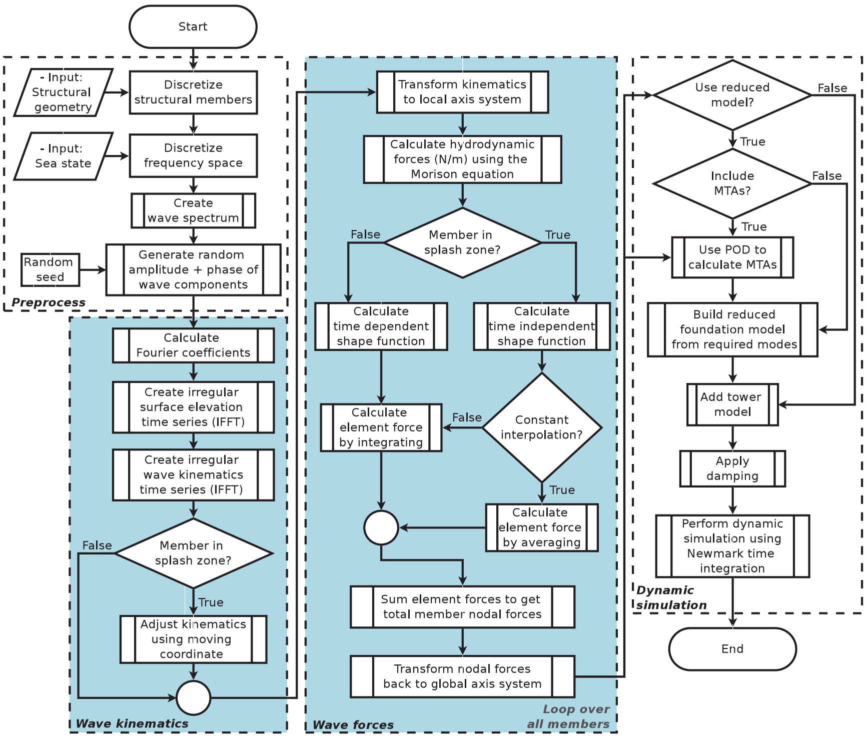

Figure 4.1: Flowchart of the combined wave and structural model.

4.2 Wave model

This section aims to explain both the implementation and the verification of the wave model. The wave model is an extension of the work of Van der Meulen [41] and is a unidirectional implementation of Sharma and Dean's formulation of the second-order pertubation model [36]. Section 4.2.1 starts with the formulation of the irregular wave model, providing the linear and second-order equations. The IFFT method is used in order to significantly increase the computational efficiency of the wave model. The basic principles and application in the wave model are explained in section 4.2.2. Consequently, the Morison equation is used to translate wave kinematics into wave forces. Details regarding this approach and the influence of the type of force distribution are discussed in section 4.2.3. Finally, the wave model is compared to the software USFOS in section 4.2.4 for a verification in terms of the resultant wave forces.

4.2.1 Irregular wave model

As described in section 2.7, the velocity potential can presented as the sum of the linear part and the second-order pertubation:

$$\Phi(x,z,t) = \Phi^{(1)}(x,z,t) + \Phi^{(2)}(x,z,t) \tag{4.1}$$

Similarly, the total surface elevation is given by:

$$\eta(x,t) = \eta^{(1)}(x,t) + \eta^{(2)}(x,t) \tag{4.2}$$

The following two sections describe the first- and second-order expressions for the second-order pertubation model.

First order expressions
The first-order velocity potential is given by:

$$\Phi^{(1)}(x,z,t) = -\sum_{m=1}^{N} b_m \frac{\cosh k_m(z+d)}{\cosh k_m d} \sin(\psi_m) \tag{4.3}$$

Where the amplitude and the phase functions are given by equation 4.4 and 4.5, respectively:

$$b_m = \frac{a_m g}{\omega_m} \tag{4.4}$$

$$\psi_m = \omega_m t - k_m x - \phi_m \tag{4.5}$$

In equation 4.3 it should be noticed that it has been multiplied with -1, compared to equation 2.6 ($\sin(x) = -\sin(-x)$). This is done in order to provide a more transparent reformulation in section 4.2.2 on the Inverse Fast Fourier Transform. The first-order surface elevation is given by:

$$\eta^{(1)}(x,t) = \sum_{m=1}^{N} a_m \cos(\psi_m) \tag{4.6}$$

The phase angles ϕ_m are uniformly distributed between 0 and 2π, the amplitudes a_m are Rayleigh distributed and are drawn from the wave spectrum $S(f_m)$:

$$a_m = \sqrt{2S(f_m)\Delta f} \tag{4.7}$$

Note that the wave spectrum is given in Hz, rather than in angular frequency. The transformation is done easily through $\Delta f_m = \Delta\omega_m/(2\pi)$. The first-order horizontal and vertical velocity u and w are obtained by taking the spatial derivative of the velocity potential:

$$u^{(1)}(x,z,t) = \frac{\partial \Phi^{(1)}}{\partial x} = \sum_{m=1}^{N} k_m b_m \frac{\cosh k_m(z+d)}{\cosh k_m d} \cos(\psi_m) \tag{4.8}$$

$$w^{(1)}(x,z,t) = \frac{\partial \Phi^{(1)}}{\partial z} = -\sum_{m=1}^{N} k_m b_m \frac{\sinh k_m(z+d)}{\cosh k_m d} \sin(\psi_m) \tag{4.9}$$

The first-order accelerations are then obtained by taking the time derivative of the two velocity terms, respectively:

$$\dot{u}^{(1)}(x,z,t) = \frac{\partial u^{(1)}}{\partial t} = -\sum_{m=1}^{N} \omega_m k_m b_m \frac{\cosh k_m(z+d)}{\cosh k_m d} \sin(\psi_m) \tag{4.10}$$

$$\dot{w}^{(1)}(x,z,t) = \frac{\partial w^{(1)}}{\partial t} = -\sum_{m=1}^{N} \omega_m k_m b_m \frac{\sinh k_m(z+d)}{\cosh k_m d} \cos(\psi_m) \tag{4.11}$$

Second-order expressions

The second-order contributions consist of two parts, i.e. the sum and difference components. The velocity potential is build up accordingly, $\Phi^{(2)} = \Phi^{(2-)} + \Phi^{(2+)}$ and is defined as follows:

$$\Phi^{(2)}(x,z,t) = -\frac{1}{4} \sum_{m=1}^{N} \sum_{n=1}^{N} \left[b_m b_n \frac{\cosh k_{mn}^{\pm}(z+d)}{\cosh k_{mn}^{\pm} d} \frac{D_{mn}^{\pm}}{(\omega_m \pm \omega_n)} \sin(\psi_m \pm \psi_n) \right] \tag{4.12}$$

Where

$$\begin{aligned} D_{mn}^{-} = & \frac{(\sqrt{R_m} - \sqrt{R_n})[\sqrt{R_n}(k_m^2 - R_m^2) - \sqrt{R_m}(k_n^2 - R_n^2)]}{(\sqrt{R_m} - \sqrt{R_n})^2 - k_{mn}^{-} \tanh k_{mn}^{-} d} \\ & + 2 \frac{(\sqrt{R_m} - \sqrt{R_n})^2 (k_m k_n + R_m R_n)}{(\sqrt{R_m} - \sqrt{R_n})^2 - k_{mn}^{-} \tanh k_{mn}^{-} d} \end{aligned} \tag{4.13}$$

$$\begin{aligned} D_{mn}^{+} = & \frac{(\sqrt{R_m} + \sqrt{R_n})[\sqrt{R_n}(k_m^2 - R_m^2) + \sqrt{R_m}(k_n^2 - R_n^2)]}{(\sqrt{R_m} + \sqrt{R_n})^2 - k_{mn}^{+} \tanh k_{mn}^{+} d} \\ & + 2 \frac{(\sqrt{R_m} + \sqrt{R_n})^2 (k_m k_n - R_m R_n)}{(\sqrt{R_m} + \sqrt{R_n})^2 - k_{mn}^{+} \tanh k_{mn}^{+} d} \end{aligned} \tag{4.14}$$

The wave numbers k_{mn}^{-}, k_{mn}^{+} and the variables R_m, R_n are defined as:

$$k_{mn}^{-} = |k_m - k_n| \tag{4.15}$$

$$k_{mn}^{+} = k_m + k_n \tag{4.16}$$

$$R_m = \frac{\omega_m^2}{g} \tag{4.17}$$

The second-order surface elevation $\eta^{(2)}$ is given by:

$$\eta^{(2)}(x,t) = \sum_{m=1}^{N}\sum_{n=1}^{N}\left[a_m a_n \left(B_{mn}^{-}\cos(\psi_m - \psi_n) + B_{mn}^{+}\cos(\psi_m + \psi_n)\right)\right] \tag{4.18}$$

Where the transfer functions for the second-order amplitude are defined as:

$$B_{mn}^{\pm} = \frac{1}{4}\left[\frac{D_{mn}^{\pm} - (k_m k_n \pm R_m R_n)}{\sqrt{R_m R_n}} + (R_m + R_n)\right] \tag{4.19}$$

Finally, the second-order kinematics are derived in a similar manner as their linear counterparts. The horizontal and vertical velocity are given by:

$$u^{(2)}(x,z,t) = \frac{\partial \Phi^{(2)}}{\partial x} = \sum_{m=1}^{N}\sum_{n=1}^{N} Z_{mn}^{\pm}\cos(\psi_m \pm \psi_n) \tag{4.20}$$

$$w^{(2)}(x,z,t) = \frac{\partial \Phi^{(2)}}{\partial z} = -\sum_{m=1}^{N}\sum_{n=1}^{N} Q_{mn}^{\pm}\sin(\psi_m \pm \psi_n) \tag{4.21}$$

The accelerations are again found by taking the time derivative of the velocities:

$$\dot{u}^{(2)}(x,z,t) = \frac{\partial u^{(2)}}{\partial t} = -\sum_{m=1}^{N}\sum_{n=1}^{N} Z_{mn}^{\pm}(\omega_m \pm \omega_n)\sin(\psi_m \pm \psi_n) \tag{4.22}$$

$$\dot{w}^{(2)}(x,z,t) = \frac{\partial w^{(2)}}{\partial t} = -\sum_{m=1}^{N}\sum_{n=1}^{N} Q_{mn}^{\pm}(\omega_m \pm \omega_n)\cos(\psi_m \pm \psi_n) \tag{4.23}$$

Where the variables $Z_{mn}^{\pm}$ and $Q_{mn}^{\pm}$ are introduced to collect the amplitude terms:

$$Z_{mn}^{\pm} = \frac{1}{4} b_m b_n \frac{\cosh k_{mn}^{\pm}(z+d)}{\cosh k_{mn}^{\pm} d} \frac{D_{mn}^{\pm}}{(\omega_{R,m} \pm \omega_{R,n})} k_{mn}^{\pm} \tag{4.24}$$

$$Q_{mn}^{\pm} = \frac{1}{4} b_m b_n \frac{\sinh k_{mn}^{\pm}(z+d)}{\cosh k_{mn}^{\pm} d} \frac{D_{mn}^{\pm}}{(\omega_{R,m} \pm \omega_{R,n})} k_{mn}^{\pm} \tag{4.25}$$

4.2.2 Inverse Fast Fourier Transform

As described in section 2.8, the contributions of the individual regular waves can be superimposed in order to create a regular wave train. However, many frequency components are required to accurately describe the sea spectrum and the superposition method can therefore become a computationally expensive procedure. This is especially true for the second-order contributions where a double summation is involved. A more efficient approach is to use the *Inverse Fast Fourier Transform*. This is method is based on the Fourier Transform, which is a technique that allows a signal in the time-domain to be transformed into a spectrum in the frequency domain. Using the IFFT, the individual wave contributions are efficiently calculated in the frequency domain and consequently summed and transformed to the time-domain, generating the desired time-series for the irregular wave.

IFFT definition
An illustration of the use of the IFFT is provided in the following explanation, using the first-order surface elevation $\eta^{(1)}$ as an example. The required simulation time T needs to be discretized into N time steps of Δt. The size of the time step is directly related to the computational time and must therefore be chosen carefully. The time step must be sufficiently small in order to accurately capture the behavior of the waves with a period around the peak period of the spectrum. It is important to realize that the sum contribution of the second-order introduces another peak at twice the peak frequency of the spectrum. To discretize T, a time vector $t_p = p\Delta t$ is introduced, where $p = 1, 2, ..., N$. The angular frequency is discretized in the same way, introducing the frequency vector $\omega_m = m\Delta\omega$, where $m = 1, 2, ..., N$. Using these vectors, the first-order surface elevation can now be presented in a discretized format:

$$\eta^{(1)}(x, t_p) = \sum_{m=1}^{N} a_m \cos(\omega_m t_p - k_m x - \phi_m) \tag{4.26}$$

Equation 4.26 can be reformulated according to Euler's complex exponential function, $\exp(i\phi) = \cos(\phi) + i\sin(\phi)$:

$$\eta^{(1)}(x, t_p) = \Re\left\{\sum_{m=1}^{N} a_m \exp(-i(k_m x + \phi_m)) \exp(i(m\Delta\omega)(p\Delta t))\right\} \tag{4.27}$$

Where $\Re$ stands for the real part of the expression. The multiplication of the time and frequency bin width can be rewritten to $\Delta\omega\Delta t = 2\pi/N$, yielding:

$$\eta^{(1)}(x, t_p) = \Re\left\{\sum_{m=1}^{N} X_{\eta}^{(1)}(\omega_m) \exp\left(i\frac{2\pi m}{N}p\right)\right\} \tag{4.28}$$

From equation 4.27 to 4.28, the amplitude a_m and the first exponential term are gathered in the Fourier coefficient of the the first-order surface elevation, $X_\eta^{(1)}$:

$$X_\eta^{(1)}(x,\omega_m) = a_m \exp(-i(k_m x + \phi_m)) \tag{4.29}$$

It is observed that the Fourier coefficient is not time-dependent but rather a function of the frequency ω_m. Equation 4.30 describes the inverse of the Discrete Fourier Transform of $X_\eta^{(1)}$. Using the IFFT algorithm [4], this transform can be calculated in an efficient manner and the first-order surface elevation can thus be reformulated as:

$$\eta^{(1)}(x,t_p) = \Re\left\{\text{IFFT}\left[X_\eta^{(1)}(x,\omega_m)\right]\right\} \tag{4.30}$$

Fourier coefficient

Following the described definition, the Fourier coefficients for all first- and second-order wave variables can be derived. In this way, a complete formulation of the wave problem is established in the frequency domain. By means of a more short formulation, the dependency on x and ω_m is dropped from the notation, e.g. $X_{\eta,m}^{(1)}(x,\omega_m)$ is now simply written as $X_{\eta,m}^{(1)}$:

$$X_{\eta,m}^{(1)} = a_m \exp(-i(k_m x + \phi_m)) \tag{4.31}$$

Considering the first-order the horizontal and vertical velocity $u^{(1)}$ and $w^{(1)}$, the Fourier coefficients are defined according to equation 4.32 and 4.33, respectively:

$$X_{u,m}^{(1)} = \frac{gk_m}{\omega_m}\frac{\cosh k_m(z+d)}{\cosh k_m d}X_{\eta,m}^{(1)} \tag{4.32}$$

$$X_{w,m}^{(1)} = -\frac{gk_m}{\omega_m}\frac{\sinh k_m(z+d)}{\cosh k_m d}X_{\eta,m}^{(1)} \tag{4.33}$$

Consequently, the Fourier coefficients for the acceleration terms are given by:

$$X_{\dot{u},m}^{(1)} = -\omega_m X_{u,m}^{(1)} \tag{4.34}$$

$$X_{\dot{w},m}^{(1)} = \omega_m X_{w,m}^{(1)} \tag{4.35}$$

Applying the IFFT to the above defined Fourier coefficients, the first-order kinematics are found. $\Im$ refers to the imaginary part of the expression.

$$u^{(1)}(x,z,t_p) = \Re\left\{\text{IFFT}\left[X^{(1)}_{u,m}\right]\right\} \tag{4.36}$$

$$w^{(1)}(x,z,t_p) = \Im\left\{\text{IFFT}\left[X^{(1)}_{w,m}\right]\right\} \tag{4.37}$$

$$\dot{u}^{(1)}(x,z,t_p) = \Im\left\{\text{IFFT}\left[X^{(1)}_{\dot{u},m}\right]\right\} \tag{4.38}$$

$$\dot{w}^{(1)}(x,z,t_p) = \Re\left\{\text{IFFT}\left[X^{(1)}_{\dot{w},m}\right]\right\} \tag{4.39}$$

The second-order terms can be expressed by means of Fourier coefficients in a similar way. The Fourier coefficient of the second-order surface elevation is given by equation 4.40:

$$X^{(2)}_{\eta,nm} = a_m a_n B^{\pm}_{mn} \text{exp}\left(-i((k_m x \pm k_n x) + (\phi_m \pm \phi_n))\right) \tag{4.40}$$

The second-order surface elevation can then be discretized and reformulated to:

$$\eta^{(2)}(t_p) = \Re\left\{\sum_{m=1}^{N}\sum_{n=1}^{N} X^{(2)}_{\eta,mn} \exp\left(i\frac{2\pi(m \pm n)}{N}p\right)\right\} \tag{4.41}$$

In order to further increase computational efficiency, [1] describes a method which reduces the double summation in 4.41 into a single summation:

$$\eta^{(2)}(t_q) = \Re\left\{\sum_{m=1}^{M} Y^{(2)}_{\eta,j} \exp\left(i\frac{2\pi j}{M}q\right)\right\} \tag{4.42}$$

The introduction of equation 4.42 allows the second-order surface elevation to be calculated according to the newly defined Fourier coefficient $Y^{(2)}_{\eta,j}$:

$$\eta^{(2)}(t_q) = \Re\left\{\text{IFFT}\left[Y^{(2)}_{\eta,j}\right]\right\} \tag{4.43}$$

This formulation requires the definition of this single-summation Fourier coefficient $Y^{(2)}_{\eta,j}$. As can be seen from equation 4.43, a new time vector t_q is introduced. This is required in order to be able to represent the highest sum-frequencies. Hence, the index vector q is defined as $q = 1, 2, ..., M$ where $M = 2N$. The new time vector is then defined as $t_q = q\Delta t$. The single-summation method is based on the collection of the original Fourier coefficients $X^{(2)}_{\eta,mn}$ for every possible combination of index pairs of m and n, adding up to j. For example, the double-summation index pairs $(m, n) = (1, 3)$, $(3, 1)$ and $(2, 2)$, all contribute to the sum interactions of $j = 4$. The coefficients for the difference-contribution can be formulated in a similar way. Since the IFFT formulation of $\eta^{(2)}(t_q)$ (equation 4.43) requires positive values of j, the difference index vector is defined as $j = |m - n|$. The single summation coefficient

$Y_{\eta,j}^{(2-)}$ with $j = 1$ thus contains contributions from $X_{\eta,mn}^{(2)}$ with $(m,n) = (1,2)$ and $(2,1)$. Using the above described properties of the single-summation Fourier coefficients, the sum- and difference-coefficients are fully described by equation 4.44 and 4.45, respectively:

$$Y_{\eta,j}^{(2+)} = \begin{cases} 0 & j \leq 2, \\ \underbrace{\sum\sum}_{\text{m+n =j}} X_{\eta,mn}^{(2+)} & 2 \leq j \leq M. \end{cases} \tag{4.44}$$

$$Y_{\eta,j}^{(2-)} = \begin{cases} \underbrace{\sum\sum}_{\text{|m-n| =j}} X_{\eta,mn}^{(2-)} & 1 \leq j \leq (N-1), \\ 0 & j > (N-1). \end{cases} \tag{4.45}$$

The second-order surface elevation is now completely defined in terms of the single-summation Fourier coefficients. The second-order velocities and accelerations are first discretized using the same approach as for the surface elevation:

$$u^{(2)}(x,z,t_p) = \Re\left\{\sum_{m=1}^{N}\sum_{n=1}^{N} X_{u,mn}^{(2)} \exp\left(i\frac{2\pi(m\pm n)}{N}p\right)\right\} \tag{4.46}$$

$$w^{(2)}(x,z,t_p) = \Im\left\{\sum_{m=1}^{N}\sum_{n=1}^{N} X_{w,mn}^{(2)} \exp\left(i\frac{2\pi(m\pm n)}{N}p\right)\right\} \tag{4.47}$$

$$\dot{u}^{(2)}(x,z,t_p) = \Im\left\{\sum_{m=1}^{N}\sum_{n=1}^{N} X_{\dot{u},mn}^{(2)} \exp\left(i\frac{2\pi(m\pm n)}{N}p\right)\right\} \tag{4.48}$$

$$\dot{w}^{(2)}(x,z,t_p) = \Re\left\{\sum_{m=1}^{N}\sum_{n=1}^{N} X_{\dot{w},mn}^{(2)} \exp\left(i\frac{2\pi(m\pm n)}{N}p\right)\right\} \tag{4.49}$$

The double-summation Fourier coefficients for the second-order kinematics are provided in equation 4.50 to 4.53:

$$X_{u,mn}^{(2)} = \quad Z_{mn}^{\pm} \exp\left(-i(k_m x \pm k_n x) + (\phi_m \pm \phi_n)\right) \text{sgn}(m \pm n)) \tag{4.50}$$

$$X_{w,mn}^{(2)} = -Q_{mn}^{\pm} \exp\left(-i(k_m x \pm k_n x) + (\phi_m \pm \phi_n)\right) \text{sgn}(m \pm n)) \tag{4.51}$$

$$X_{\dot{u},mn}^{(2)} = -(\omega_m \pm \omega_n) X_{u,mn}^{(2)} \tag{4.52}$$

$$X_{\dot{w},mn}^{(2)} = \quad (\omega_m \pm \omega_n) X_{w,mn}^{(2)} \tag{4.53}$$

The signum function sgn(x) in equation 4.50 is an odd function and is defined as:

$$\mathrm{sgn}(x) = \begin{cases} -1 & x < 0, \\ 0 & x = 0, \\ 1 & x > 0. \end{cases} \tag{4.54}$$

The procedure to reformulate the second-order surface elevation in terms of the single-summations Fourier coefficients can also be applied to the second-order kinematics. The IFFT of the obtained coefficients then yields the discretized second-order horizontal velocity and acceleration, as presented in equation 4.55 and 4.58, respectively, where the single summation Fourier coefficients are represented by the several $Y_j^{(2)}$ terms:

$$u^{(2)}(x,z,t_q) = \Re\left\{\mathrm{IFFT}\left[Y_{u,j}^{(2)}\right]\right\} \tag{4.55}$$

$$w^{(2)}(x,z,t_q) = \Im\left\{\mathrm{IFFT}\left[Y_{w,j}^{(2)}\right]\right\} \tag{4.56}$$

$$\dot{u}^{(2)}(x,z,t_q) = \Im\left\{\mathrm{IFFT}\left[Y_{\dot{u},j}^{(2)}\right]\right\} \tag{4.57}$$

$$\dot{w}^{(2)}(x,z,t_q) = \Re\left\{\mathrm{IFFT}\left[Y_{\dot{w},j}^{(2)}\right]\right\} \tag{4.58}$$

The formulation of the second-order kinematics completes the single-summation IFFT description of the wave problem. Using this implementation, the model is capable of a far more efficient computation compared to the time domain superposition, without loss of accuracy. Furthermore, the Taylor-expansion model as described in section 2.6, is used to stretch the kinematics to the free surface. This model is consistent up to the second order. This concludes the *wave kinematics* procedure as illustrated by the flowchart of the model in figure 4.1.

4.2.3 Wave forces

The kinematics model fully describes the first- and second-order wave motion. Next, the structural properties come into play when the hydrodynamic forces are calculated using the Morison equation. This section corresponds to the *wave forces* procedure depicted in the flowchart in figure 4.1. The theoretical background on the Morison equations is provided in section 2.9 but the equation itself is repeated here for convenience:

$$dF = \tfrac{1}{4}\rho C_M \pi D^2 \dot{u} dz + \tfrac{1}{2}\rho C_D D u|u| dz \tag{4.59}$$

As discussed, the kinematic terms u and $\dot{u}$ in equation 4.59 imply the velocity and acceleration normal to the structural element. As the kinematics model is applied in the global axis system, a rotation to the element local axis system is required to calculate the forces on each of the individual jacket members. This axis system is defined by two rotations: firstly with angle α around the z-axis and secondly with angle $-\beta$ around the new y'-axis. The definition of the local axis system is illustrated in figure 4.2 where the subscripts $_g$ and $_l$ indicate the global and local axis system, respectively. The different L terms represent the projected length of the structural element.

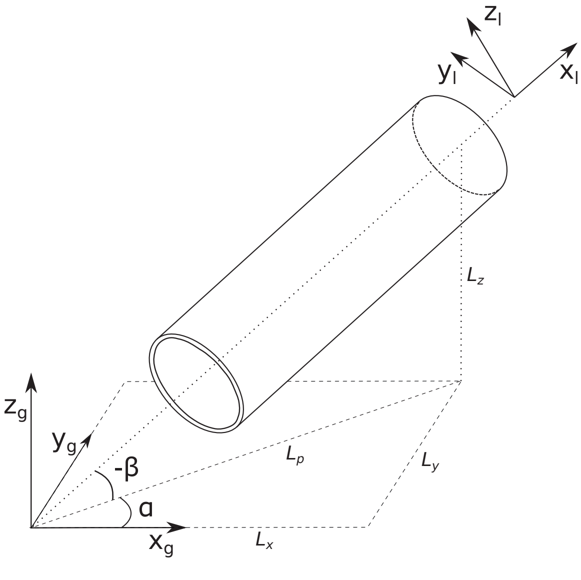

Figure 4.2: Definition of the local axis system.

The rotation matrix T is defined as follows:

$$\begin{aligned}\boldsymbol{T} &= \begin{bmatrix} \cos(-\beta) & 0 & -\sin(-\beta) \\ 0 & 1 & 0 \\ \sin(-\beta) & 0 & \cos(-\beta) \end{bmatrix} \begin{bmatrix} \cos(\alpha) & \sin(\alpha) & 0 \\ -\sin(\alpha) & \cos(\alpha) & 0 \\ 0 & 0 & 1 \end{bmatrix} \\ &= \begin{bmatrix} \cos(\alpha)\cos(\beta) & \sin(\alpha)\cos(\beta) & \sin(\beta) \\ -\sin(\alpha) & \cos(\alpha) & 0 \\ -\cos(\alpha)\sin(\beta) & -\sin(\alpha)\sin(\beta) & \cos(\beta) \end{bmatrix}\end{aligned} \tag{4.60}$$

Where α and β are defined as:

$$\alpha = \operatorname{atan}\left(\frac{L_y}{L_x}\right) \tag{4.61}$$

$$\beta = -\operatorname{atan}\left(\frac{L_z}{L_p}\right) \tag{4.62}$$

Hence, based on the start and end coordinates of a structural member, its orientation can be established and the global kinematics can be expressed in its local axis system:

$$\boldsymbol{V}_l = \begin{bmatrix} u_l \\ v_l \\ w_l \end{bmatrix} = \boldsymbol{T} \begin{bmatrix} u_g \\ v_g \\ w_g \end{bmatrix} \tag{4.63}$$

For a three dimensional member, the Morison equation can be written as:

$$F = \tfrac{1}{4}\rho C_M \pi D^2 \dot{\boldsymbol{V}}_l + \tfrac{1}{2}\rho C_D D V_n \boldsymbol{V}_l \tag{4.64}$$

Where V_n is the total normal velocity and is the resultant of the velocities along the local y- and z-axis, v_l and w_l respectively:

$$V_n = \sqrt{v_l^2 + w_l^2} \tag{4.65}$$

The Morison equation is used to calculate the hydrodynamic force in N/m at a number of points along the jacket member, defined by the hydrodynamic discretization. Eventually the forces (and moments) applied on the member need to be translated to nodal forces in the structural end nodes of the member. This is necessary because the hydrodynamic forces are applied to the structural nodes of the FE model in the dynamic simulation. Some steps have to be taken in order to get from the sectional forces in the "hydrodynamic nodes" to forces and moments in the structural nodes of the member. The sectional forces first need to be interpolated to obtain a distributed force $q(x)$ along the member. This distributed force is then multiplied with the shape functions of the structural element $N_i^e(x)$ which describe the translation into nodal forces and moments. Finally, this new function is integrated along the length of the member to obtain the nodal forces and moments, according to equation 4.66:

$$\boldsymbol{f} = \sum_{i=1}^{n} \int_{x_i}^{x_{i+1}} \boldsymbol{N}^{e^T}(x)\boldsymbol{q}(x)dx \tag{4.66}$$

An example of the use of the shape functions is given here by means of a 2D beam element. The beam element has four DoF, two translations and two rotations, and can be described by the following set of shape functions:

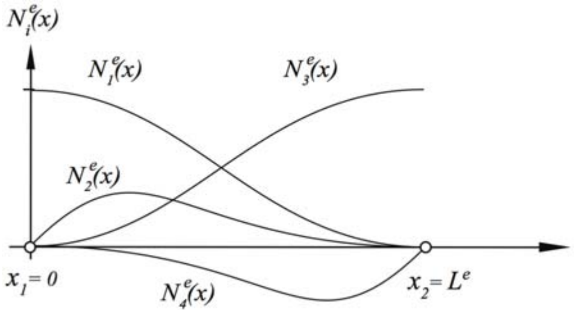

$$\begin{aligned}
N_1^e(x) &= 1 - \frac{3x^2}{L^{e^2}} + \frac{2x^3}{L^{e^3}} \\
N_2^e(x) &= x - \frac{2x^2}{L^{e^2}} + \frac{x^3}{L^{e^2}} \\
N_3^e(x) &= \frac{3x^2}{L^{e^2}} - \frac{2x^3}{L^{e^3}} \\
N_4^e(x) &= \frac{x^3}{L^{e^2}} - \frac{x^2}{L^{e}}
\end{aligned} \tag{4.67}$$

For the choice of interpolation function $q(x)$ the model offers three different options: quadratic, linear and constant. The three distributions are illustrated in figure 4.3.

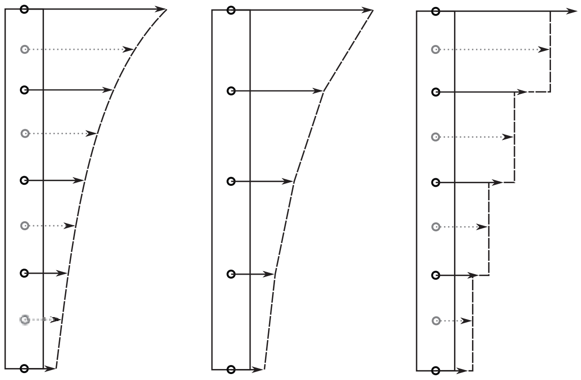

Figure 4.3: Quadratic, linear and constant interpolation of the sectional forces.

The most straightforward method is linear interpolation, where the kinematics and the sectional forces are calculated in the predefined hydrodynamic nodes. To be able to describe a quadratic distribution over an element, an additional center point is required. For the constant distribution, a point force is calculated in the center of each element, based on the average of the end forces of the element.

The choice of interpolation function has an influence on the accuracy and the calculation time of the simulation. Where the quadratic distribution yields the most accurate solution, the constant interpolation performs best in terms of calculation time. The latter is due to the fact that both the linear and the quadratic method require an integration over the discretization length while for the constant method a simple multiplication suffices. The difference in accuracy for the three interpolation methods is presented in figure 4.4. A distinction is made between a fully submerged member and a member in the splash zone. The considered member has a length of 10 m, which means for example that the hydrodynamic discretization length is 1 m when using 10 elements.

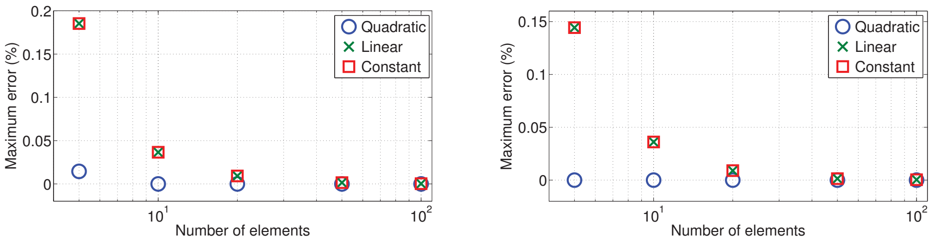

(a) Error force splash zone member

(b) Error force submerged member

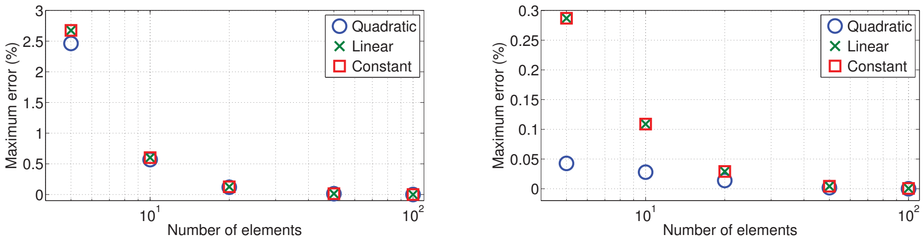

(c) Error moment splash zone member

(d) Error moment submerged member

Figure 4.4: Maximum force and moment error for the different interpolation methods.

It can be seen that, as expected, the quadratic function performs best in terms of accuracy. The linear and the constant functions provide the same level of accuracy. This is because integrating the linearly distributed force over the discretization length yields the same result as multiplying the average of the end forces with that same length. Furthermore, it is observed that maximum error is made for the moment in the splash zone. This is due to the fact that not only accuracy of the amplitude of the force but also that of the moment arm is dependent on the discretization length. The difference in terms of calculation time is illustrated in figure

4.5 for 6000 time steps (10 min simulation time with $\Delta t = 0.1$ s). It can be seen that the constant method requires the least amount of time, which especially true for the fully submerged member. As is illustrated in the flowchart of the model (figure 4.1), when a member is fully submerged, the shape function is time-independent and thus needs to be calculated only once. In combination with the simple multiplication operation of the constant method, this yields a very time-efficient procedure (figure 4.5b). Due to the fact that shape function is time-dependent in the splash zone, the difference between the three methods is less pronounced there (figure 4.5a).

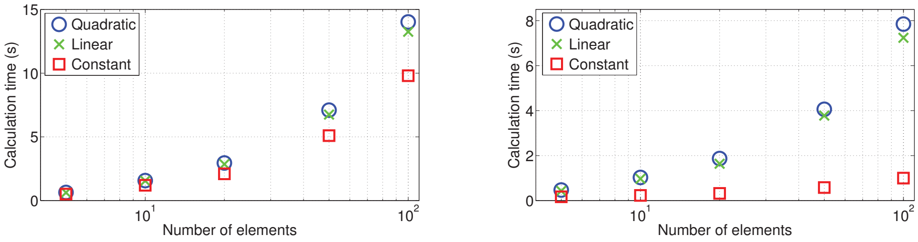

(a) Calculation time splash zone member **(b)** Calculation time submerged member

Figure 4.5: Calculation time for the different interpolation methods.

After the multiplication of the shape functions and the distribution function, the result is integrated according to equation 4.66. This yields the nodal forces and moments in terms in the element local axis system. Since these forces eventually have to be applied in the dynamic analysis, the final step is rotate the nodal forces back the global axis system. This completes the calculation of the wave forces, in accordance with the third block in the model flow chart (figure 4.1).

4.2.4 Verification

The wave load model is verified using the software USFOS [25]. USFOS does not have the capabilities to model second-order irregular waves, nor can it use the Taylor expansion method for the kinematics. In order to make a fair comparison, linear regular waves are used with a vertical extrapolation of the wave kinematics. An example is given for a member in the splash zone, inclined along the propagation direction of the wave as depicted in figure 4.7. Figure 4.6 shows the comparison of the inertia force in x-direction between the Matlab model and USFOS, both in the time and in the frequency domain.

The example case uses a hydrodynamic discretization of 1 m and a time step of 0.1 s. It can be seen in figure 4.6a that the time signals match well. An obvious dis-

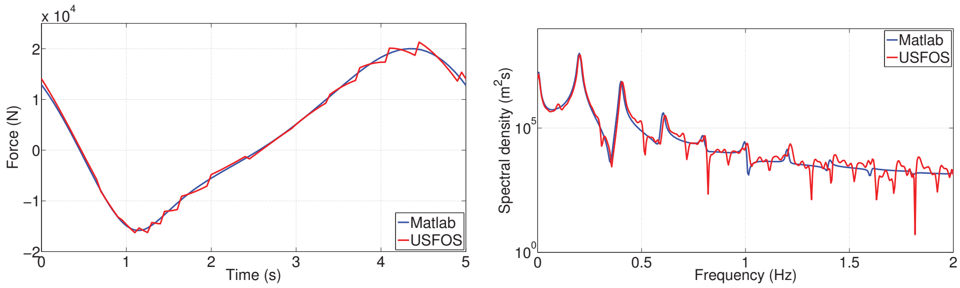

(a) Time domain.

(b) Frequency domain.

Figure 4.6: Inertia force on a inclined member in the splash zone.

crepancy is the zigzag pattern in the USFOS curve where the Matlab model yields a smooth curve. The zigzag pattern is due to the hydrodynamic discretization of the member. In USFOS, when the midpoint of an element becomes submerged the full element is being considered to be subjected to wave loading. This causes a continuous over- and undershooting of the actual wave forces, where the error becomes larger with an increasing hydrodynamic discretization. In the Matlab model, the first dry node is always put on the free surface such that the wave kinematics and the corresponding wave forces are calculated exactly up to the surface. An illustration of the procedure is given in figure 4.7.

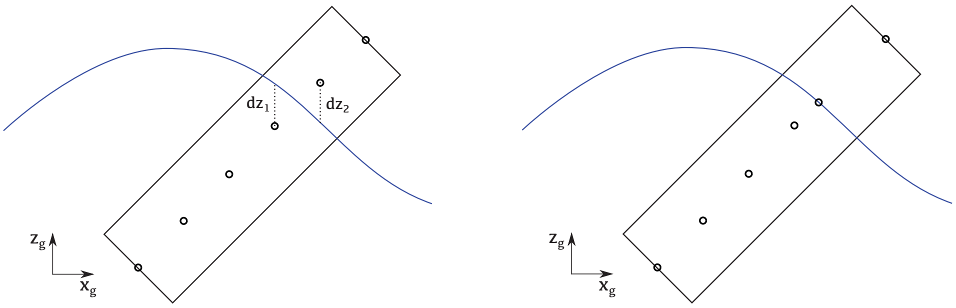

(a) Determine location of the surface node.

(b) Place the first dry node on the surface.

Figure 4.7: Moving coordinate Matlab model.

The moving coordinate ensures that the wave forces are calculated exactly up to the free surface which results in the smooth curve shown in figure 4.6a. The use of a moving coordinate has the advantage that the structural discretization can be easily enlarged without the introduction of the zigzag error. The fact that this error can have an influence on the dynamic response of the structure is illustrated by figure 4.6b. It can be seen that the zigzag pattern in the time domain introduces nonphysical effects in the frequency domain. For example, when an artificial force is introduced near one of the eigenfrequencies of the structure, it can cause an artificial response.

A verification is also carried out for the complete OC4 jacket structure (see section 4.3.1). The results of this verification in terms of resulting force in x-direction are presented in appendix C. The figures show that the Matlab model produces the same results as USFOS, only with a smoother curve. The zigzag pattern is less pronounced for the complete jacket since the total force on the jacket consists also of many submerged members, for which this effect is not present. It can be concluded that the Matlab model produces the correct results in terms of linear wave loads. The implementation of the moving coordinate ensures a smooth and exact representation of the forces and allows for a relatively large structural discretization.

4.3 Structural model

This section elaborates on the structural side of the model. First, the structural properties of the jacket and the tower that are used in the case study (section 4.4) are discussed in section 4.3.1. Secondly, the procedure how to get from hydrodynamic forces to stresses in the jacket members is discussed in section 4.3.2. Finally, the different reduced models that are used in the case study are introduced in section 4.3.3.

4.3.1 Jacket and tower model

In order to perform the case study described in section 4.4, a structural model of a jacket and a wind turbine are required. For the jacket model the "UpWind reference jacket" is used that was developed for the Offshore Code Collaboration Continuation (OC4) project. The jacket is hereafter referred to as the OC4 jacket and its detailed design is described in [45]. The tower model is based on the tower of the Siemens' 4MW offshore wind turbine, the SWT-4.0-130. The implementation of the jacket and tower is discussed below.

Jacket
The OC4 jacket is designed for 50 m water depth and has a total height of 68 m. The structure has four main legs which are interconnected via four bays of cross bracing. Figure 4.8 shows the OC4 jacket and the member properties are summarized in table 4.1.

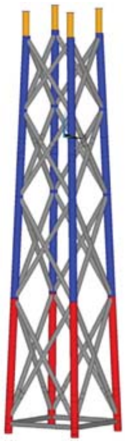

Figure 4.8: OC4 jacket [45].

Property set	Component	D_{out} (m)	t (mm)
1 (grey)	x- and mud braces	0.8	20
2 (red)	leg at lowest level	1.2	50
3 (blue)	leg 2nd to 4th level	1.2	35
4 (orange)	leg crossing TP	1.2	40

Table 4.1: Member properties OC4 jacket [45].

The jacket model implementation is based on [44] where the four legs and the bracing are modeled in Ansys using linear beam elements. The stiffness of the connection to the sea bed is assumed to be high and is therefore modeled as a rigidly clamped connection. Because of this assumption, any soil effects are excluded from the system. On the top side the jacket is connected to the tower via the transition piece (TP). This is again a rigid connection and the interface to the tower is made using a 6-DoF coupling. This is the only boundary node of the jacket as is further explained in section 4.3.3. Marine growth, water inside the free-flooded legs and added mass are included in the mass model of the jacket in terms of nodal point masses, as described in [44].

Tower

The SWT-4.0-130 tower has a base diameter of 5.5 m and tapers to a top diameter of 3.1 m. The total height of the tower is 68.8 m where the RNA is modeled as a lumped mass. This means that in the simulations no wind loads, controller settings or other aerodynamic related forces are taken into account. The tower has a 6-DoF interface at the bottom that corresponds to the interface of the jacket.

Damping is applied to the complete system by means of Rayleigh damping. The damping is tuned such that the first eigenfrequencies have a damping value of around 5% logarithmic decrement, corresponding to 0.8% damping ratio. Appendix B provides an overview of the eigenfrequencies of the complete OWT model and visualizations of first ten eigenmodes.

4.3.2 From hydrodynamic forces to member stresses

The geometry of the structure is first used to determine the hydrodynamic forces. In accordance with the Morison equation, these forces are dependent on the wave kinematics and the geometrical properties of the jacket members. As no relative velocity is taken into account, these forces contain no information about the response of the jacket. The response is considered separately in a dynamic analysis where the hydrodynamic forces are applied to the jacket nodes as external forces. Using the mass, damping and stiffness matrices representing the structural characteristics, the equations of motion are solved for the displacements, velocities and accelerations:

$$\boldsymbol{M}\ddot{\boldsymbol{u}} + \boldsymbol{C}\dot{\boldsymbol{u}} + \boldsymbol{K}\boldsymbol{u} = \boldsymbol{f} \tag{4.68}$$

The Newmark time integration method is used to solve the equations of motion, as described in appendix F. This eventually yields the structure's response in the global axis system. When considering the structural integrity of the system, the stresses in the structural members are of interest. These stress time signals can then be expressed in terms of fatigue damage, using rainflow counting and subsequently applying the S-N curve and the Palmgren-Miner rule. To accurately compute the fatigue damage in the member, stress concentration factors are required to account for local stress behavior, e.g. around the welds of the jacket nodes. The actual fatigue damages are important in the design phase of a foundation but to a lesser extent for the comparative study in this thesis. Therefore only the stresses are considered in chapter 5, as they provides a more transparent comparison of the two wave models. The stress time signals are converted to stress range bins using rainflow counting to determine the dominant excitation ranges.

To obtain the stress in a jacket member, the internal force vector $\boldsymbol{f}_e$ $[12 \times 1]$ is calculated for each time step from the element stiffness matrix $\boldsymbol{K}_e$ $[12 \times 12]$ and the displacements of the end nodes $\boldsymbol{u}_e$ $[12 \times 1]$:

$$\boldsymbol{f}_e = \boldsymbol{K}_e \boldsymbol{u}_e \tag{4.69}$$

The internal force vector contains the time series of the forces and moments in all three directions for the two end nodes of the member. In order to calculate the normal stress σ_{xx}, the normal force and the resulting bending moment need to computed. First the resulting moment M_r is calculated according to equation 4.70:

$$M_r = \sqrt{M_y^2 + M_z^2} \tag{4.70}$$

Also taking into account the normal force F_x, the normal stress is calculated according to equation 4.71:

$$\sigma_{xx} = \frac{M_r r}{I_y} + \frac{F_x}{A} \tag{4.71}$$

Where the area A and the area moment of inertia I_y are given by:

$$A = \pi\left(r_o^2 - r_i^2\right) \tag{4.72}$$

$$I_y = \tfrac{1}{4}\pi\left(r_o^4 - r_i^4\right) \tag{4.73}$$

Which in turn are defined by the outer diameter r_o and inner diameter r_i:

$$r_o = \frac{D}{2} \tag{4.74}$$

$$r_i = \frac{D}{2} - t \tag{4.75}$$

The shear stress σ_{xy} is dependent on the resultant shear force F_r and the torsional moment M_x. The resultant shear force is computed as follows:

$$F_r = \sqrt{F_y^2 + F_z^2} \tag{4.76}$$

The shear stress then given by:

$$\sigma_{xy} = \frac{M_x r}{J_x} + \frac{4F_r}{3A}\frac{r_o^2 + r_o r_i + r_i^2}{r_o^2 + r_i^2} \tag{4.77}$$

Where the area moment of inertia J_x is given by:

$$J_x = \tfrac{1}{2}\pi\left(r_o^4 - r_i^4\right) \tag{4.78}$$

To capture the total stress in an element, the Von Mises stress can be calculated. The location along the circumference is of the member where the maximum stress occurs is not specifically considered. The Von Mises stress can therefore be simplified according to equation 4.79:

$$\begin{aligned}\sigma_{vm} &= \frac{1}{\sqrt{2}}\sqrt{(\sigma_{xx}-\sigma_{yy})^2 + (\sigma_{yy}-\sigma_{zz})^2 + (\sigma_{zz}-\sigma_{xx})^2 + 6\sigma_{xy}^2 + 6\sigma_{yz}^2 + 6\sigma_{zx}^2} \\ &= \frac{1}{\sqrt{2}}\sqrt{2\sigma_{xx}^2 + 6\sigma_{xy}^2}\end{aligned} \tag{4.79}$$

The Von Mises stress σ_{vm} is the stress that is referred to in chapter 5.

4.3.3 Reduced models

One of the goals of the thesis is to determine the most optimal reduced model, in terms of accuracy and computational time. In order to do so, several of the methods discussed in chapter 3 are applied to the OC4 jacket. Table 4.2 summarizes the different reduced models that are used in the case study.

Name	Method	Stat. modes	Vib. modes	MTAs
CB00	Guyan	6	0	0
CB20	CB	6	20	0
CB10M10	ACB	6	10	10
M20	MTA only	6	0	20

Table 4.2: Reduced models used in the case study.

The reduced models are a combination of static constraint modes, fixed interface vibration modes and MTAs. The different types of modes are illustrated in appendix B. Each of the models contains the six static constraint modes, based on the interface node of the jacket, where the foundation is attached to the tower. As the CB00 model only contains these modes, this is in fact the Guyan model. The variation in the use of the other two types of modes is made in order to investigate the influence and relative importance of spectral and spatial convergence. For the jacket model, only the top node is considered a boundary node, all other nodes are internal nodes. As discussed in chapter 3, both the Guyan method and the Craig-Bampton method, do not take into account any loading on the internal DoF. As nearly all of the internal DoF of the jacket are subjected to external, hydrodynamic loading, the Augmented Craig-Bampton method is a promising way to enhance spatial convergence. The models contain only first order MTAs and the assembly of the foundation model and the tower model is performed using primary assembly.

4.4 Case study

The objective of this thesis consists of two parts. Firstly, the difference in response is investigated when using a linear or a nonlinear irregular wave model. Secondly, the performance of several reduced models is compared in terms of spectral and spatial convergence. In order to be able to perform these tasks, a set of load cases is defined to which the jacket structure is subjected. The data for this load case table is based on measurements from a typical project in the German Bight. The data consists of scatter diagrams ($H_s - T_p$) for twelve wave directions. In total this would lead to around 1200 different load cases that need to be considered. It is noted that these load cases are just wave-only scenarios, in which no wind loading is taken into account. When wind conditions would also be considered, the variability in wind speed, direction and operational settings of the OWT would increase the number of load cases to over 10.000. This is what is done in the development phase of an offshore wind farm, but due to time and computational constraints, even the 1200 wave-only load cases can not all be considered in this thesis. Therefore a simplification of the input data is required. The load case table and the procedure to obtain it are explained in section 4.4.1. All other input parameters for the case study are presented in table 4.3.

Description	Var.	Value	Unit
Water depth	d	50	m
Water density	ρ	1025	kg/m^3
Hydrodyn. discr.	Δx	1	m
Time step	Δt	0.1	s
Simulation time	T_{sim}	600	s
Cut-in frequency	ω_{in}	0	rad/s
Cut-out frequency	ω_{out}	$4{\cdot}\omega_p$	rad/s
Drag coefficient	C_d	1	-
Inertia coefficient	C_m	2	-

Table 4.3: Input parameters for the case study.

4.4.1 Load case table

As stated before, the input data consists of a scatter diagram for each of the twelve wave directions, for example as presented in table 4.4. The wave height is presented in terms of H_{m_0} but is used here as H_s (see section 2.7.2).

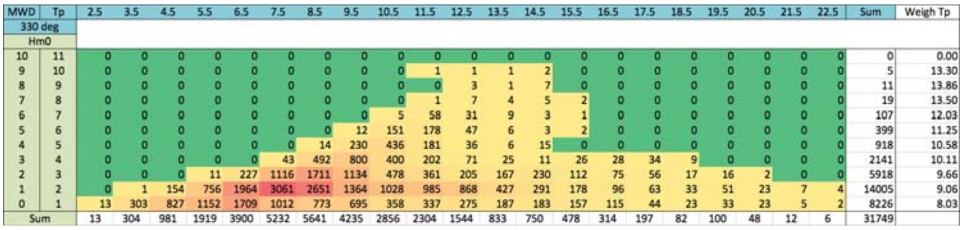

MWD	Tp	2.5	3.5	4.5	5.5	6.5	7.5	8.5	9.5	10.5	11.5	12.5	13.5	14.5	15.5	16.5	17.5	18.5	19.5	20.5	21.5	22.5	Sum	Weigh Tp
330 deg																								
Hm0																								
10	11	0	0	0	0	0	0	0	0	0	0	0	0	0	0	0	0	0	0	0	0	0	0	0.00
9	10	0	0	0	0	0	0	0	0	0	1	1	1	2	0	0	0	0	0	0	0	0	5	13.30
8	9	0	0	0	0	0	0	0	0	0	0	3	1	7	0	0	0	0	0	0	0	0	11	13.86
7	8	0	0	0	0	0	0	0	0	0	1	7	4	5	2	0	0	0	0	0	0	0	19	13.50
6	7	0	0	0	0	0	0	0	0	5	58	31	9	3	1	0	0	0	0	0	0	0	107	12.03
5	6	0	0	0	0	0	0	0	12	151	178	47	6	3	2	0	0	0	0	0	0	0	399	11.25
4	5	0	0	0	0	0	0	14	230	436	181	36	6	15	0	0	0	0	0	0	0	0	918	10.58
3	4	0	0	0	0	0	43	492	800	400	202	71	25	11	26	28	34	9	0	0	0	0	2141	10.11
2	3	0	0	0	11	227	1116	1711	1134	478	361	205	167	230	112	75	56	17	16	2	0	0	5918	9.66
1	2	0	1	154	756	1964	3061	2651	1364	1028	985	868	427	291	178	96	63	33	51	23	7	4	14005	9.06
0	1	13	303	827	1152	1709	1012	773	695	358	337	275	187	183	157	115	44	23	33	23	5	2	8226	8.03
Sum		13	304	981	1919	3900	5232	5641	4235	2856	2304	1544	833	750	478	314	197	82	100	48	12	6	31749	

Table 4.4: Scatter diagram for wave direction 330°.

In order to reduce the number of load cases to manageable proportions, a weighed average T_p is calculated for each H_s bin. This procedure reduces each of the twelve scatter diagrams to just a single load case per H_s. This method is hereafter referred to as the *weighted* T_p method. Applying this method to all directions yields a load case table of manageable proportions. Since the significant wave height data is provided in bins of 0.5 m, every two bins are assigned that same value for T_p. This leads to the simplified load case table as presented in table 4.5. The values in the table represent the weighted T_p and the cell color indicates the relative occurrence of each sea state.

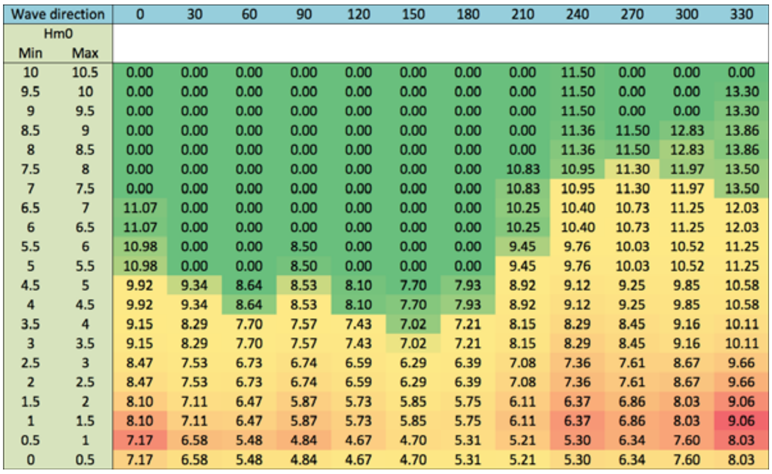

Wave direction		0	30	60	90	120	150	180	210	240	270	300	330
Hm0													
Min	Max												
10	10.5	0.00	0.00	0.00	0.00	0.00	0.00	0.00	0.00	11.50	0.00	0.00	0.00
9.5	10	0.00	0.00	0.00	0.00	0.00	0.00	0.00	0.00	11.50	0.00	0.00	13.30
9	9.5	0.00	0.00	0.00	0.00	0.00	0.00	0.00	0.00	11.50	0.00	0.00	13.30
8.5	9	0.00	0.00	0.00	0.00	0.00	0.00	0.00	0.00	11.36	11.50	12.83	13.86
8	8.5	0.00	0.00	0.00	0.00	0.00	0.00	0.00	0.00	11.36	11.50	12.83	13.86
7.5	8	0.00	0.00	0.00	0.00	0.00	0.00	0.00	10.83	10.95	11.30	11.97	13.50
7	7.5	0.00	0.00	0.00	0.00	0.00	0.00	0.00	10.83	10.95	11.30	11.97	13.50
6.5	7	11.07	0.00	0.00	0.00	0.00	0.00	0.00	10.25	10.40	10.73	11.25	12.03
6	6.5	11.07	0.00	0.00	0.00	0.00	0.00	0.00	10.25	10.40	10.73	11.25	12.03
5.5	6	10.98	0.00	0.00	8.50	0.00	0.00	0.00	9.45	9.76	10.03	10.52	11.25
5	5.5	10.98	0.00	0.00	8.50	0.00	0.00	0.00	9.45	9.76	10.03	10.52	11.25
4.5	5	9.92	9.34	8.64	8.53	8.10	7.70	7.93	8.92	9.12	9.25	9.85	10.58
4	4.5	9.92	9.34	8.64	8.53	8.10	7.70	7.93	8.92	9.12	9.25	9.85	10.58
3.5	4	9.15	8.29	7.70	7.57	7.43	7.02	7.21	8.15	8.29	8.45	9.16	10.11
3	3.5	9.15	8.29	7.70	7.57	7.43	7.02	7.21	8.15	8.29	8.45	9.16	10.11
2.5	3	8.47	7.53	6.73	6.74	6.59	6.29	6.39	7.08	7.36	7.61	8.67	9.66
2	2.5	8.47	7.53	6.73	6.74	6.59	6.29	6.39	7.08	7.36	7.61	8.67	9.66
1.5	2	8.10	7.11	6.47	5.87	5.73	5.85	5.75	6.11	6.37	6.86	8.03	9.06
1	1.5	8.10	7.11	6.47	5.87	5.73	5.85	5.75	6.11	6.37	6.86	8.03	9.06
0.5	1	7.17	6.58	5.48	4.84	4.67	4.70	5.31	5.21	5.30	6.34	7.60	8.03
0	0.5	7.17	6.58	5.48	4.84	4.67	4.70	5.31	5.21	5.30	6.34	7.60	8.03

Table 4.5: Simplified load case table for the case study: values represent weighted T_p and color indicates the relative occurrence.

Now that the both the significant wave heights and corresponding peak periods are defined, only one parameter is missing as an input to the JONSWAP spectrum; the peak enhancement factor γ. This factor can be calculated as a function of H_s and T_p according to equation 4.80.

$$\gamma = \begin{cases} 5 & \text{for} \quad \dfrac{T_p}{\sqrt{H_s}} \leq 3.6 \\ \exp\left(5.75 - 1.15\dfrac{T_p}{\sqrt{H_s}}\right) & \text{for} \quad 3.6 < \dfrac{T_p}{\sqrt{H_s}} \leq 5 \\ 1 & \text{for} \quad 5 < \dfrac{T_p}{\sqrt{H_s}} \end{cases} \tag{4.80}$$

With values for γ calculated, JONSWAP spectra can be created for each of the load cases. The load case table is used for both the comparison between the linear and nonlinear wave models (chapter 5), as well as for the performance analysis of the reduced models (chapter 6). Three different seeds are used for each of the $H_s - T_p$ combinations in order to improve statistical stability while maintaining a manageable number of load cases. No current is taken into account in any of the load cases.

A verification of the weighted T_p procedure is provided in appendix D. There the response triggered by the weighted T_p load case is compared to a weighted response of all individual load cases for two H_s bins. It is found that the weighted T_p case can yield a significantly different response in an absolute sense. However, the method seems to approximate the ratio of the stresses induced by the nonlinear wave model over the linear wave model relatively well. As the objective of the thesis is comparative by nature, the weighted T_p approach is assumed to be a valid simplification. The influence of this approach is only checked in terms of the wave model comparison as it is assumed that the model reduction study is not affected.

5

Results: linear vs. nonlinear waves

5.1 Introduction

The first objective of this thesis is treated in this chapter, i.e. determining the influence on jacket response of using a nonlinear wave model compared to a linear model. This influence is quantified on several levels. In section 5.2 the total stress in each of the individual members is calculated based on the load case table presented in section 4.4.1. This analysis determines the contribution of the nonlinear waves in terms of local effects. The nonlinear contributions are also examined on a more global scale in terms of the energy in the complete system. The comparison is carried out for the OWT model with a first eigenfrequency of 0.38 Hz and 5% logarithmic decrement damping. In order to check the sensitivity of the results, two sensitivity studies are carried out which are discussed in section 5.3. The damping sensitivity is analyzed by creating a structural model of which the logarithmic damping is enlarged from 5% to 30%. The sensitivity in terms of the eigenfrequency of the OWT is also considered. A second alternative model is created by adjusting the stiffness matrix of the jacket. This causes the eigenfrequency of the complete OWT system to be scaled down from 0.38 Hz to 0.28 Hz. The conclusions of this chapter are finally summarized in section 5.4.

5.2 Stress in jacket members

This section elaborates on the stresses in the jacket members. As discussed in section 4.3.2, the stresses here are presented in terms of Von Mises stress. Figure 5.1 illustrates the vertical stress distribution over the jacket. Figure 5.1b shows three focus members of the OC4 jacket that correspond to red bars in the figures on either side of it. The figure on the left side (5.1a) represents the normalized total stress distribution over the jacket members. This is obtained by calculating the stress in each member for all load cases in the load case table. Consequently, rainflow counting is performed on the stress signal and the stress range bins are simply multiplied by their number of occurrence and summed. The total stresses per load case are then weighted based on their relative occurrence in the load case table. This yields a total stress per member which is finally normalized to stress of the heaviest loaded member. The figure on the right hand side (5.1c) shows the ratio of the total stress induced by the nonlinear model with respect to the linear model.

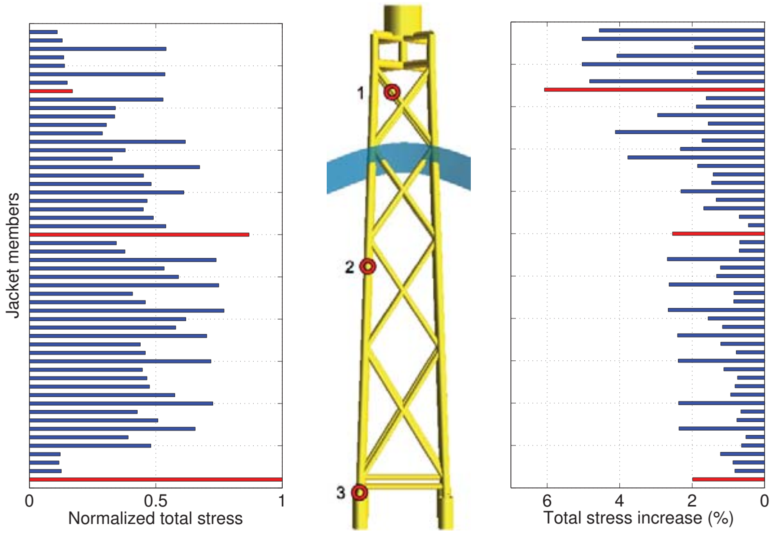

(a) Normalized weighted total stress.

(b) Focus members [25].

(c) Stress increase from nonlinear wave model.

Figure 5.1: Vertical stress distribution over jacket members.

In figure 5.1a it can be observed that the bottom part of one of the legs is the heaviest loaded member (3). The second heaviest loaded member is located half way down the jacket in the same leg (2). When looking at the stress ratios (figure 5.1c) it can be seen that the stress increase for these members is relatively low, i.e. the leg members experience a 2 to 3% stress increase. The nonlinear contribution increases when moving towards the splash zone. The highest ratio is found in one the cross bracings (1). In turn, the member with the highest ratio turns out to only have a minor contribution in terms of the total stress. To gain some more insight into how these stress levels are build up, focus member 3 is further analyzed below. Figure 5.2 shows the weighted number of occurrence of all stress bins, for both the linear and the nonlinear wave model.

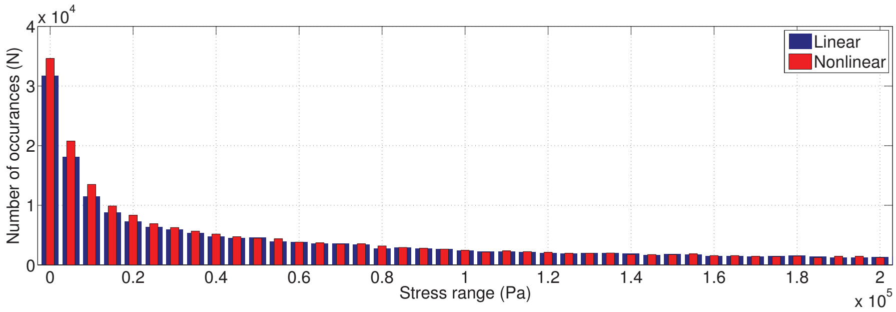

(a) Stress ranges from 0 to $2 \cdot 10^5$ Pa.

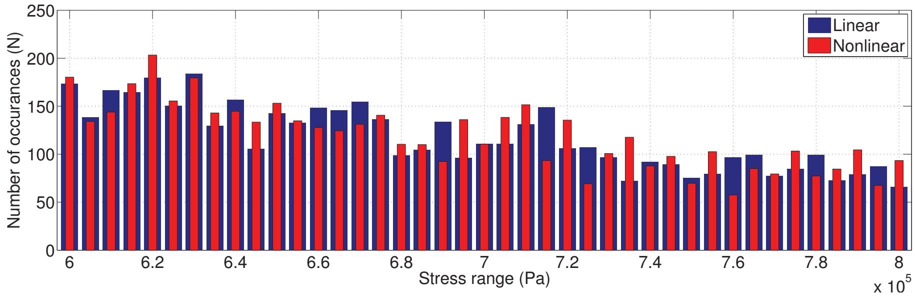

(b) Stress ranges from 6 to $8 \cdot 10^5$ Pa.

Figure 5.2: Weighted occurrence of stress ranges for focus member 3.

From figure 5.2a it can be seen that the difference between the linear and the nonlinear loading is most pronounced in the lower stress ranges. In the higher stress ranges the difference is harder to quantify as a small increase in the stress range will cause that specific occurrence to jump to the next stress bin. This explains the ambivalent pattern shown in figure 5.2b. The stress increase in the lower stress regions might be attributed to the sum frequency effect in the nonlinear waves. This effect generates high frequent, small amplitude waves which in turn cause stress with a similar properties.

The results presented so far are in terms of total stress, weighted over all load cases. This gives a good indication of global stress distribution in the jacket. In order to analyze the stress behavior in a single member, the stress in focus member 2 is considered separately. To also distinguish between the contributions of different load cases, three sea states are considered with varying values for the peak period. The load cases correspond to the cases considered in the verification of the load cases table (H_s = 1.5 m), presented in appendix D. A spectral analysis is performed on the member stresses in focus member 2, which is presented in figure 5.3a. The corresponding linear wave spectra are shown in figure 5.3b.

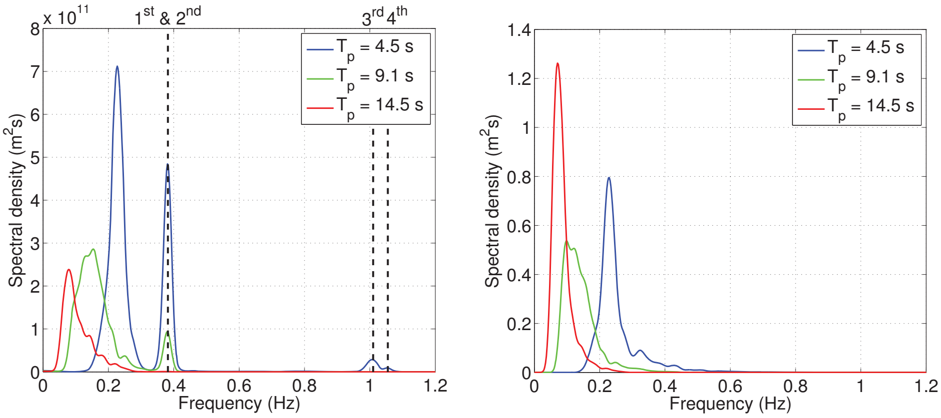

(a) Stress in focus member 2.

(b) Linear wave spectra.

Figure 5.3: Stress in focus member 2, induced by different sea states (H_s = 1.5 m).

This comparison is made to demonstrate that the different sea states trigger a different response in the jacket members. The peak period of the wave spectrum with T_p = 4.5 s is relatively close the first two eigenfrequencies of jacket. It is observed that a large response is triggered around the first two eigenfrequencies and even around the third and fourth eigenfrequency some response is present. The wave spectrum with T_p = 9.1 s displays only a minor response around the first two eigenfrequencies. For the case with a peak period of 14.5 s no stress is induced around the eigenfrequencies of the structure and only around the frequencies of the wave spectrum some response is triggered. The comparison is only shown for the linear wave spectra as these load cases have a very low amount of nonlinearity.

Another global measure to compare the two wave models is in terms of the potential and kinetic energy in the system. The potential energy represents the global deformation energy in the system and is a function of displacement and stiffness. The kinetic energy in the system indicates the level of dynamic response and is a function of velocity and mass. A low amount of kinetic energy thus points to a quasi-static response. In a fully resonant response the potential and kinetic energy are continuously exchanged (not taking damping into account). The potential and kinetic energy are calculated according to equation 5.1 and 5.2, respectively:

$$\boldsymbol{E}_p = \frac{1}{2}\boldsymbol{q}^T\boldsymbol{K}\boldsymbol{q} \tag{5.1}$$

$$\boldsymbol{E}_k = \frac{1}{2}\boldsymbol{v}^T\boldsymbol{M}\boldsymbol{v} \tag{5.2}$$

Figure 5.4 shows a time window around the maximum kinetic energy, induced by the highest sea state in the load case table (H_s = 10.25 m, T_p = 11.50 s). The energies are normalized with respect to maximum energy in the linear time series (t = 52 s). It can be seen that the nonlinear waves have a significant contribution to the kinetic energy in the system and thus trigger more dynamic effects than the linear model. On average over this time window, the energy induced by the nonlinear model is a factor 2.73 larger than that of the linear model. The highest sea state in the load case table is selected to clearly demonstrate the relative difference between the two wave models. For lower sea states the effect will be less pronounced, but still present.

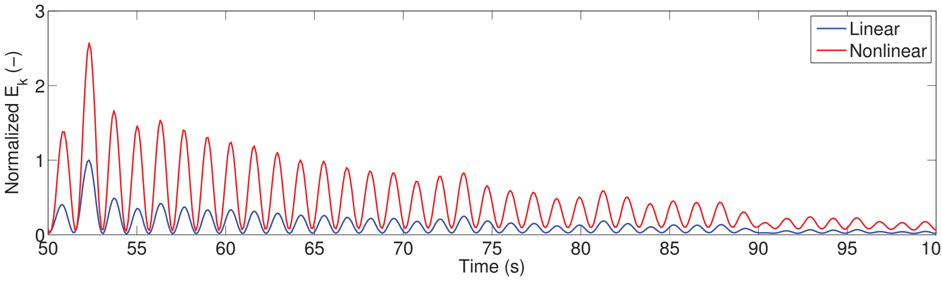

Figure 5.4: Maximum kinetic energy induced by the highest sea state (H_s = 10.25 m, T_p = 11.50 s), normalized with respect to the maximum linear energy (t = 520 s).

5.3 Sensitivity study

The results obtained in the previous section are checked here for sensitivity in terms of the eigenfrequency and the damping. In order to do so, two new structural models are created. For the first model the stiffness of the jacket foundation is scaled back to 37% of its reference stiffness to reduce the eigenfrequency of the complete structural model from 0.38 Hz to 0.28 Hz. This model is hereafter referred to as the *frequency model*. For the second model the frequency content remains unchanged but the damping value is increased 5% logarithmic decrement to 30% for the first two modes. This is done to simulate the aerodynamic damping that is generated by the rotor in operating conditions. This model is hereafter referred to as the *damping model*. Both models are subjected to the same set of wave loads as the *reference model* in section 5.2. The results are compared in terms of total stress and the ratio of the stresses, as well as the amount of energy in the system. Figure 5.5 shows the weighted nonlinear stress for all three models, normalized with respect to the maximum value of the reference model (figure 5.5a).

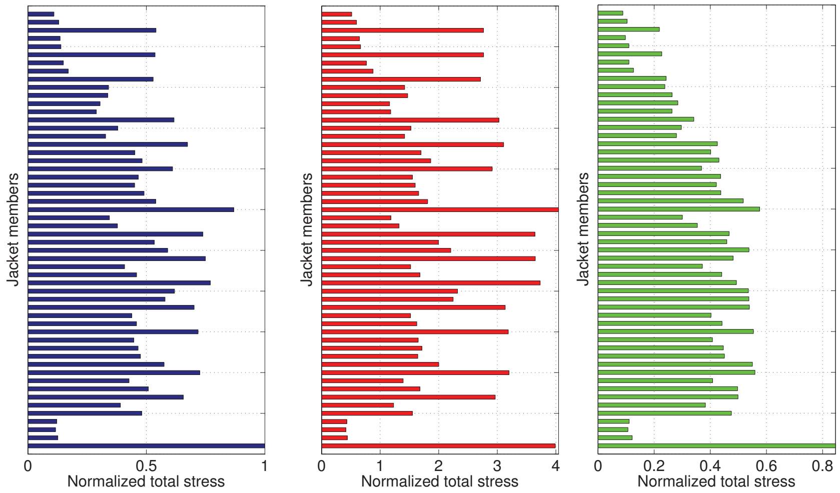

(a) Reference model. **(b)** Frequency model. **(c)** Damping model.

Figure 5.5: Total nonlinear stress normalized on the maximum value in figure 5.5a.

It can be clearly seen that the frequency model has the to endure the largest stresses. On average the stress is increased with about 400% compared to the reference model. The large spikes correspond to the leg members of the jacket. A similar distribution can be observed for the reference model and the damping, however significantly smaller in amplitude. It is noted that the results in figure 5.5a are the same as the data presented in figure 5.1a. Where the difference between the reference model and the frequency model is very large, the difference with the damping model is only small. Both observations can be explained based on the physical changes that the model adjustments imply. Due to the lowering of the eigenfrequencies of the frequency model its response spectrum moves more towards the wave spectrum by which the structure is excited. This causes significantly higher response than for the reference model, subjected to the same loading. The damping model has the same frequency content as the reference model but only experiences a higher damping of the response in the first two eigenmodes. The stress in the jacket members is on average around 20% lower for the damping model.

Figure 5.6 shows the difference between the three models but now in terms of the increase in stress due to the use of the nonlinear wave model compared to the linear wave model. It is noted that the results presented in figure 5.6a represent the same data as 5.1c. Figure 5.6b shows the results for the frequency model and figure 5.6c represents the data for the damping model.

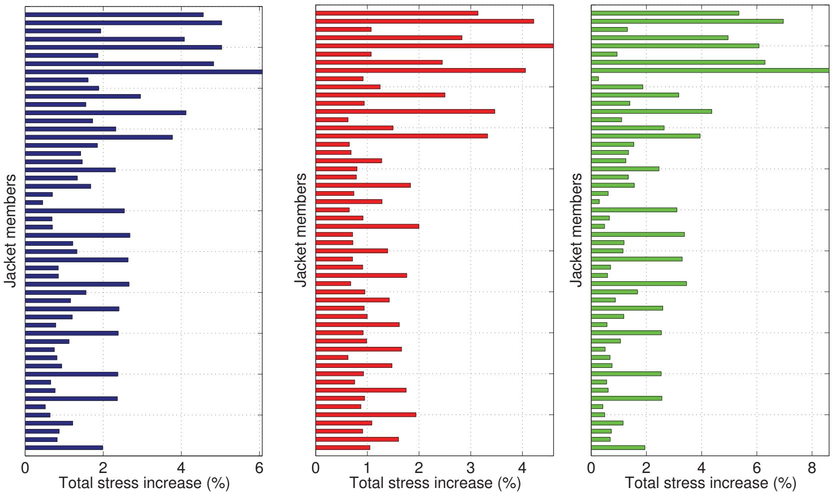

(a) Reference model. **(b)** Frequency model. **(c)** Damping model.

Figure 5.6: Stress increase of nonlinear wave model compared to the linear model.

It can be seen that the damping model yields the highest stress increase for the use of the nonlinear wave model. While the absolute stress significantly increased for the frequency model, the ratio of the nonlinear model over the linear model demonstrates a small decrease compared to the reference model. Further inspection of the response of the frequency model shows that, since the response to the linear waves increased so much, the second-order contribution becomes less pronounced and therefore shows a relatively smaller stress increase. The damping model demonstrates an increase in the nonlinear contribution with respect to the reference model. This can be explained by the fact that added damping is applied two the first two eigenmodes, which are closest to the linear wave spectrum. Since the response that is excited by the linear spectrum experiences a relatively higher damping, the nonlinear waves will naturally have a larger contribution.

Similar to the previous section, the different models are also compared in terms of kinetic energy in the system. Figure 5.7 provides an overview of the linear and nonlinear kinetic energy for the three models. It is noted that figure 5.7a is the same as figure 5.4, but it is repeated here in order to make a clear comparison between the models. The values of the other two figures are normalized with respect to the maximum value of the linear kinetic energy in the reference model.

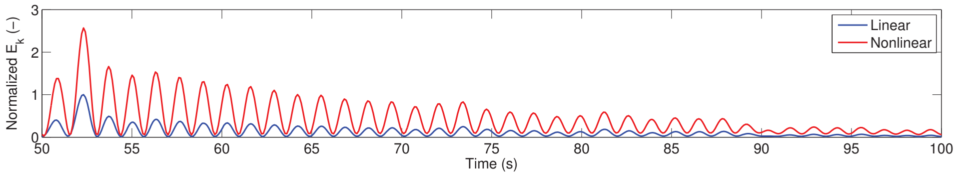

(a) Reference model (average increase factor 2.73).

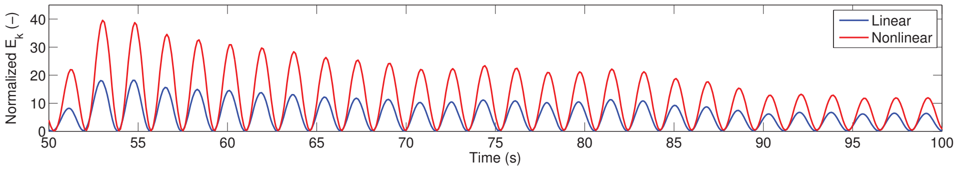

(b) Frequency model (average increase factor 1.85).

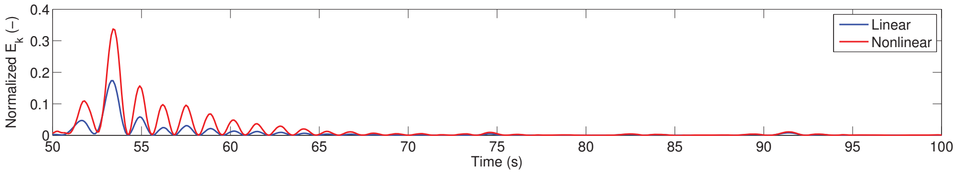

(c) Damping model (average increase factor 2.30).

Figure 5.7: Maximum kinetic energy induced by the highest sea state (H_s = 10.25 m, T_p = 11.50 s), normalized with respect to the maximum linear energy for the reference model (figure 5.7a).

The conclusions that can be drawn from figure 5.7 correspond well to conclusions based on the stress in the jacket members. First of all, it is noticed that the frequency model experiences a significantly higher kinetic energy than the reference model in an absolute sense. However, the ratio between the nonlinear and the linear energy again turns out to be smaller for the frequency model. Considering figure 5.7c, the influence of the increased damping is clearly illustrated by the behavior of the kinetic energy. Not only are the absolute values lower than in the reference case, also the amount of cycles for the kinetic energy to damp out is considerably less. For this specific case the average factor by which the energy is increased by the nonlinear model is slightly smaller than for the reference model. Concluding, the stress in the jacket members and the kinetic energy in the complete system generally demonstrate the same trends, both in absolute terms and in relative terms.

The two wave models are not only compared in terms of the response that they trigger, but also in terms of calculation time. In order to determine the difference, a number of runs is performed using the two models. In relation to the flowchart in figure 4.1, these runs include the whole process except for the dynamic simulation. A simulation time of $T_{sim} = 600$ s is used with a time step of $\Delta t = 0.1$ s. The average calculation time T_c for the two models is presented in table 5.1:

Model	T_c (s)
Linear	110
Nonlinear	200

Table 5.1: Average calculation times for linear and nonlinear wave model.

It can be seen that the nonlinear wave model causes a significant increase in the calculation time of the wave loads. However, this increase should not be considered by itself as the generation of the wave loads is only part of the calculation routine to determine the structure's response. Rather, the increase should be considered in terms of the combined calculation time of the wave load generation and the dynamic simulation. The calculation times of the dynamic simulation are discussed in chapter 6 and a final comparison is made in chapter 7.

5.4 Conclusions

The influence of the nonlinear wave model is compared to the linear wave model in terms of the total, weighted stress in the jacket members and energy in the complete system. For the reference model the following conclusions can be drawn based on section 5.2:

- Depending on the location of the member, the stress due to the nonlinear wave model can be 1% to 6% higher than for the linear wave model.
- The difference between the linear and the nonlinear wave model is most pronounced in the splash zone.
- When considering a single member, the stress increase is most pronounced in the lower stress ranges.
- The nonlinear wave model triggers more dynamic response than the linear wave model.

Furthermore, it is demonstrated that the T_p value of a sea state has a large influence on the response in the jacket members. In section 5.3 a sensitivity study is performed to check the influence of the eigenfrequency and the damping on the results obtained in section 5.2. The most important conclusions of the sensitivity study can be summarized as follows:

- Moving the structure's eigenfrequency towards the peak frequency of the wave spectrum significantly increases the stress in the members (on average 400%).
- Increasing the damping of the structure decreases the stress in the members (on average 20%).
- The damping model experiences the highest stress increase when using the nonlinear wave model compared to the linear wave model.
- Despite the strong increase in absolute terms, the relative contribution of the nonlinear waves becomes smaller for the frequency model.
- Increasing the damping on the first two modes causes a relatively higher contribution of the nonlinear wave model.
- The conclusions that are drawn based on the stress in the jacket members and the energy in the complete system are in good agreement with each other.

It is noted that the comparison is conducted for wave-only load cases. When wind loading is included the difference between the two wave models is expected to be less pronounced.

6

Results: Model reduction

6.1 Introduction

In this chapter the performance of the reduced models is presented and discussed. The goal here is to establish a link between the wave loading on the one hand, and the model reduction strategy on the other. Does different wave loading require a different (type of) reduced model? And if so, what would be an optimal model reduction strategy to accurately and efficiently handle a complete set of load cases? In order to answer these questions, nonlinear wave loads are calculated based on the load case table presented in section 4.4.1, and consequently a dynamic analysis is carried out using four different types of reduced models. As introduced in section 4.3.3, a Guyan model (CB00), a Craig-Bampton model (CB20), an Augmented Craig-Bampton model (CB10M10) and a MTA-only model (M20) are initially used and compared in terms of spectral and spatial convergence. The results of this comparative study are presented in section 6.2. In that same section different variants of the CB10M10 and M20 model are proposed with the objective to define a more generic reduced model.

Section 6.3 investigates the energy distribution over the included modes in the reduction basis for the CB10M10 models. As all results presented in section 6.2 and 6.3 are based on wave-only load cases, a sensitivity study of the effects of wind loads is discussed in section 6.4. The influence is measured both in terms of the overall model performance as well as the energy distribution over the different modes. Finally, the most important conclusions of this chapter are summarized in section 6.5.

6.2 Model comparison

The four main models as described in the introduction of this chapter are used to calculate the response of the complete OWT for the full loads case table. The performance of the models is compared in terms of their spectral and spatial convergence. The first is measured in terms of the error on the eigenfrequency of the system, the latter in terms of the error in the potential energy. The results of this comparison are presented in section 6.2.1. In the quest of a reduced model that is more generically applicable, several alternatives are compared in section 6.2.2.

6.2.1 Main models

The main models are first compared in terms of spectral convergence. This is done by calculating the eigenfrequencies of the complete OWT model, both with the full model as well as with the reduced models. The difference compared to the full model is plotted in figure 6.1.

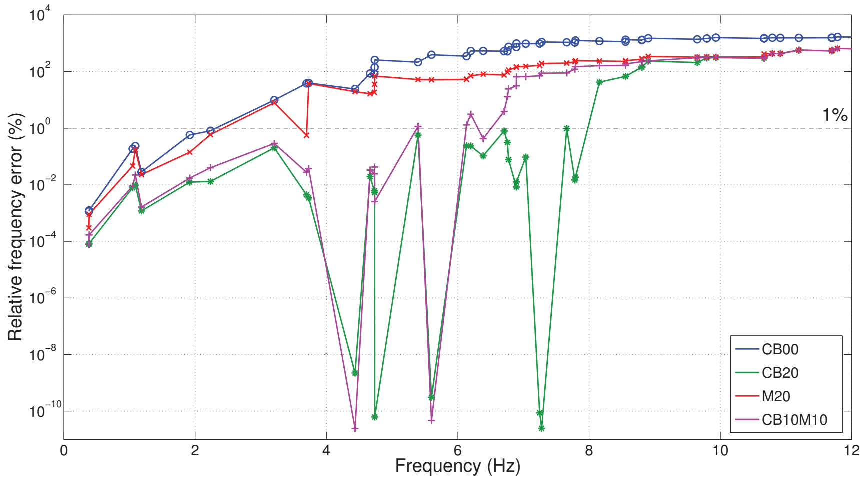

Figure 6.1: Relative error on the eigenfrequencies of the OWT.

It can be seen that the two models that include the fixed interface vibration mode shape (CB20 and CB10M10) have a significantly higher spectral convergence than the models without these mode shapes (CB00 and M20). This can be explained by the fact that the latter two models do not contain any dynamic information that is based on the structural properties of the jacket. These models are only accurate to a frequency of around 2.5 Hz after which the error becomes larger than 1%. The CB10M10 model provides accurate spectral information up to 6 Hz and the CB20 model even up to 8 Hz. Some very small errors are illustrated by the clear spikes in the green and the pink curve between 4 and 8 Hz. The corresponding frequencies turn out to only trigger localized effects in the jacket, which can be very well described by certain fixed interface vibration modes that are included in the reduction basis. This is illustrated by comparing the eigenfrequencies of the complete OWT with those of the fixed interface vibration modes. For example, the 11^{th} and the 17^{th} mode of the complete system have exactly the same eigenfrequency as the 3^{rd} and the 9^{th} fixed interface vibration mode, respectively.

It is remarked that the errors illustrated in figure 6.1 do not tell the whole story about accuracy of the response. Firstly, the errors should always be considered in combination with the forcing characteristics. For example when considering wave-only loads, the excitation frequencies can be found in the range of 0.05 to 0.5 Hz. When considering the frequency errors from this perspective, all four models demonstrate a good spectral convergence in this frequency range. Secondly, as illustrated in section 4.3.3, spectral convergence is only part of the story. In order to investigate the performance of the models in terms of spatial convergence, the response of the OWT is calculated for the full load case table using all four reduced models. For each of the load cases the potential energy is calculated, which represents the deformation energy captured in the system. From the time series of the potential energy the mean and the standard deviation of the signal is computed and the errors with respect to the full model are plotted in figure 6.2a and 6.2b, respectively. The error on the mean of the potential energy refers to the model's ability to represent the mean deformation, whereas the standard deviation is a measure to indicate the model's performance in terms of representing the oscillatory nature of the external force, establishing a link to the fatigue loads.

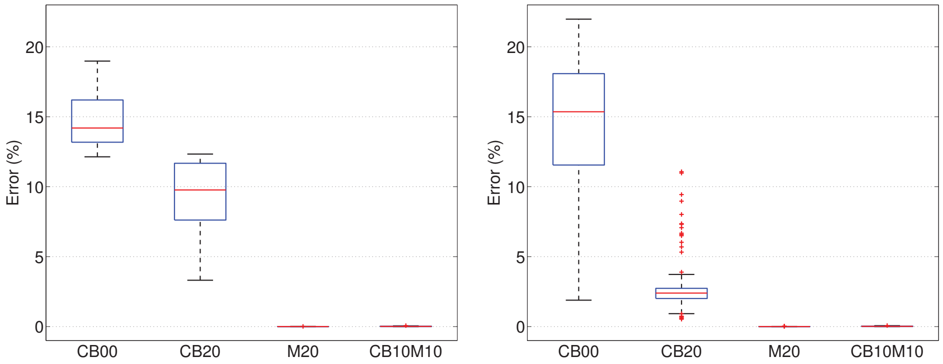

(a) Error mean potential energy.

(b) Error standard deviation potential energy.

Figure 6.2: Potential energy errors for all load cases for different reduced models.

Figure 6.2a and 6.2b both show the same trend: the CB00 and the CB20 model show relatively large errors while the CB10M10 and M20 models hardly show any error at all. These figures clearly demonstrate the value of using MTAs. Where the fixed interface vibration modes are the main driver for obtaining a good spectral convergence, the MTAs clearly have a valuable contribution when it comes to spatial convergence. The positive effect of the MTAs was to be expected as they are especially designed for the purpose of allowing the structure to deform in a specific load-induced shape. However, the almost negligible level of error of the models including MTAs in the reduction basis is remarkable. This can be seen as a clear illustration of the main drawback of the Guyan and the CB-only models and the main advantage of the use of MTAs, i.e. the representation of an external force on the internal DoF. Due to the fact that nearly all jacket DoF are considered as internal DoF (only the top DoF are boundary DoF), while most of these DoF are exposed to external, hydrodynamic loading, make the MTAs specifically valuable in the model reduction of a jacket structure.

Similar to the linear and nonlinear wave model, the calculation times of the reduced structural models is also considered. Referring back to the flowchart in figure 4.1, only the dynamic simulation is considered here. In order to determine the gain in calculation time, a number of simulations is performed using the software package BHawC. The simulations are run for a simulation time of T_{sim} = 600 s, using a time step of Δt = 0.02 s. No distinction is made between the different types of reduced model as all nearly have the same size relative to the full model. The results are presented in table 6.1:

Model	DoF	T_c (min)
Full	1300	250
Reduced	400	30

Table 6.1: Average calculation times for full and reduced model.

The values of the calculation time T_c in table 6.1 demonstrate the power of the reduced models. The dynamic simulation is performed nearly ten times faster using a reduced model compared to a full model. As shown before, the price to pay for this significant time reduction is very small, i.e. the CB10M10 and M20 models display an almost negligible error. These results establish that the use of reduced models not only causes a large gain in computational efficiency, but achieves this while guaranteeing a high level of accuracy.

6.2.2 Generic model

For the CB10M10 and the M20 models described in the previous section, the MTAs were calculated based on the applied force for each specific load case. This means that, when considering all 489 load cases in the load case table (169 cases times 3 seeds) one ends up with 489 different reduced models. Despite the fact that these specifically designed models clearly provide the highest level of accuracy, the computational time of all the sets of MTAs and obvious bookkeeping issues provide certain drawbacks to this model reduction strategy. Therefore, in this section several other strategies are investigated to find a more generically applicable reduced model.

In order to end up with a smaller amount of reduced models, a number methods is considered in which several load cases are clustered. In the case where the MTAs are calculated for each specific load case, the POD technique (see appendix E) is applied to the force vectors of that specific case. In the different clustering methods the snapshot matrices of the hydrodynamic force of the considered load cases are first normalized. Next, they are concatenated in time such that the matrix to which the POD is applied covers multiple load cases. The MTAs obtained using this strategy thus contain the dominant modes triggered by a combination of load cases. The clustering is performed for three different scenarios, namely per direction (*dir*), per significant wave height bin (*hs*) and for all load cases combined (*tot*). The performance of these models is compared to that of the models designed for each specific (*spec*) load case. Table 6.2 provides an overview of the number of reduced models using each of these strategies. It is noted that the difference in terms of calculation time to obtain the different models is negligible.

Model	Clustering	# models
spec	N.A.	489
dir	per direction	12
hs	per H_s bin	11
tot	all load cases	1

Table 6.2: Different reduced models strategies.

The above mentioned clustering strategies are implemented in the two models containing the MTAs: CB10M10 and M20. Again, the response for all load cases is calculated using these reduced models and the results in terms of the error in mean and the standard deviation of the potential energy are plotted in figure 6.3a and 6.3b, respectively. It is noted that the CB10M10spec and M20spec models in figure 6.3 represent the same data as CB10M10 and M20 in figure 6.2.

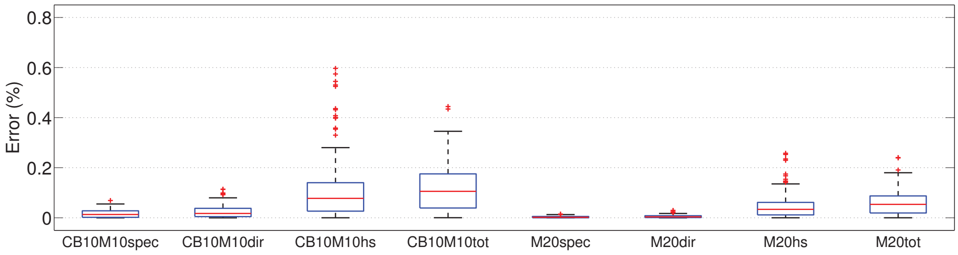

(a) Error mean potential energy.

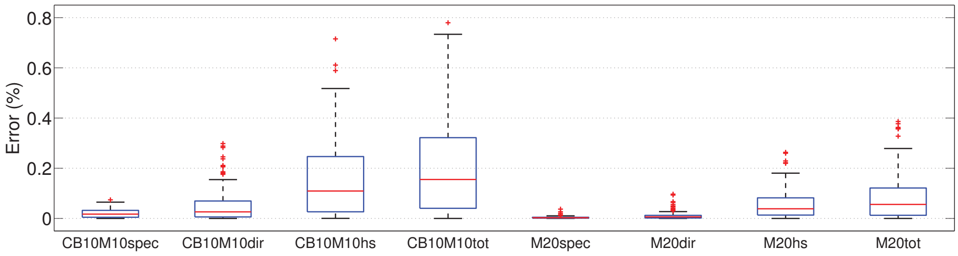

(b) Error standard deviation potential energy.

Figure 6.3: Potential energy errors for all load cases for different realizations of the CB10M10 and M20 models.

Based on figure 6.3 a number of observations can be made:

- All models perform relatively well. For all load cases all models provide an error smaller than 1%, both in terms of the mean and the standard deviation of the potential energy.
- For both model types (CB10M10 and M20) the same trend can be observed: the specific model performs best, the *dir* models performs better than the *hs* models, which in turn performs better than the *tot* models. The reason that the *dir* models provide the best alternative to the *spec* models can be found in the fact that loading from the same direction will generally deform the structure in the same direction, whereas the MTAs in the *hs* models need to be able to describe deformations from all directions. For the single *tot* model it is obviously an even bigger challenge to accurately represent every single load case.
- The M20 models perform slightly better than the CB10M10 models. Including ten more MTAs thus improves the spatial convergence more than including ten fixed interface vibration modes.

Judging from the final conclusion one might wonder why to use fixed interface vibration modes at all. However, it is remarked that the load cases considered here only include wave loading, and no wind loading is taken into account. As discussed in section 6.2.1, the performance of a reduced model in terms of spectral and spatial convergence strongly depends on the forcing characteristics. Due to the relative low frequency content of the wave forces, the corresponding low frequency range is effectively the only region where the models are tested. As figure 6.1 illustrated, in the low frequency region all models have a relatively good spectral convergence. From figure 6.2 and 6.3 it became apparent that for that frequency range the spatial convergence is dominant when it comes to overall accuracy. When wind loading is included the system is subjected to forces containing a higher spectral content, such as for example around the blade passing frequency. In section 6.4 it is investigated whether the same conclusions can be drawn in terms of model accuracy when the load cases also include wind loading.

6.3 Modal contribution

In section 6.2 both the fixed interface vibration modes and the MTAs have demonstrated their value. In this section the CB10M10 model is decomposed in order to gain more insight in which of the specific modes within the reduced model is contributing most. To do so, a low, medium and high wave-only load case is selected and consequently the mean potential energy per mode is calculated. This is done by reducing the stiffness matrix $\boldsymbol{K}$ with only a single mode (i) from the reduction basis $\boldsymbol{R}$ and then pre- and post-multiplying that with corresponding modal amplitude q_i (equation 6.1).

$$E_{p_i}(t) = q_i(t)\boldsymbol{R}_i^T\,\boldsymbol{K}\,\boldsymbol{R}_i\,q_i(t) \tag{6.1}$$

Once the time signals of the potential energy per mode are obtained, the mean energy per mode is calculated and the values are normalized. The results for the low, medium and high wave-only (W-O) load cases can be observed in figure 6.4. The first ten modes represent the fixed interface vibration modes (blue), the last ten modes represent the MTAs (red).

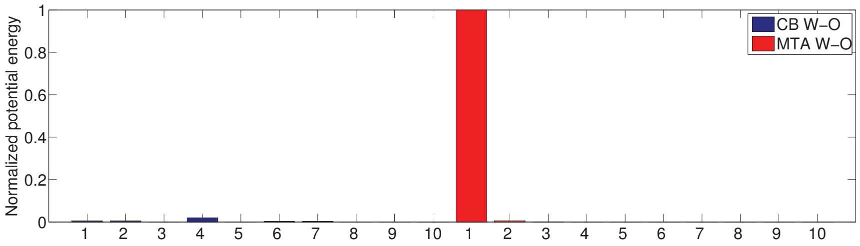

(a) Low sea state: $H_s = 0.75$ m, $T_p = 6.34$ s.

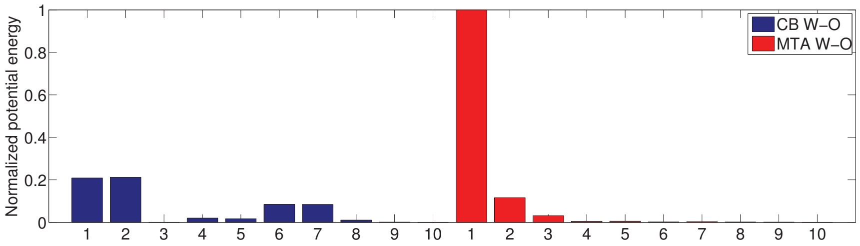

(b) Medium sea state: $H_s = 4.25$ m, $T_p = 9.25$ s.

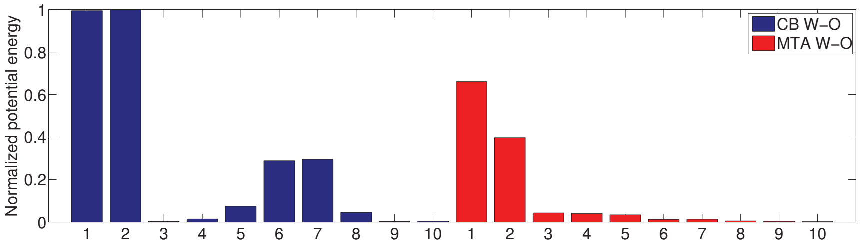

(c) High sea state: $H_s = 8.25$ m, $T_p = 11.50$ s.

Figure 6.4: Normalized potential energy per CB10M10 mode (wave-only loading).

Some interesting observations can be made when considering the differences in energy distribution for the three sea states. For the low sea state, almost all energy is absorbed by the first MTA mode. This could be explained by the fact that for this sea state little global response of the structure is triggered and that most deformation, however small, takes place on a local scale. As the sea state increases more potential energy is captured by the CB modes. Especially looking at figure 6.4c, the transition of the energy from the MTAs to the CB modes is clearly visible. Following the same rationale, the high sea state has more impact on a global scale and the CB modes therefore can offer a larger contribution in the description of the response shapes.

Also, as the sea state increases, the energy captured by the MTAs becomes more distributed over several modes instead of only the single mode for the low sea state. The higher the significant wave height becomes, the larger the spreading becomes in terms of instantaneous surface elevation. Consequently, it is logical that more load-dependent shapes are required to capture the response triggered by the increasingly diverse loading. The same behavior can be observed when considering figure 6.5.

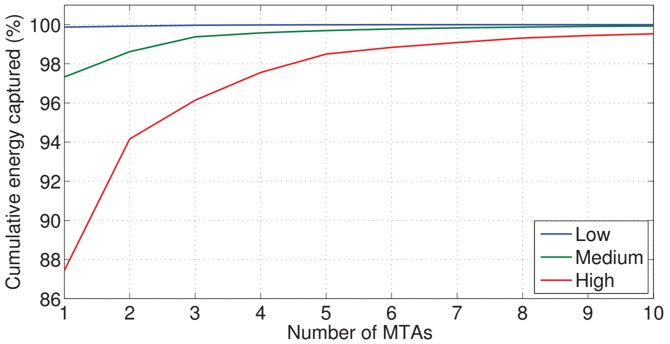

Figure 6.5: Cumulative energy captured by the first ten MTAs for the different sea states.

The curves in figure 6.5 represent the cumulative proper orthogonal values (POVs) of the first ten MTAs, corresponding the low, medium and high sea state. As explained in appendix E, the POVs indicate how much energy the corresponding POM captures. Figure 6.5 demonstrates that for a low sea state, almost all energy is captured by the first POM/MTA and the other nine modes hardly have any contribution. In the case of the high sea state the first mode captures around 87% of the energy and the next couple of modes still provide a significant contribution. The difference between the energies illustrated by figures 6.4 and 6.5, is that the first describes the potential energy captured in the dynamic simulation whereas the latter is solely based on the POVs of the external force and is thus independent of the structure. Since the two methods indicate the same trend, the development of a certain procedure could be considered where based on the POVs, a minimum number of MTAs is determined per load case before each dynamic simulation. Using this procedure, the reduced model size can be optimized in terms of accuracy and calculation time, for each specific load case.

6.4 Wind load sensitivity

In section 6.2 the performance of the different reduced models was based on wave-only load cases. In this section also wind loading is included while using the same load case table in terms of wave loading. The same wind loading is applied to all load cases. This is not a realistic scenario due to the correlation between wind speed and wave height. In order to obtain correct values for the loading in an absolute sense it would be required to apply a dedicated wind load corresponding to each of the sea states. However, as the current study is a sensitivity analysis for the performance of the reduced models, only a single wind load case is considered. The wind loading is calculated for the rated wind speed, thereby subjecting the tower to the maximum trust force, and is applied as a point force to the tower top.

In this section only the CB10M10 and M20 models are considered. The results for both the wave-only (W-O) cases as well as the wave-wind (W-W) cases are provided in figure 6.6a and 6.6b, respectively. Again, it is noted that the results for the CB10M10 W-O and M20 W-O are the same as the results initially shown in figure 6.2 for CB10M10 and M20.

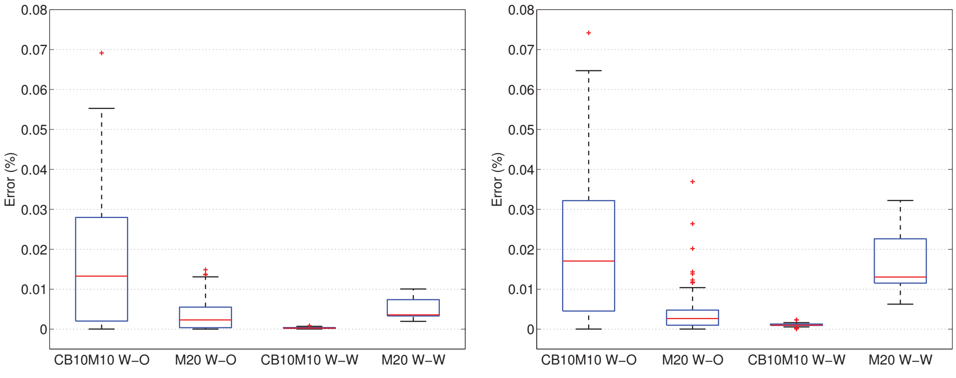

(a) Error mean potential energy. **(b)** Error standard deviation potential energy.

Figure 6.6: Potential energy errors comparison for wave-only (W-O) cases and wave-wind (W-W) cases.

An interesting observation that can be made based on figure 6.6, is that where M20 models performed better for wave-only loads, the CB10M10 models perform better for the wave-wind load cases. The reason for this can be found in the fact that the wind loads are introduced into the jacket through the interface node with the tower. The deformation shapes corresponding to this type of loading are more likely to be well represented by the CB modes (mainly global behavior) than by the MTAs (mainly local behavior). Also, since the wind loading contains more high frequent components, the difference in spectral convergence between the CB10M10 and the M20 models will play a more important role too. Figure 6.7 shows the distribution of the potential energy over the different CB10M10 modes, for the same low, medium and high load case as in figure 6.4.

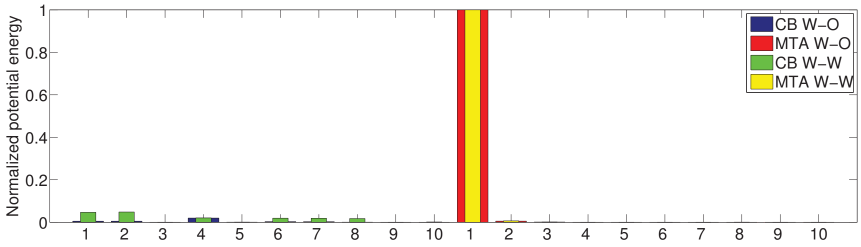

(a) Low sea state: $H_s = 0.75$ m, $T_p = 6.34$ s.

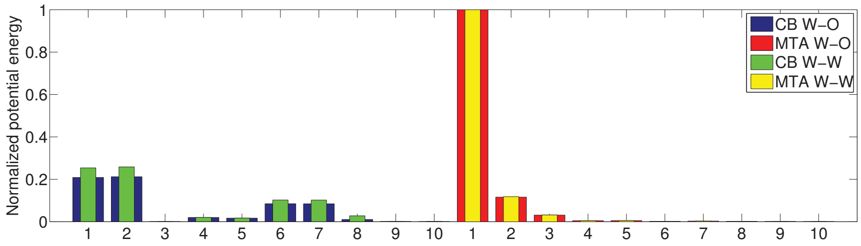

(b) Medium sea state: $H_s = 4.25$ m, $T_p = 9.25$ s.

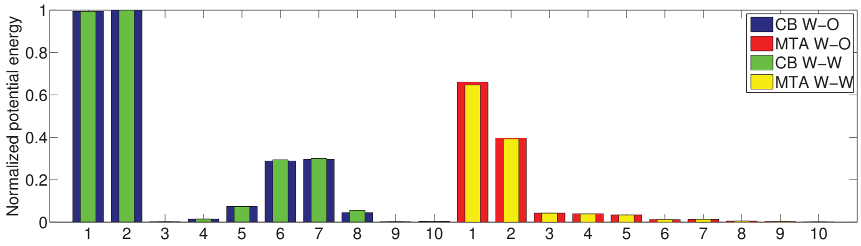

(c) High sea state: $H_s = 8.25$ m, $T_p = 11.50$ s.

Figure 6.7: Normalized potential energy per CB10M10 mode (wave-wind loading).

It can be seen that energy captured by the MTAs remains almost the same compared to the wave-only cases, but the CB modes represent a relatively higher part of the energy. The influence is largest for the low sea state, which can be explained by the fact that the same wind load will have a relative larger contribution on the low sea state case. The higher contribution of the CB modes corresponds to the increased accuracy of the CB10M10 model, as was illustrated by figure 6.6. Next to the extra energy in the CB modes, it is also likely that a lot of the extra energy due to the wind load is captured by the Guyan modes. Despite the fact that they do not contain any dynamic information, the Guyan modes should be able to reasonably well represent the response due to the mean trust force.

6.5 Conclusions

A number interesting findings have been done in the previous sections, both in terms of accuracy and computational efficiency of the reduced models. The most important conclusions are summarized as follows:

- Including fixed interface vibration modes significantly increases the spectral convergence of the reduced model.
- Including MTAs significantly increases the spatial convergence of the reduced model.
- Spatial convergence proves to be dominating for the wave-only cases, thereby making the M20 models the most accurate.
- Using a reduced model decreases the computational time nearly with a factor 10 compared to the full model.
- When wind loading is included, the features of the fixed interface vibration modes become more attractive and the CB10M10 model is the most accurate.
- In terms of energy distribution over the individual modes: for low sea states the MTAs almost carry all energy, for higher sea states the CB modes become more important.
- All models containing MTAs provide a high level of accuracy. Depending on the allowable error, the *tot* model provides an attractive alternative to the *spec* models.

Overall it can be concluded that when a reduced model is carefully assembled, it can lead to a very significant reduction in computational time with a negligible loss of accuracy.

7

Conclusions and recommendations

7.1 Introduction

The overall goal of this thesis is to build a bridge between the fields of wave modeling and structural modeling. In order to do so in an efficient manner, this broad statement was delimited in terms of the thesis objective, as presented in section 1.4:

> *Develop an efficient, integrated calculation strategy for the dynamic fatigue load analysis of a jacket-based OWT subjected to nonlinear irregular wave loading.*

This objective was subsequently split up into the two following main tasks:

1. Implement a second-order irregular wave model for a jacket foundation and examine the difference with respect to a linear model.
2. Investigate model reduction techniques and develop an efficient application for the load analysis of an OWT.

This subdivision was made as both topics first required an in-depth analysis before being able to establish the relation between the two. In this final chapter the most important findings are summarized and used to determine to what extent the thesis objective is fulfilled.

7.2 Conclusions

The conclusions presented here are in accordance with the setup of the thesis: firstly the impact of the nonlinear wave model is discussed, secondly the findings regarding the reduced models are addressed. Finally, the relation between the two disciplines is established in relation to the thesis objective.

7.2.1 Linear vs. nonlinear wave model

A case study was performed using a typical site in the German Bight. The linear and nonlinear wave model were compared in terms of member stresses and energy in the complete system. For a weighted summation of the response of all load cases, it was found that the stresses in the members increase by 1% to 6% when using the nonlinear wave model. The increase is dependent on the member location and is most pronounced near the splash zone. Considering the kinetic energy in the system, the nonlinear wave model demonstrated a significant increase in the dynamic response of the structure.

A sensitivity study showed that the eigenfrequencies and the damping of the structure play an important role in determining the response of the structure, both in absolute terms as well as in relative (nonlinear vs. linear) terms. Despite the fact that the results from the case study are clearly site- and structure-dependent, it can be concluded that the nonlinear wave model contributes significantly to the response of the structure. The increase in computational time of the nonlinear model (T_c = 200 s) is relatively large compared to the linear model (T_c = 110 s), but the overall impact is small in relation to the subsequent dynamic response simulation (T_c = 30 min). It is therefore concluded that, for the sake of accuracy, the nonlinear wave model should be used instead of the linear model in the fatigue load analysis of a jacket-based offshore wind turbine.

7.2.2 Reduced model comparison

In the comparison of the reduced models, all models were subjected to nonlinear wave loading based on the load case table. The response to these load cases was calculated for the different reduced models and their performance was evaluated in terms of spectral and spatial convergence. It was established that the addition of fixed interface vibration modes significantly improves the spectral convergence, compared to a reduced model only containing static constraint modes (CB00). However, only including fixed interface vibration modes (CB20) still yielded a relatively large error in terms of potential energy in the system.

This problem was overcome by increasing the spatial convergence through the inclusion of Modal Truncation Augmentation vectors. Both models including these MTAs (CB10M10 and M20) demonstrated very small errors (max. 0.08%) in terms of potential energy compared to the full model. By clustering the load cases it was found that even a single reduced model (*tot*) yielded only a small error (max. 1%). In order to accurately describe the response to the relatively broad loading spectrum of wave and wind loading, it is concluded that the reduced model should include both fixed interface vibration modes and MTAs.

The great added value of the use of reduced models was exposed when considering the calculation time of the dynamic simulation. An average sized reduced model (± 400 DoF) is able to perform the dynamic analysis nearly ten times quicker than the full model (± 1300 DoF). When the reduced model is carefully composed, this substantial time reduction does not come at the price of a significant loss of accuracy.

Summarizing the findings above, it is concluded that the thesis objective is fulfilled. The nonlinear irregular wave model has been successfully implemented and its influence has been compared to the linear model. Furthermore, a strategy has been developed to compose an accurate and efficient reduced model, tailored to the specific external loading. Together these tools provide *an efficient, integrated calculation strategy for the dynamic fatigue load analysis of a jacket-based OWT subjected to nonlinear irregular wave loading.*

7.3 Recommendations

Two categories of recommendation are made based on the work performed in this thesis. The first category focuses on the simplifications that were made and what to do differently when performing a complete load analysis. The second category consists of recommendations regarding further development of the model and general ideas regarding future work.

7.3.1 Complete load analysis

- **Use a full load case table**
  Due to time constraints, the load case table used in the case study was based on a weighted T_p. As was illustrated in appendix D, this method can introduce large errors in terms of the absolute stresses. When performing a full stress analysis all specific $H_s - T_p$ combinations need to be considered, as the response of the structure is highly dependent on the T_p value. Another option to obtain a smaller load case table would be to calculate a weighted H_s for each T_p.
- **Use stress concentration factors to determine fatigue damage**
  For this thesis the stress concentration factors of the jacket members have not been taken into consideration. When performing a full fatigue analysis the stress concentration factors are required to translate the stresses into damages. It would be interesting to investigate how the nonlinear/linear ratio in terms of stresses compares to the same ratio in terms of fatigue damage.

7.3.2 Future work

- **Include a deterministic wave model**
  Currently the model is able to handle nonlinear irregular waves, but no nonlinear regular waves. This would be a practical addition from a designers point of view. In terms of the corresponding reduced model it is expected that the trend indicated by figure 6.5 will continue, i.e. the larger the wave height, the more MTAs are required to capture the increased spatial variation. Also, since an extreme wave is characterized by a high steepness, the impact-like loading of the wave is likely to trigger higher frequent response in the structure. In order to accurately represent this, more modes will have to be included in the reduction basis.

- **Develop a POV-based error estimation method**
  The energy distribution over the modes in the reduction basis has been shown to be heavily dependent on the external loading. An optimal balance between the fixed interface vibration modes and the MTAs could be established using the POVs. Based on the POVs it can be determined how much of the energy in the wave loading is captured by the corresponding POMs. Since the energy distribution over the POMs and the MTAs showed great resemblance, it is suggested to establish a relation between the error in response energy (compared to the full model) and the error in POM energy (compared including all POMs). Clearly the POVs already provide a useful indication for the amount of POMs to be incorporated to capture the energy in the wave loading, but a relation to the response error would even be more interesting from a load analysis point of view.

- **Reconsider the safety factor on fatigue loads**
  Through the implementation of the nonlinear wave model, the wave loads on the jacket foundation can be determined with a higher level of accuracy. Generally fatigue loads are calculated using a linear irregular wave model. To account for the inherent underestimation of the loads a safety factor is applied to the dynamic response. The use of a more accurate model allows for a smaller safety factor, which in turn might lead to lower loads and a less overdimensioned foundation. It is noted that a saving in terms of materials does not directly translate to a proportional cost reduction. This is due to the fact the fabrication of a jacket is relatively labor intensive. Therefore, further research is suggested in which the relation between the wave model accuracy, the use of the safety factor and its influence on the foundation costs are investigated.

A

Derivation wave problem

In this appendix a detailed derivation of the wave problem is given. The linearized equations in section A.4 form the starting point of section 2.3.

A.1 Equations of motion

The derivation of the equations governing the surface waves starts at the conservation laws. The velocity field can be described by the vector $\boldsymbol{V} = (u, v, w)$ at time t at the point $\boldsymbol{x} = (x, y, z)$, in a Cartesian coordinate system fixed in space. The velocity vector field defines the instantaneous velocity of the fluid at any location in space.

$$\boldsymbol{V} = u\boldsymbol{i} + v\boldsymbol{j} + w\boldsymbol{k} \tag{A.1}$$

Here $\boldsymbol{i}$, $\boldsymbol{j}$ and $\boldsymbol{k}$ are unit vectors defined along the x-, y- and z-axis, respectively. Assuming an incompressible fluid, the density ρ is constant, the continuity equation simplifies and describes the conservation of mass. In an incompressible fluid the velocity $\boldsymbol{V} = (u, v, w)$ satisfies the continuity equation at each point in the fluid.

$$\nabla \cdot \boldsymbol{V} = 0 \tag{A.2}$$

Where ∇ is the vector differential operator, defined by the partial derivatives $\frac{\partial}{\partial x}$, $\frac{\partial}{\partial y}$, $\frac{\partial}{\partial z}$. Next, the conservation of momentum is used to establish a momentum balance. This relation is based on Newton's second law, which states that the net force on an object is equal to the rate of change of its momentum $\rho\boldsymbol{V}$. Since ρ is constant, the left hand side of the momentum is equation is described by the acceleration field. This is obtained by taking the substantial derivative of the velocity field. The equation for the substantial derivative of a function $F(x, y, z, t)$ is provided in equation A.3:

$$\frac{DF}{Dt} = \frac{\partial F}{\partial t} + \boldsymbol{V} \cdot \nabla F \tag{A.3}$$

Here $\boldsymbol{V}$ is the velocity field at time t. When applying the substantial derivative to the velocity field, the acceleration field is obtained in accordance with equation A.4:

$$\frac{D\boldsymbol{V}}{Dt} = \frac{\partial \boldsymbol{V}}{\partial t} + \boldsymbol{V} \cdot \nabla \boldsymbol{V} \tag{A.4}$$

Here the first term is referred to as the *local acceleration* and rest of the acceleration terms are called *convective accelerations*. These accelerations in the fluid need to be balanced by the external forces acting on it. The right hand side of the momentum equation consist of the body forces, the pressure forces and the viscous forces. The body forces are included in the vector $\boldsymbol{F}$. A valid assumption for the water waves is that only body force acting on the fluid is the gravity potential [39]. Therefore $\boldsymbol{F}$ only has a contribution in the z-direction: $\boldsymbol{F} = (0, 0, -g)$. The pressure forces are due to the scalar pressure field $p = p(x, y, z, t)$. The viscous forces are given by a multiplication of the kinematic viscosity ν with the Laplace operator of the velocity field. The latter is a differential operator takes the divergence of the gradient of velocity field. Equating the acceleration field with the forces acting on the fluid, the momentum equation is found:

$$\frac{D\boldsymbol{V}}{Dt} = \boldsymbol{F} - \frac{\nabla p}{\rho} + \nu \nabla^2 \boldsymbol{V} \tag{A.5}$$

Equation A.2 and A.5 together represent the Navier-Stokes equations.

A.2 Potential flow

The Navier-Stokes equations can describe wide variety of flow phenomena. Computation Fluid Dynamics (CFD) is one of the fields using these equations to numerically solve flow problems. However, analytical solutions to these equations only exist for simple problems. Therefore two assumptions are made in order to simplify the governing equations. The first assumption is that the fluid is inviscid. Viscous forces are important in wave boundary layers, but not important for the overall wave motion. By neglecting the viscous term in the momentum equation, the Euler equations are found:

$$\frac{D\boldsymbol{V}}{Dt} = \boldsymbol{F} - \frac{\nabla p}{\rho} \tag{A.6}$$

Next, the vorticity vector Ω is introduced which is defined as the curl of the velocity vector:

$$\boldsymbol{\Omega} \equiv \nabla \times \boldsymbol{V} = \begin{pmatrix} \boldsymbol{i} & \boldsymbol{j} & \boldsymbol{k} \\ \frac{\partial}{\partial x} & \frac{\partial}{\partial y} & \frac{\partial}{\partial z} \\ u & v & w \end{pmatrix} \tag{A.7}$$

Equation A.7 yields:

$$\boldsymbol{\Omega} \equiv \left(\frac{\partial w}{\partial y} - \frac{\partial v}{\partial z}, \quad \frac{\partial u}{\partial z} - \frac{\partial w}{\partial x}, \quad \frac{\partial v}{\partial x} - \frac{\partial u}{\partial y} \right) \tag{A.8}$$

The second assumption is that the fluid is irrotational. When a fluid is irrotational, the velocity potential Φ can be introduced as follows:

$$\boldsymbol{V} = \nabla \Phi \tag{A.9}$$

Equation A.9 shows that the velocities can now be obtained by taking the gradient of the velocity potential. The velocity potential is a more convenient way of representing the velocities since one now deals with the scalar Φ instead of the vector $\boldsymbol{V}$. When inserting the velocity potential into the vorticity vector (equation A.7), it can be seen that the vorticity of a fluid described by a velocity potential is in fact zero.

$$\boldsymbol{\Omega} \equiv \left(\frac{\partial^2 \Phi}{\partial y \partial z} - \frac{\partial^2 \Phi}{\partial z \partial y}, \quad \frac{\partial^2 \Phi}{\partial z \partial x} - \frac{\partial^2 \Phi}{\partial x \partial z}, \quad \frac{\partial^2 \Phi}{\partial x \partial y} - \frac{\partial^2 \Phi}{\partial y \partial x} \right) = (0,0,0) \tag{A.10}$$

When inserting the velocity potential in equation A.2 (continuity), the following relation is obtained:

$$\nabla^2 \Phi = 0 \tag{A.11}$$

The velocity potential thus has to satisfy the above equation. This equation is known as the Laplace equation and is the governing equation for potential wave theory. So far, the fluid is assumed to be incompressible, inviscid and irrotational. Based on the fact that the fluid is irrotational, it can be concluded that:

$$\Omega_x = \frac{\partial w}{\partial y} - \frac{\partial v}{\partial z} = 0 \quad \rightarrow \quad \frac{\partial w}{\partial y} = \frac{\partial v}{\partial z} \tag{A.12}$$

By implementing this into the Euler equations, the following relations for the x-direction are obtained. Here only the x-direction is considered for illustrative purposes, but the same procedure can used for the y- and z-direction.

$$\frac{\partial u}{\partial t} + u \frac{\partial u}{\partial x} + v \frac{\partial v}{\partial x} + w \frac{\partial w}{\partial x} + \frac{1}{\rho} \frac{\partial p}{\partial x} = 0 \tag{A.13}$$

$$\frac{\partial u}{\partial t} + \frac{\partial}{\partial x}\left(\frac{u^2+v^2+w^2}{2} + \frac{p}{\rho} + gz\right) = 0 \tag{A.14}$$

$$\frac{\partial}{\partial x}\left(\frac{\partial \Phi}{\partial t} + \frac{|\nabla\Phi|^2}{2} + \frac{p}{\rho} + gz\right) = 0 \tag{A.15}$$

Spatial integration of equation A.15 yields the following:

$$\left(\frac{\partial \Phi}{\partial t} + \frac{|\nabla\Phi|^2}{2} + \frac{p}{\rho} + gz\right) = C_1(x,t) \tag{A.16}$$

Using a similar approach, equation A.17 and A.18 are obtained for the y- and z-direction, respectively.

$$\left(\frac{\partial \Phi}{\partial t} + \frac{|\nabla\Phi|^2}{2} + \frac{p}{\rho} + gz\right) = C_2(y,t) \tag{A.17}$$

$$\left(\frac{\partial \Phi}{\partial t} + \frac{|\nabla\Phi|^2}{2} + \frac{p}{\rho} + gz\right) = C_3(z,t) \tag{A.18}$$

Since equations A.16, A.17 and A.18 have the same left hand side, the following must hold:

$$C_1(x,t) = C_2(y,t) = C_3(z,t) \tag{A.19}$$

This must be true for any set of (x,y,z) coordinates and since C_2 and C_3 for example do not depend on x, nor can C_1. The same holds for the y- and z-direction and hence it can be stated that all integration coefficients can condensed into a single coefficient that is not dependent on space, only on time.

$$C_1(x,t) = C_2(y,t) = C_3(z,t) = C(t) \tag{A.20}$$

This yields the following equation which is known better as the *Bernoulli equation*:

$$\left(\frac{\partial \Phi}{\partial t} + \frac{|\nabla\Phi|^2}{2} + \frac{p}{\rho} + gz\right) = C(t) \tag{A.21}$$

The equation can be further simplified by including the time dependency of C into the velocity potential and thereby making C a constant which can be set to zero.

$$\left(\frac{\partial \Phi}{\partial t} + \frac{|\nabla\Phi|^2}{2} + \frac{p}{\rho} + gz\right) = 0 \tag{A.22}$$

The Bernoulli equation is nonlinear and is true for unsteady, irrotational and inviscid fluid motion.

A.3 Boundary conditions

In order to be able to find a solution to for the velocity potential, certain boundary conditions need to be imposed on the problem.

Kinematic bottom boundary condition
The sea bottom is impermeable, hence the vertical velocity there is equal to zero. This requirement is described by equation A.23 and is referred to as the kinematic bottom boundary condition (KBBC).

$$\frac{\partial \Phi}{\partial z} = 0 \quad \text{for } z = -d \tag{A.23}$$

Kinematic free surface boundary condition
Before deriving the kinematic free surface boundary condition (KFSBC), the meaning of a substantial derivative is recalled here. The definition is provided in equation A.3. Next, z is expressed in terms of the instantaneous free surface:

$$z = \eta(x, y, t) \tag{A.24}$$

Then, the function $F(x, y, z, t)$ is defined as follows:

$$F(x, y, z, t) = z - \eta(x, y, t) = 0 \tag{A.25}$$

The basic assumption for the KFSBC is that a particle at the free surface, stays at the free surface. This entails that equation A.25 is always satisfied and that the substantial derivative of F is equal to zero.

$$\frac{\partial}{\partial t}(z - \eta(x, y, t)) + \nabla \Phi \cdot \nabla (z - \eta(x, y, t)) = 0 \tag{A.26}$$

The KFSBC can than be formulated as:

$$\frac{\partial \eta}{\partial t} + \frac{\partial \Phi}{\partial x}\frac{\partial \eta}{\partial x} + \frac{\partial \Phi}{\partial y}\frac{\partial \eta}{\partial y} - \frac{\partial \Phi}{\partial z} = 0 \quad \text{for } z = \eta(x, y, t) \tag{A.27}$$

Here the fluid velocity $\boldsymbol{V}$ is expressed in terms of the velocity potential Φ.

Dynamic free surface boundary condition
The dynamic free surface boundary condition (DFSBC) imposes the statement that the water pressure at the free surface is equal to the constant atmospheric pressure p_0. If the constant C in the Bernoulli equation (A.21) is set equal to $\frac{p_0}{\rho}$, then the DFSBC is given as follows:

$$\frac{\partial \Phi}{\partial t} + \frac{|\nabla \Phi|^2}{2} + gz = 0 \quad \text{for } z = \eta(x, y, t) \tag{A.28}$$

A.4 Linearization of the wave problem

The Laplace equation (A.11), constrained by the two kinematic (A.23 and A.27) and the dynamic (A.28) boundary conditions describe the fully nonlinear wave problem in 3D. The two nonlinear free surface boundary conditions have to be satisfied at the instantaneous free surface. The issue is that the position of the free surface is not known before solving the problem. The nonlinear terms can be discarded by linearizing the wave problem. The governing assumption here is that the wave amplitude H is small with respect to the wave length L, hence the wave steepness H/L is small. This removes the nonlinear terms from the equations and entails that the boundary conditions are now to be satisfied at the mean sea level (MSL), $z = 0$, instead of at the instantaneous free surface η. Finally, only 2D waves in the x-z plane are considered here and therefore the y-direction is dropped from the equations.

The kinematic bottom boundary condition (A.23) is not affected by these simplifications but is mentioned here again for a full description of the 2D wave problem:

$$\frac{\partial \Phi}{\partial z} = 0 \quad \text{for } z = -d \tag{A.29}$$

The kinematic free surface boundary condition (A.27) is linearized to:

$$\frac{\partial \Phi}{\partial z} = \frac{\partial \eta}{\partial t} \quad \text{for } z = 0 \tag{A.30}$$

The dynamic free surface boundary condition loses the quadratic velocity term and is now described by:

$$\frac{\partial \Phi}{\partial t} + g\eta = 0 \quad \text{for } z = 0 \tag{A.31}$$

The 2D Laplace equation is obtained by disregarding the y-term in 3D Laplace equation (A.11).

$$\frac{\partial^2 \Phi}{\partial x^2} + \frac{\partial^2 \Phi}{\partial z^2} = 0 \quad \text{for } -d \leq z \leq 0 \tag{A.32}$$

The Laplace equation (A.32) and the three boundary conditions stated above (A.29, A.30 and A.31), formulate the 2D linearized wave problem. To summarize, this problem is based on the assumptions of a 2D incompressible, inviscid and irrotational fluid and a small wave steepness.

B

Eigenfrequencies and eigenmodes

This appendix contains the eigenfrequencies and eigenmodes of different structural models. The information corresponding to the complete OWT model is presented in section B.1. The three types of mode shapes are illustrated in the following sections: static constraint modes (section B.2), fixed interface vibration modes (section B.3) and Modal Truncation Augmentation modes (section B.4). Finally, the eigenfrequencies and corresponding damping values of the models used in the sensitivity study in section 5.3, are provided in section B.5.

B.1 Complete OWT model

#	Full (Hz)	CB00 (Hz)	CB20 (Hz)	M20 (Hz)	CB10M10 (Hz)
1	0.381	0.381	0.381	0.381	0.381
2	0.384	0.384	0.384	0.384	0.384
3	1.048	1.050	1.048	1.048	1.048
4	1.089	1.091	1.089	1.091	1.089
5	1.183	1.184	1.183	1.184	1.183
6	1.918	1.929	1.918	1.918	1.918
7	2.232	2.251	2.233	2.251	2.234
8	3.205	3.520	3.212	3.520	3.215
9	3.696	5.110	3.696	3.706	3.697
10	3.729	5.201	3.729	5.201	3.731
11	4.435	5.506	4.435	5.364	4.435
12	4.664	8.668	4.665	5.422	4.666
13	4.729	8.712	4.729	6.273	4.729
14	4.734	11.452	4.734	6.595	4.736
15	4.736	16.939	4.736	6.960	4.736
16	5.395	16.975	5.425	8.163	5.454
17	5.599	27.614	5.599	8.712	5.599
18	6.134	27.632	6.149	8.746	6.201
19	6.198	39.337	6.213	11.279	6.408
20	6.387	40.704	6.394	11.721	6.413

Table B.1: First 20 eigenfrequencies for different reduced models.

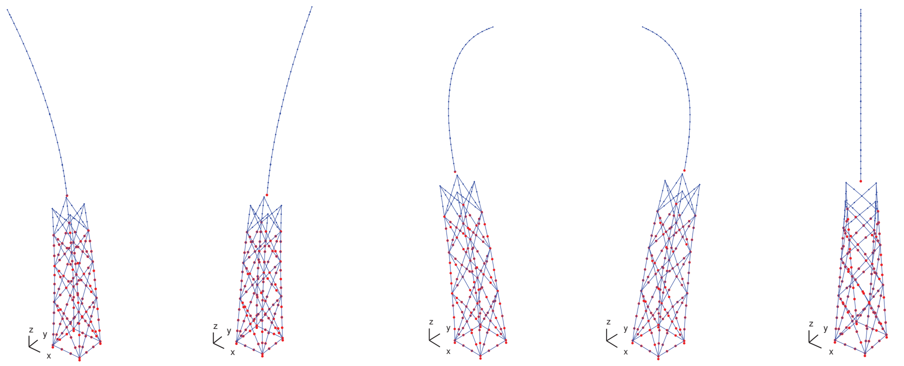

(a) Mode 1 **(b)** Mode 2 **(c)** Mode 3 **(d)** Mode 4 **(e)** Mode 5

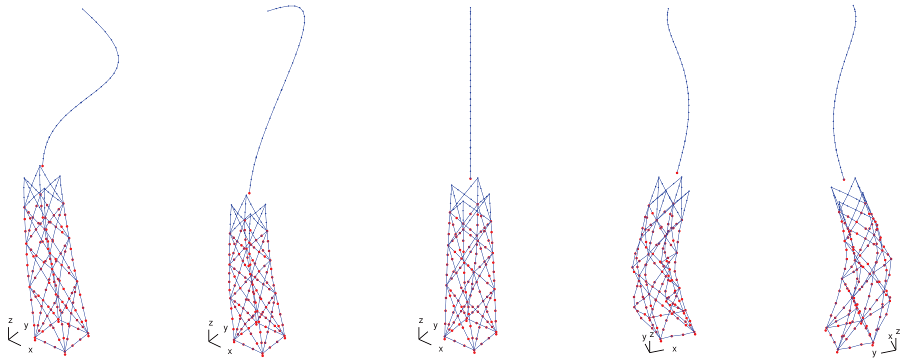

(f) Mode 6 **(g)** Mode 7 **(h)** Mode 8 **(i)** Mode 9 **(j)** Mode 10

Figure B.1: First ten eigenmodes of the OWT.

B.2 Static constraint modes

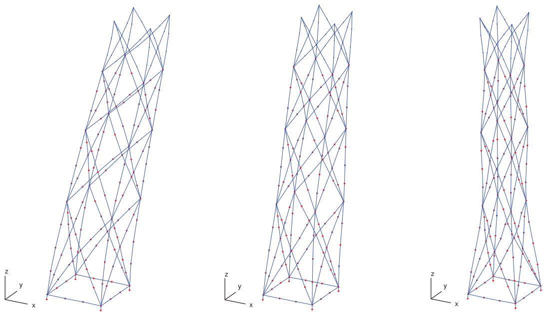

(a) Mode 1 **(b)** Mode 2 **(c)** Mode 3

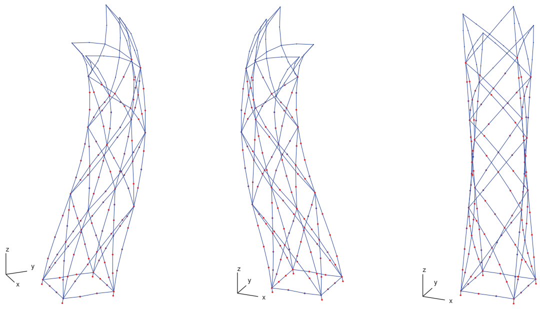

(d) Mode 4 **(e)** Mode 5 **(f)** Mode 6

Figure B.2: All six static constraint modes.

B.3 Fixed interface vibration modes

#	Freq. (Hz)
1	4.091
2	4.091
3	4.435
4	4.699
5	4.736
6	4.855
7	4.855
8	5.206
9	5.599
10	6.281

Table B.2: First 10 frequencies of the fixed interface vibration modes.

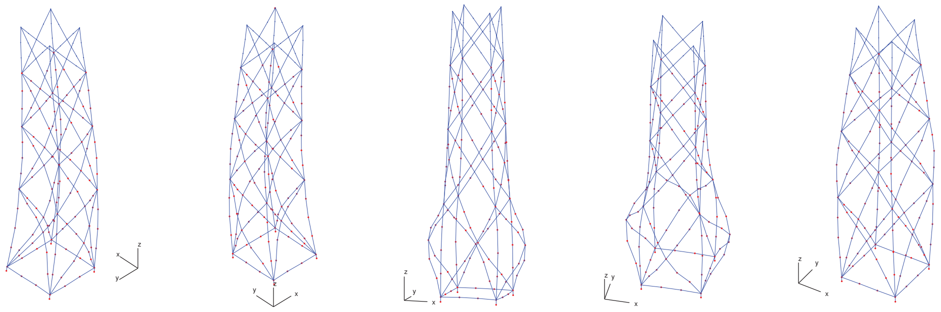

(a) Mode 1 **(b)** Mode 2 **(c)** Mode 3 **(d)** Mode 4 **(e)** Mode 5

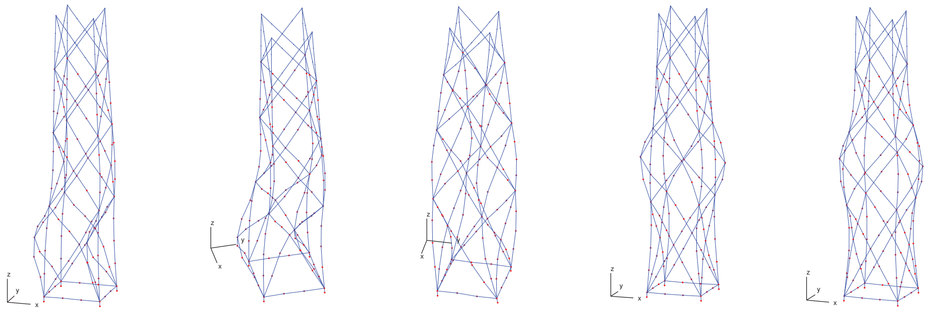

(f) Mode 6 **(g)** Mode 7 **(h)** Mode 8 **(i)** Mode 9 **(j)** Mode 10

Figure B.3: First ten Craig-Bampton modes.

B.4 Modal Truncation Augmentation modes

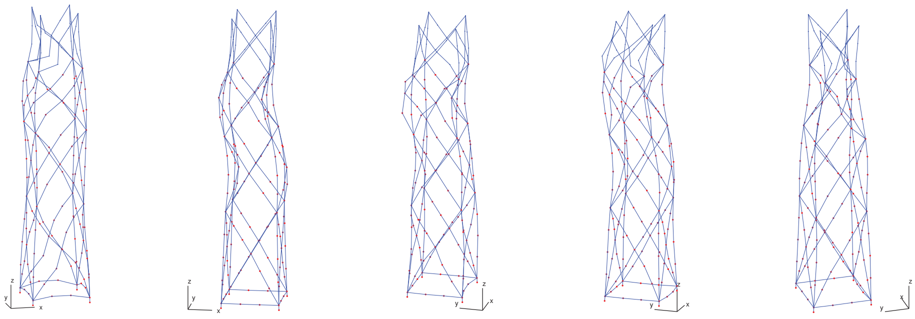

(a) Mode 1 **(b)** Mode 2 **(c)** Mode 3 **(d)** Mode 4 **(e)** Mode 5

Figure B.4: First five MTAs for the high load case of section 6.3.

B.5 Models sensitivity study

	Reference model		Damping model		Frequency model	
#	Freq. (Hz)	Damp. (%)	Freq. (Hz)	Damp. (%)	Freq. (Hz)	Damp. (%)
1	0.381	5.049	0.381	29.951	0.281	5.070
2	0.384	5.030	0.384	30.131	0.282	5.059
3	1.048	5.426	1.048	5.855	0.811	5.136
4	1.089	5.539	1.089	6.242	0.833	5.208
5	1.183	5.812	1.183	5.812	0.996	5.771
6	1.918	8.277	1.918	8.617	1.711	8.722
7	2.232	9.419	2.232	9.521	1.944	9.751
8	3.205	13.079	3.205	13.079	2.239	11.081
9	3.695	14.962	3.695	15.011	2.467	12.117
10	3.728	15.088	3.728	15.130	2.562	12.552
11	4.434	17.822	4.434	17.822	2.697	13.173
12	4.662	18.711	4.662	18.711	2.838	13.823
13	4.726	18.962	4.726	18.968	2.880	14.014
14	4.731	18.981	4.731	18.987	2.916	14.182
15	4.733	18.989	4.733	18.989	2.932	14.255
16	5.391	21.560	5.391	21.560	3.366	16.270
17	5.596	22.360	5.596	22.360	3.405	16.449
18	6.129	24.454	6.129	24.526	3.909	18.803
19	6.194	24.707	6.194	24.770	4.006	19.256
20	6.382	25.447	6.382	25.447	4.012	19.288

Table B.3: First 20 eigenfrequencies for models used in the sensitivity study in chapter 5, damping values are given in terms of logarithmic decrement.

C

Verification USFOS: OC4 jacket

In this appendix the verification of the Matlab code with the software package USFOS is illustrated graphically. The complete OC4 jacket is subjected to a regular wave with $H = 2.5$ m and $T = 5$ s. Figure C.1 shows the comparison of the total force in x-direction over the one wave period. A detailed representation of the window around the maximum force is presented in figure C.2. Both figures demonstrate that the two models match perfectly. The fact that the Matlab curve is smoother than the USFOS curve is due to the implementation of the moving coordinate, as explained in section 4.2.4.

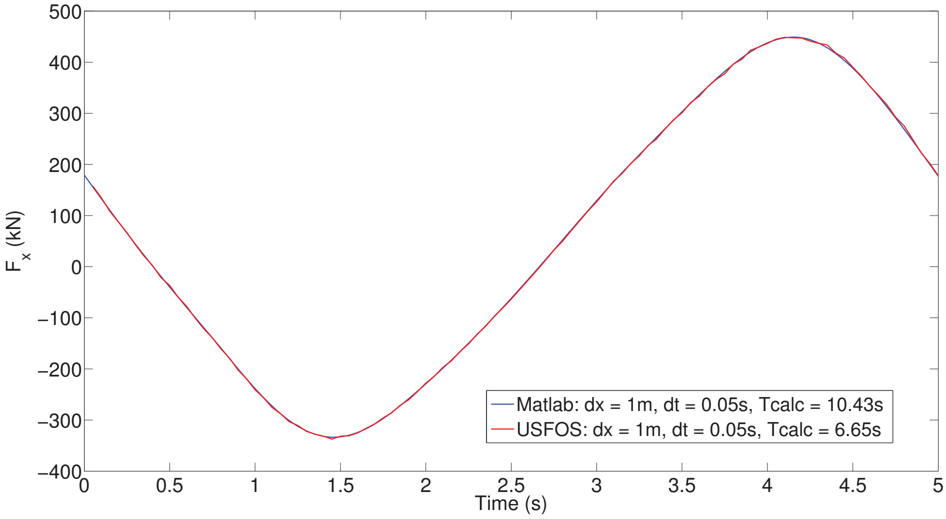

Figure C.1: Overview: comparison total force in x-direction F_x.

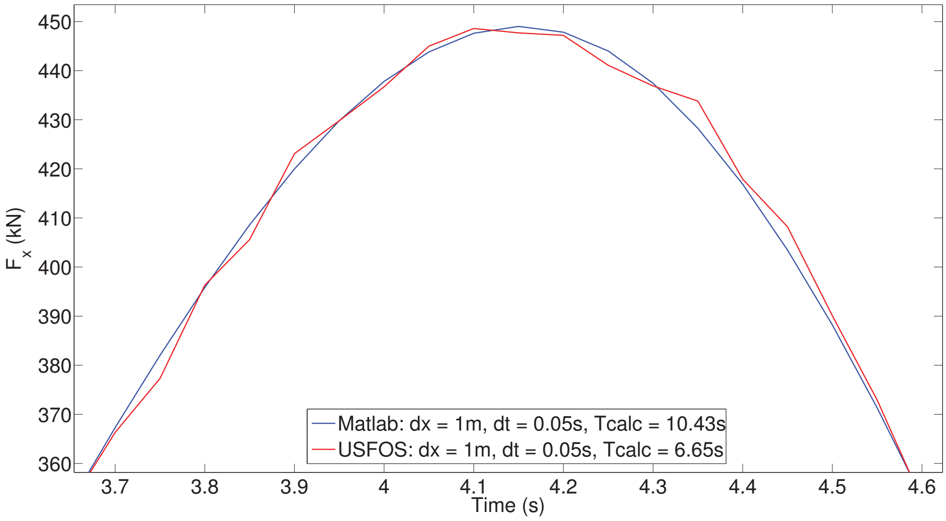

Figure C.2: Zoomed in: comparison total force in x-direction F_x.

D

Verification load case table

The validity of the weighted T_p method is verified in this appendix. For illustration purposes, a schematic representation of this method is depicted in the top line of figure D.1. The bottom line shows the procedure in which a specific T_p is used for each load case. The stresses based on the linear and nonlinear wave model are indicated with L and NL and the subscripts $_{ref}$ and $_{spec}$ refer to the reference case of the weighted T_p and the load cases using a specific T_p, respectively.

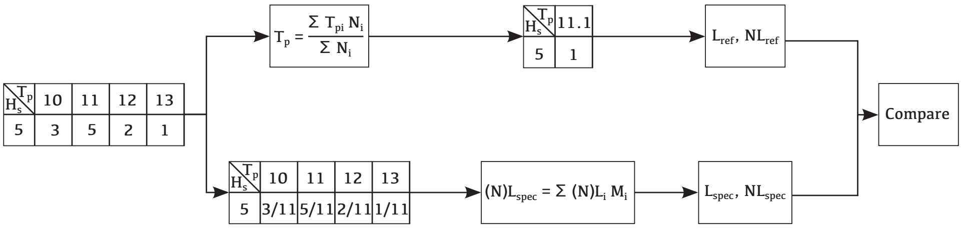

Figure D.1: Numerical example of the weighted T_p (top) vs. the specific T_p (bottom).

When taking a weighted T_p the shorter, steeper waves that contributed most to the nonlinear effects are not specifically considered. At the same time, the longer, flatter waves that typically have a low amount of nonlinearity, are not specifically taken into account either. In order to check the influence of this simplification, two H_s bins are selected and the wave loads are calculated for each specific $H_s - T_p$ combination. Consequently, the stresses in all members are calculated and weighted based on their number of occurrence. This total stress per member can then be compared to the stress obtained from the single load case that is calculated using the weighted T_p. The simplification is expected to mainly influence the comparison between the linear and nonlinear wave model and not the performance of the reduced models. Therefore, the results are measured in terms of the ratio of the stresses induced by the nonlinear wave model over those from the linear model.

	H_s = 1.5 m	H_s = 7.5 m
$\frac{L_{ref}}{L_{spec}}$	96%	5.5%
$\frac{NL_{ref}}{NL_{spec}}$	98%	7.6%
$\frac{NL_{ref}}{L_{ref}}$	0.7%	22%
$\frac{NL_{spec}}{L_{spec}}$	0.5%	19%

Table D.1: Total stress increase (0.38 Hz).

	H_s = 1.5 m	H_s = 7.5 m
$\frac{L_{ref}}{L_{spec}}$	143%	16%
$\frac{NL_{ref}}{NL_{spec}}$	135%	15%
$\frac{NL_{ref}}{L_{ref}}$	1.4%	13%
$\frac{NL_{spec}}{L_{spec}}$	2.6%	15%

Table D.2: Total stress increase (0.28 Hz).

For this sensitivity study the dominant wave direction (330°) is selected in order to investigate the load cases with the highest impact on the structure's total loading. Within this direction the most dominant significant wave height bin is taken, which gives an average H_s of 1.5 m (figure 4.4). In order to also incorporate the influence of the wave height on this sensitivity study, the same comparison is carried out for a high H_s bin, i.e. 7.5 m. To be able to capture the comparison in a single value, the average of the total stress in all members is compared. On the one hand it is investigated how well the *reference* load case of the weighted T_p is able to represent the total stress, compared to a weighted average of all the load cases with a *specific* T_p. On the other hand, it is of great interest what the influence of a weighted T_p has on the ratio between the stresses induced by the linear and nonlinear wave model. In tables D.1 and D.2 the results are presented where the values represent the ratios of the mean of the total stress in all members. Table D.1 contains the values for the original structural model as described in section 4.3. In table D.2 the results are presented for a more flexible structural model check the sensitivity of the values in table D.1.

First of all, when considering the top two rows of table D.1, several observations can be made. It can be noticed that the reference case produces a higher total stress than the weighted specific cases for both H_s bins. The fact that this is significantly higher for the low H_s bin derives from the large spreading in T_p values (figure 4.4). In the case of $H_s = 1.5$ m the T_p values range from 3.5 s to 22.5 s, whereas for the case where $H_s = 7.5$ the peak period values only range from 11.5 s to 15.5 s. It is therefore likely that a weighted T_p in the latter case will produce a result that is more coherent with the results from the specific cases. Secondly, when observing the results from the bottom two rows, some more interesting conclusions can be drawn. As expected, the cases with the high significant wave height yield a much higher second-order contribution than the low H_s cases. The most important finding is that the ratio of the reference case and that of the specific cases show only a small discrepancy. In the top two rows the reference case has shown to overestimate the total stress compared to the weighted specific cases. When looking at the nonlinear contribution, the reference case and the specific case show very similar results. This last finding seems to indicate that despite the fact that the reference case overestimates the total stress in absolute sense (top two rows), the relative importance of the second-order contribution is still captured quite accurately (bottom two rows). Table D.2 shows similar trends and the ratios of the nonlinear stress over the linear stress are fairly close together.

It is noted that all results in tables D.1 and D.2 strongly depend on the actual realization of the random signal. As for each of the specific load cases a different input spectrum is used, also the seed is different for all load cases. This requires the averaging of the total stresses of the specific load cases since no direct time series comparison can be made with the reference signal. The extent to which the single realization of the reference load case is able to capture the results from the specific load cases is dependent on that realization. Overall it can be concluded that the simplification of the load case table through the weighted average T_p has a significant impact on the calculated stresses in the jacket members. This is especially true when considering the stress in an absolute sense, where the error is largest when the reference case is supposed to represent a wide range of T_p values. The ratio between the stresses caused by the first- and second-order wave model seems to be captured well by the reference case. However, to increase statistical stability a larger number of seeds should be used. Finally, the results presented above provide enough confidence to use the reduced load case table for this comparative study but also indicate that a full load case table should be used when performing an actual fatigue load analysis.

E

Proper Orthogonal Decomposition

The Proper Orthogonal Decomposition (POD) method, also know as Principal Component Analysis (PCA), is a mathematical data analysis method to efficiently extract the principal components from large, complex data sets. The POD method describes an orthogonal linear transformation, which transforms data dependent on n possibly correlated variables to a reduced or equal set of uncorrelated variables, referred to as principal components. For the mathematical description of the POD method the reader is referred to [21]. Here only the practical implementation for this thesis is discussed.

Starting with some time-varying signal, a number of snapshots m can be obtained. Each of these snapshots represents a vector $\boldsymbol{z_i}$ which contains the values of n output variables. The $\boldsymbol{z}$ vectors are collected in the matrix $\boldsymbol{Z}$:

$$\boldsymbol{Z} = \begin{bmatrix} \boldsymbol{z_1} & \dots & \boldsymbol{z_m} \end{bmatrix} = \begin{bmatrix} z_{11} & \dots & z_{1m} \\ \vdots & \ddots & \vdots \\ z_{n1} & \dots & z_{nm} \end{bmatrix} \tag{E.1}$$

In this thesis the $\boldsymbol{Z}$ matrix is filled with a wave load time series, typically consisting of 6000 vectors (each time step of a 10 minute simulation) each with approximately 1000 entries (representing the unreduced DoF of the jacket). Based on the $\boldsymbol{Z}$ matrix the so-called sample covariance matrix can be constructed:

$$\boldsymbol{C} = \sum_{i=1}^{m} \mathrm{E}\left[(\boldsymbol{z_i} - \boldsymbol{\mu})(\boldsymbol{z_i} - \boldsymbol{\mu})^T\right] \tag{E.2}$$

Where $\boldsymbol{\mu}$ is the average of the snapshots. The snapshots can be chosen such that they have a zero mean:

$$\boldsymbol{x_i} = \boldsymbol{z_i} - \boldsymbol{\mu} \tag{E.3}$$

Now the covariance matrix can expressed accordingly:

$$\boldsymbol{C} = \frac{1}{m}\sum_{i=1}^{m} \boldsymbol{x_i}\boldsymbol{x_i}^T = \frac{1}{m}\boldsymbol{X}\boldsymbol{X}^T \tag{E.4}$$

The eigensolutions to the $(n \times n)$ covariance matrix $\boldsymbol{C}$ characterize the POD and are given by:

$$\boldsymbol{C}\phi_j = \lambda_j \phi_j \tag{E.5}$$

The eigenvectors ϕ_j represent the proper orthogonal modes (POMs). The eigenvalues λ_i represent the proper orthogonal vectors (POVs) which are an indication for the energy captured by the corresponding in POM.

Another way to obtain the POMs and the POVs is to apply the Singular Value Decomposition (SVD) method to $\boldsymbol{X}$. The SVD of the real-valued $\boldsymbol{X}$ matrix can be written as:

$$\boldsymbol{X} = \boldsymbol{U}\boldsymbol{\Sigma}\boldsymbol{V}^T \tag{E.6}$$

Where $\boldsymbol{U}$ is the $(n \times n)$ matrix containing left singular vectors, $\boldsymbol{\Sigma}$ is the $(n \times m)$ matrix containing the singualr values and $\boldsymbol{V}$ is the $(m \times m)$ matrix of right singular vectors. Since $\boldsymbol{U}$ and $\boldsymbol{V}$ are unity matrices, the following holds:

$$\boldsymbol{X}\boldsymbol{X}^T = \boldsymbol{U}\boldsymbol{\Sigma}\boldsymbol{V}^T\boldsymbol{V}\boldsymbol{\Sigma}^T\boldsymbol{U}^T = \boldsymbol{U}\left(\boldsymbol{\Sigma}\boldsymbol{\Sigma}^T\right)\boldsymbol{U}^T \tag{E.7}$$

$$\boldsymbol{X}^T\boldsymbol{X} = \boldsymbol{V}\boldsymbol{\Sigma}^T\boldsymbol{U}^T\boldsymbol{U}\boldsymbol{\Sigma}\boldsymbol{V}^T = \boldsymbol{V}\left(\boldsymbol{\Sigma}\boldsymbol{\Sigma}^T\right)\boldsymbol{V}^T \tag{E.8}$$

The right hand side of equations E.7 and E.8 describes the eigenvalue decomposition of $\boldsymbol{X}\boldsymbol{X}^T$ and $\boldsymbol{X}^T\boldsymbol{X}$, respectively. By taking the square root of the eigenvalues of $\boldsymbol{X}\boldsymbol{X}^T$ the singular values of $\boldsymbol{X}$ are obtained. These values correspond to the POVs multiplied with the number of samples m. In turn, the left singular vectors $\boldsymbol{U}$ of $\boldsymbol{X}$ correspond to the eigenvectors of $\boldsymbol{X}\boldsymbol{X}^T$ and thus to the POMs. The SVD method has two advantages over the POD method. Firstly, extra information is extracted in the form of matrix $\boldsymbol{V}$, which contains the time modulation of the corresponding POM, normalized by the singular value. Secondly, as it avoids the calculation of the covariance matrix, it is more computationally efficient to apply the SVD method to the snapshot matrix than the POD to the covariance matrix [20].

F

Newmark time integration method

The Newmark time integration method was developed in 1959 and is nowadays still widely used. The method is an efficient single-step integration procedure. The basic idea of the method is that the displacements and velocities at time $t_{n+1} = t_n + h$ can be found based on values at time t_n. This is done by means of a Taylor series expansion of the state vector. The velocities and displacements at time t_{n+1} can be calculated according to equation (F.1) and (F.2), respectively:

$$\dot{\boldsymbol{q}}_{n+1} = \dot{\boldsymbol{q}}_n + \int_{t_n}^{t_{n+1}} \ddot{\boldsymbol{q}}(\tau) d\tau \tag{F.1}$$

$$\boldsymbol{q}_{n+1} = \boldsymbol{q}_n + h\dot{\boldsymbol{q}}_n + \int_{t_n}^{t_{n+1}} (t_{n+1} - \tau)\ddot{\boldsymbol{q}}(\tau) d\tau \tag{F.2}$$

Subsequently, the integral of the acceleration terms is approximated using a numerical quadrature. To this end $\ddot{\boldsymbol{q}}(\tau)$ is defined in the time interval $[t_n, t_{n+1}]$ as a function of $\ddot{\boldsymbol{q}}_n$ and $\ddot{\boldsymbol{q}}_{n+1}$ at the interval limits:

$$\int_{t_n}^{t_{n+1}} \ddot{\boldsymbol{q}}(\tau) d\tau = (1-\gamma)h\ddot{\boldsymbol{q}}_n + \gamma h \ddot{\boldsymbol{q}}_{n+1} + \boldsymbol{r}_n \tag{F.3}$$

$$\int_{t_n}^{t_{n+1}} (t_{n+1} - \tau)\ddot{\boldsymbol{q}}(\tau) d\tau = \left(\tfrac{1}{2} - \beta\right) h^2 \ddot{\boldsymbol{q}}_n + \beta h^2 \ddot{\boldsymbol{q}}_{n+1} + \boldsymbol{r}'_n \tag{F.4}$$

Where $\boldsymbol{r}_n$ and $\boldsymbol{r}'_n$ are the corresponding error measure. The constants γ and β are the parameters of the quadrature scheme. They can be chosen freely, leading to different levels of accuracy and stability of the method. By substituting equation (F.3) and (F.4) into equation (F.1) and (F.2) respectively, the following approximation equations for the Newmark method are obtained:

$$\dot{\boldsymbol{q}}_{n+1} = \dot{\boldsymbol{q}}_n + (1-\gamma)\, h\ddot{\boldsymbol{q}}_n + \gamma h \ddot{\boldsymbol{q}}_{n+1} \tag{F.5}$$

$$\boldsymbol{q}_{n+1} = \boldsymbol{q}_n + h\dot{\boldsymbol{q}}_n + \left(\tfrac{1}{2} - \beta\right) h^2 \ddot{\boldsymbol{q}}_n + \beta h^2 \ddot{\boldsymbol{q}}_{n+1} \tag{F.6}$$

Here the assumption is made that the equations of motion are linear, i.e. the matrices $\boldsymbol{M}$, $\boldsymbol{C}$ and $\boldsymbol{K}$ are independent of $\boldsymbol{q}$. Finally, the acceleration $\ddot{\boldsymbol{q}}_{n+1}$ can be computed as follows:

$$\begin{aligned}\left(\boldsymbol{M} + \gamma h \boldsymbol{C} + \beta h^2 \boldsymbol{K}\right) \ddot{\boldsymbol{q}}_{n+1} = \boldsymbol{f}_{n+1} &- \boldsymbol{C}\, \left(\dot{\boldsymbol{q}}_n + (1-\gamma)\, h\ddot{\boldsymbol{q}}_n\right) \\ &- \boldsymbol{K}\left(\boldsymbol{q}_n + h\dot{\boldsymbol{q}}_n + \left(\tfrac{1}{2} - \beta\right) h^2 \ddot{\boldsymbol{q}}_n\right)\end{aligned} \tag{F.7}$$

Solving this equation implies inverting a linear system of equations associated with the time stepping matrix $\boldsymbol{S}$:

$$\boldsymbol{S} = \boldsymbol{M} + \gamma h \boldsymbol{C} + \beta h^2 \boldsymbol{K} \tag{F.8}$$

For a constant time step the $\boldsymbol{S}$ matrix only needs to be evaluated once. When the acceleration terms are calculated, the velocities and displacements follow from equation (F.5) and (F.6), respectively.

F.1 Implicit Newmark scheme

For the implicit Newmark scheme the state vector at time t_{n+1} is a function of its own time derivative, meaning that $\beta \neq 0$. A linear set of equations has to be solved to find $\ddot{\boldsymbol{q}}_{n+1}$, before $\dot{\boldsymbol{q}}_{n+1}$ and $\ddot{\boldsymbol{q}}_{n+1}$ can be computed. To ensure the system's stability, the following should hold: $\gamma \geqslant \frac{1}{2}$ and $\beta \geqslant \frac{1}{4}(\gamma + \frac{1}{2})^2$.

F.2 Explicit Newmark scheme

For the explicit Newmark scheme the state vector at time t_{n+1} can be calculated directly from the results at the previous time step, hence $\beta = 0$. No system of equations has to be solved now. Stability of the system is secured when $\gamma \geqslant \frac{1}{2}$ and $h < \frac{2}{\omega}$, where h is the time step and ω is the highest possible eigenfrequency in the system.

Bibliography

[1] P. Agarwal. *Structural Reliability of Offshore Wind Turbines*. PhD thesis, University of Texas AT Austin, 2008.

[2] G.B. Airy. Tides and waves. *Encyclopaedia Metropolitana*, 1845.

[3] A.A. Mohamad Ali, A. Al-Kadhimi, and M. Shaker. Dynamic behavior of jacket type offshore structure. *Jordan Journal of Civil Engineering*, volume 6, no. 4, 2012.

[4] J.W. Cooley and J.W. Tukey. An algorithm for the machine calculation of complex fourier series. *Mathematics of Computation*, volume 19: p. 297–301, 1965.

[5] R. Craig and M. Bampton. Coupling of substructures for dynamic analysis. *AIAA Journal*, volume 6: p. 1313–1319, 1968.

[6] D. de Klerk, D.J. Rixen, and S.N. Voormeeren. General framework for dynamic substructuring: History, review, and classification of techniques. *AIAA Journal*, volume 46: p. 1169–1181, May 2008.

[7] R.G. Dean and R.A. Dalrymple. *Water wave mechanics for engineers and scientists*. World Scientific, 1991.

[8] Det Norkse Veritas. Recommended practice DNV-RP-C205: Environmental conditions and environmental loads, October 2010.

[9] J. Dickens. A critique of mode acceleration and modal truncation augmentation methods for modal response analysis. *Computers & Structures*, volume 62: p. 985 – 998, 1997.

[10] EWEA. The european offshore wind industry - key trends and statistics 1st half 2013, June 2013.

[11] EWEA. Wind energy statisticis and targets. Factsheet, 2013.

[12] O.M. Faltinsen. *Sea loads on ships and offshore structures*. Cambridge University Press, 1990.

[13] J.D. Fenton. Nonlinear wave theories. *Ocean Engineering Science*, Volume 9: p. 3–25, 1990.

[14] G. Gladwell. Branch mode analysis of vibrating systems. *Journal of Sound and Vibration*, volume 1: p. 41–59, 1964.

[15] J. Grue, D. Clamond, M. Huseby, and A. Jensen. Kinematics of extreme waves in deep water. *Applied Ocean Research*, Volume 25: p. 355–366, 2003.

[16] R.J. Guyan. Reduction of stiffness and mass matrices. *AIAA Journal*, volume 3: p. 380, 1965.

[17] K. Hasselmann, T.P. Barnett, E. Bouws, H. Carlson, D.E. Cartwright, K. Enke, J.A. Ewing, H. Gienapp, D.E. Hasselmann, P. Kruseman, A. Meerburg, P. Muller, D.J. Olbers, K. Richter, W. Sell, and H. Walden. *Measurements of Wind-Wave Growth and Swell Decay during the Joint North Sea Wave Project (JONSWAP)*. Deutsches Hydrographischer Institut, 1973.

[18] L.H. Holthuijsen. *Waves in Oceanic and Coastal Waters*. Cambridge University Press, 2007.

[19] W.C. Hurty. Vibrations of structural systems by component mode synthesis. *Journal of Engineering Mechanics/American Society of Civil Engineers*, volume 86: p. 51–69, 1960.

[20] G. Kerschen, J.C. Golinval, A. Vakakis, and L. Bergman. The method of proper orthogonal decomposition for dynamical characterization and order reduction of mechanical systems: An overview. *Nonlinear Dynamics*, volume 41: p. 147–169, 2005.

[21] Y. Liang, H. Lee, S. Lim, W. Lin, K. Lee, and C. Wu. Proper orthogonal decomposition and its applications - part 1. *Journal of Sound and Vibration*, volume 252: p. 527–544, 2002.

[22] M.S. Longuet-Higgins. The effect of non-linearities on statistical distributions in the theory of sea waves. *Journal of Fluid Mechanics*, volume 13: p. 459–480, 1963.

[23] R. MacNeal. Hybrid method of component mode synthesis. *Computers and Structures*, volume 1: p. 581–601, 1971.

[24] P.A. Madsen. An introduction to boussinesq formulations, January 2008. Department of Mechanical Engineering, Technical University of Denmark.

[25] SINTEF Marintek. USFOS. Computer software, 2014.

[26] T. Marthinsen and S.R. Winterstein. On the skewness of random surface waves. *Proceedings of the Second International Offshore and Polar Engineering Conference*, volume 3: p. 472 – 478, 1992.

[27] J.R. Morison, M.P. O'Brian, J.W. Johnson, and S.A. Schaaf. The force exerted by surface waves on piles. *Petroleum Transactions*, volume 189: p. 149–154, 1950.

[28] M.K. Ochi and E.N. Hubble. Six-parameter wave spectra. *Coastal Engineering*, volume 15: p. 301–328, 1976.

[29] REN21. Renewables 2014 global status report, 2014.

[30] renewableUK. Offshore wind: Forecasts of future costs and benefits, June 2011.

[31] D. Rixen. Generalized mode acceleration methods and modal truncation augmentation. In *Structures, Structural Dynamics and Material Conference and Exhibit*. 42st AIAA/ASME/ASCE/AHS/ASC, Seattle, WA, USA, April 2001.

[32] S. Rubin. Improved component-mode representation for structural dynamic analysis. *AIAA Journal*, volume 13: p. 995–1006, 1975.

[33] T. Sarpkaya and M. Isaacson. Mechanics of wave forces on offshore structures. *Van Nostrand Reinhold Company*, 1981.

[34] H.A. Schwarz. *Gesammelte Mathematische Abhandlungen*, volume 2: p. 133–143, 1890. First published in Vierteljahrsschrift der Naturforschenden Gesellschaft in Zurich, volume 15, p. 272-286, 1870.

[35] SER. Energieakkoord voor duurzame groei, September 2013.

[36] J.N. Sharma and R.G. Dean. Second-order directional seas and associated wave forces. *Old SPE journal*, volume 21, no. 1: p. 129–140, 1981.

[37] C.T. Stansberg. Kinematics under extreme waves. *Journal of Offshore Mechanics and Artic Engineering*, volume 130, no. 2, 2008.

[38] C.T. Stansberg. Second-order effects in random wave modelling. In *International symposium: waves - physical and numerical modelling*, p. 793-802, 1994.

[39] I.A. Svendsen and I.G. Jonsson. *Hydrodynamics of coastal regions*. Den private ingeniørfond, Technical University Denmark, 1982.

[40] K. Torsethaugen. Model for a doubly peaked spectrum, report no. STF22 A96204. Technical report, SINTEF Civil and Environmental Engineering, Trondheim, Norway, 1996.

[41] M.B. van der Meulen. Influence of nonlinear irregular wave modeling on the dynamic response of an offshore wind turbine. Master's thesis, Delft University of Technology, 2012.

[42] P.L.C. van der Valk. *Coupled Simulations of Wind Turbines and Offshore Support Structures*. PhD thesis, TU Delft, 2014.

[43] S.N. Voormeeren. *Dynamic Substructuring Methodologies for Integrated Dynamic Analysis of Wind Turbines*. PhD thesis, TU Delft, 2012.

[44] S.N. Voormeeren, P.L.C. van der Valk, B.P. Nortier, D-P. Molenaar, and D. J. Rixen. Accurate and efficient modeling of complex offshore wind turbine support structures using augmented superelements. *Wind Energy*, volume 17: p. 1035–1054, 2013.

[45] F. Vorpahl, W. Popko, and D. Kaufer. Description of a basic model of the "UpWind reference jacket" for code comparison in the OC4 project under IEA Wind Annex XXX. Technical report, Fraunhofer Institute for Wind Energy and Energy System Technology, 2011.

[46] J.D.E. Wheeler. Method for calculating forces produced by irregular waves. *Journal of Petroleum Technology*, volume 249: p. 359–367, 1969.

[47] R.L. Wiegel. A presentation of cnoidal wave theory for practical application. *Journal of Fluid Mechanics*, volume 7, no. 18, 1960.